Alma Mater Studiorum – Università di Bologna

DOTTORATO DI RICERCA IN

FISICA

Ciclo XXIX

Settore Concorsuale di afferenza: **02/B1**

Settore Scientifico disciplinare: **FIS/03**

Experimental study on mechanical and electromagnetic properties of novel silicon photonic devices

Presentata da: **Diego Marini**

Coordinatore Dottorato

Prof. Gastone Castellani

Relatore

Prof. Beatrice Fraboni

Correlatore

Dott. Gabriele Bolognini

Esame finale anno 2017

Contents

Introduction

The data volume from fixed and mobile Internet usage has grown enormously during the last years and has brought to new model of operating the Internet based on Information technology (IT) infra-structures, as data centers and supercomputers, where the data are stored and processed and provisioning takes place. The demand to exchange this amount of data via interconnects represents an extremely challenging technological issue that lately has led to a redesign of the communication platform actually based on electrical transmission lines. As a matter of fact, the growth rate of the electrical communication links was not able to match that of data volume: this is ultimately due to physical limits, mainly imposed by the ohmic resistance and capacitance of the conductors tracks the line is based on, that impair data exchange at communication bit rate greater than some GHz. The introduction of optics in interconnects and switching fabrics has proved the potential to scale to higher capacities, reduce the power consumption and heat generation. In this context, a new research area, named silicon photonics (SiPh), has raised growing interest, combining outcomes from material and semiconductor sciences with photonics and micro-fabrication technologies. SiPh proved to effectively leverage the mature complementary metal-oxide semiconductor (CMOS) nanofabrication technique to develop photonic and electronic integration on silicon chips. SiPh is therefore expected to provide reliable and low-cost solutions to this so-called "bandwidth wall": this is the reason why data center equipment manufacturers and semiconductors chip makers massively invest on SiPh research.

Important functionalities for interconnect solutions, such as signal modulation and frequency conversion, require the presence of second order nonlinear effects in the employed materials. Unfortunately, these effects are too weak in pure silicon and cannot be exploited. This characteristic limited the employment of this material to passive optical devices and brought to development of hybrid solutions to accomplish more complex tasks that strongly complicates the manufacturing process and rises the cost of the fabrication. The recent discovery of nonlinear effects, such as Pockels effect and second-harmonic generation (SHG), in silicon structures that are strained by the deposition of high intrinsic stress film, paved the way for the realization of SiPh nonlinear and active devices. Since that discovery, several interferometric strained silicon devices achieving modulation functionalities have been reported and frequency conversion has been demonstrated in strained silicon structures.

In this Thesis dissertation I have described the outcomes of an extensive set of simulative and experimental analyses carried out on strained-silicon micrometric and nanomentric structures and devices for photonic applications. The scope of this study was to perform a thorough analysis on the novel material properties, as well as to develop accurate and reliable simulative models for the design of photonic devices based on strained silicon technology, and assess the possible use of innovative experimental techniques for the strain measurement in photonic structures. In addition, this analysis allowed us to estimate the quality of the nanofabrication processes and techniques employed for the manufacturing of the devices.

Firstly a simulative model, based on the finite element method (FEM), has been developed to estimate the strain and stress distribution across the silicon structures and devices deformed by a high intrinsic stress silicon nitride film. The accuracy and the reliability of the model have been assessed through a comparative analysis between the simulative estimations and the experimental strain measurements carried out with the Convergent Beam Electron Diffraction (CBED) technique. Since CBED technique had never been employed for strain measurements of this type of structures, this analysis allowed to assess the possibility to extend the field of application of this technique to photonic devices. Subsequently, the model has been integrated in a multiphysical simulative model capable of estimating the electromagnetic properties of strained silion-on-insulator (SOI) single mode waveguide. The multiphysical model takes into account the effects induced by the lattice deformation on the optical properties of silicon through the photoelastic effect. Finally, the optical properties of the manufactured strained SOI waveguide have been analyzed through measurements of guiding properties and optical losses employing the Fabry-Perot resonances technique. All the experimental analysis allowed to evaluate the quality of the manufacturing processes, and in particular the adequacy of the Spacer Pattering Method (SPM) technique that had never been employed for the realization of photonic devices.

In Chapter 1 overview the potential and the advantages of introducing optics, and in particular the silicon photonics technology, in the interconnects of IT infrastructures are discussed. Then, the commonly exploited effects for accomplishing modulation functionalities on silicon-based devices are described. Subsequently a brief review of the state-of-the-art of the strained silicon technology is given, focusing on novel optical devices employing strained silicon as electro-optic material.

In Chapter 2 the mechanical properties of silicon crystal are described and the lattice deformation induced by the deposition of a silicon nitride high-intrinsic stress layer on SiPh structures is discussed. Then, the optical properties of silicon are described with a focus on the electro-optic and photoelastic effect. Subsequently, the working principles underlying the guiding mechanism of optical waveguides are analyzed together with the sources of propagation and bending loss suffered by the radiation traveling in SOI waveguides. Following, the mathematical formulation of the FEM is introduced and its application to structural and electromagnetic problems are analyzed. Finally, I outlined the

basic working principles of silicon microring resonators and of radiation scattering by diffraction gratings.

In Chapter 3 the technological processes employed for the manufacturing of the strained silicon devices are described. The process flow, for the microfabrication of the micrometric strained silicon structures, is detailed and the operating principles of the main employed fabrication steps, such as the photolithography and dry etching, are analyzed. Then the fabrication processes employed for the realization of the nanometric structures on silicon substrate and SOI waveguide-based devices are described; the spacer technique, utilized for the manufacturing of the submicrometric feature and gaps, is detailed. The description of the manufacturing processes is supported by optical microscopy, Scanning Electron Microscopy (SEM) and Transmission Electron Microscopy (TEM) analysis that provided images in correspondence of intermediate fabrication steps for novel manufacturing process assessment and validation.

In Chapter 4 the Convergent Beam Electron Diffraction (CBED) technique used for the strain measurements of the manufactured structures is described. The physical principles underlying the electron diffraction microscopy are introduced and the operating principles of the TEM at the basis of the CBED technique are described. Subsequently, the procedure for estimating the components of the strain tensor through the analysis of the diffraction patterns is described. Finally, some results of the STEM analysis and SEM analysis of the manufactured micrometric and nanometric strained silicon structures are reported through which the quality of the manufacturing processes has been assessed.

In Chapter 5 the results of simulative analysis of stress and strain tensors components are reported for the geometries observed in the micrometric and nanometric manufactured silicon ridges. The results of the comparative analysis between the estimated lattice deformation and strain measurement through the CBED technique are reported. Then the results of the simulative analysis on the optical properties of the strained SOI waveguides, obtained through the employment of the multyphisical simulative model, are discussed: in particular the estimation of modal intensity distribution, effective refractive index, effective group index and birefringence have been evaluated. Finally the results of the propagation loss measurements on the manufactured SOI devices are discussed.

SiPh technology also provides solutions in fields where the deployment of bulk optical components, due to their large size and the slow switching speed, proved to be unsuitable, as the case of Orbital Angular Momentum (OAM)-based optical communications. The optical orbital angular momentum is a degree of freedom of the photon in addition to the polarization/spin. After the demonstration that physically realizable beams with intensity distributions $u(r, \phi, z) = u_o(r, z)exp(i\phi l)$ carry a well defined OAM about the axis, OAM beams have been employed in different fields for various applications. In particular, light-carrying orbital angular momentum (OAM) has proved to have great potential in enhancing the information channel capacity in both classical and quantum optical communications. Initially, the OAM order was exploited as a new degree of freedom for modulation schemes of the signal beside the

traditional solutions relying on modulation of intensity, frequency, or polarisation of the radiation. Lately, mutliplexing schemes based on different OAM orders have been studied in which the capacity of the links is significantly enhanced through the inclusion of the OAM degree of freedom on the traditional envisioned switching domains (space, wavelength, and time).

In Chapter 6 I reported the results of an experimental study carried out on SiPh integrated emitters of beams carrying a well-defined OAM order. The OAM emitters are basically ring-shaped resonator photonic structures embedding second order angular grating capable of extracting circulating light and imposing a particular phase distribution, together with a well defined OAM order, to the radiation. Two types of integrated OAM beam emitters have been studied: the first type are micrometer-sized SOI ring resonators while the second are quasi circular waveguide with a small opening angle in the resonant structures. The second type of OAM devices are said Omega-emitters due to the similarity of the layout with the last latter of the Greek alphabet. This geometry allows to pack, in one planar substrate, several emitters with the same optical axis allowing the multiplexing of beams with different OAM orders. The radiation efficiency analysis of the ring emitter provided information on the combined effects of the geometrical parameters of ring layout and the grating geometry on the performance of the devices and produced a guideline for the design optimization of the device. The characterization of the OAM beams emitted by the Omega multiplexers, in terms of purity of the radiated modes, is aimed at providing a proof of concept of the working principle of this innovative devices and supply information on the possible use of these geometry in efficient multiplexing schemes.

Chapter 1

Overview: strained silicon and optical interconnects

1.1 Optical interconnects in datacom applications

Due to the even-growing data volume exchanged in fixed and mobile internet usage traffic, new models of operating the Internet, such as the 'Cloud', have been introduced: they are based on large information technology (IT) infra-structures as data centers and supercomputers, where the data are stored, processed and provisioning takes place[1]. The constant improvement in the computational performance of these IT infrastructures is jeopardized by the interconnection networks based on the electronics, that cannot efficiently accomplish the transfer of data at frequencies greater than Gb/s[2]. In particular bandwidth, wiring density, and power consumption of the metal wires are proving to be bottlenecks to the further scaling of speed and capacity of the high performance computing platforms as interconnect density rises[3]. Recently, active optical cable technology has been adopted for the transfer of data between the servers (inter-rack level) and copper-based Ethernet runs have been replaced by fiber optics links[4, 5]. At the same time intra-chip, inter-chip, and inter-board communications are still based on copper networks and data switching and routing functionalities are still implemented at electronic level.

The introduction of optics in interconnects and switching fabrics has the potential to scale to higher capacities, reduce the power consumption and heat generation and increase the reliability in a cost-effective manner[6]. Silicon photonics (SiPh) aims at leveraging the mature complementary metal-oxide semiconductor (CMOS) nanofabrication technique to develop photonic and electronic integration on silicon chips[7]. Furthermore SiPh enables much greater I/O bandwidth into and out of the chip overcoming the physical limitation faced by the metal wires[8]. Much effort has been devoted by semiconductor manufacturers to the development of SiPh optical functionalities and lately important goals have been scored: in 2013 a Cisco-funded start-up, Compass EOS,

unveiled a modular router with silicon photonic chips [9]and Intel in 2016 announced an inter-rack optical transceiver employing Indium Phosphide laser on silicon chips aligned to optical fiber capable of 100 Gb/s communications over several kilometers[10].

Microring resonators (MRR) and Mach-Zhender interferometers (MZI), due to their unique properties in terms of wavelength selectivity and filtering properties [11, 12], have been extensively studied as the basic building block for silicon photonic chip implementing optical routing and switching functionalities[13, 14, 15]. These devices are usually studied and manufactured employing silicon-on-insulator (SOI) platform that uses a layered silicon-silicon dioxide-silicon substrate as starting wafers. The SOI platform is fully CMOS compatible and a complete integration of the optical devices with the electronics boards is possible with a consequent reduction of the possible failures that could arise from bonding or metal connections present in hybrid integration solution[16]. The wavelength response of the MRR and MZI can be controlled, in dynamical scheme, modifying the refractive index of the silicon wire patterned in the silicon layer that confines the radiation[17][18]. The change of the refractive index can be accomplished through the exploitation of various physical effects present in silicon: in the next section some of the physical effect commonly employed in modulation scheme in semiconductor and in silicon are described.

1.2 Optical modulation in silicon

Optical modulation consists of the variation of the amplitude, phase or polarization of a light beam and is one of the main required functionalities for any optical interconnect solution[19]. Various effects are exploited to modulate a radiation: in electro-refractive modulators the application of an electric field induces a change in the real part of the refractive index causing a variation in the phase velocity of the radiation. In electro-absorption modulators the presence of an electric field changes the imaginary part of the refractive index reducing or enhancing the loss of the medium. The commonly exploited electric field effects for semiconductor materials are the linear electro-optic effect (also said Pockels effect) and Kerr effect for (electro-refraction) and Franz-Heldysh effect (electro-absorbtion)[20][21]. These effects are absent or weak in pure silicon at the telecommunication wavelength of 1.3 um and 1.55 um and cannot be employed in efficient modulation schemes.

The silicon modulator can be implemented using thermo-optic effect, that is the variation of the refractive index in response to a temperature variation[22]. Owing to the large thermo-optic coefficient of silicon, $\triangle n = 1.86 \cdot 10^{-4} K^{-1}$ and $\triangle \alpha = 10^{-4} cm^{-1}$at $\lambda = 1550\, nm$, [23]TO modulation has a key merit of wide wavelength tuning range if utilized in resonator or interferometric devices. For example, a temperature rise of $100\, K$ results in a variation of the refractive index of about $2 \cdot 10^{-2}$ that determines a resonance wavelength shift of several nanometers in SOI microring resonator inducing at the same time negligible loss ($0.04 bB/cm$), as demonstrated in[24].

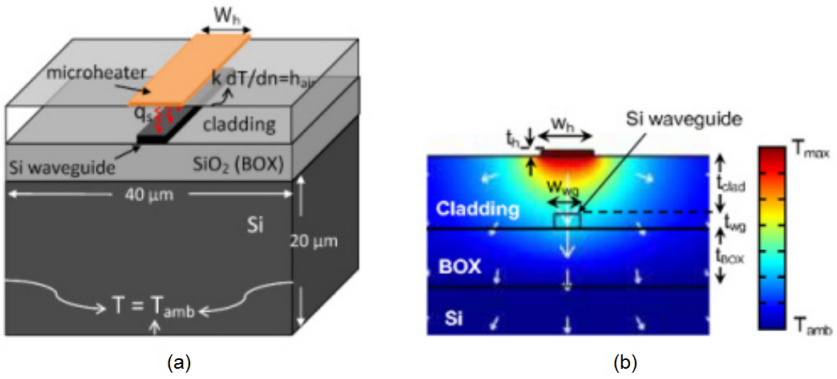

Figure 1.1: (a) Schematic of a typical metallic microheater fabricated over a Si waveguide on an SOI wafer. (b) Simulative estimation of temperature distribution at the cross-section of an SOI waveguide when current flows in the metallic microheater and heat is generated, from [25].

The common approach to control the silicon waveguide temperature is to integrate a microheater on the top of the device, (see Fig. 1.1)[25]:

the microheater is basically of a high-resistive metallic layer that dissipates, due to Joule effect, some power of the current passing through it in correspondence of the waveguide and acting as a heat source. Despite the high resonance wavelength tunability of TO modulators and the negligible loss induced, these modulation scheme are not suitable for modern telecomunication applications due to the low tuning speed (of the order of um) imposed by the slow thermal diffusion processes.

The most common modulation mechanism employs the free-carrier dispersion effect in which the real and imaginary part of the refractive index is dependent on the concentration of the free carriers present in the material, i.e electrons and holes. The empirical equations for FCD-induced refractive index change $\triangle n$ and absorption coefficient change $\triangle \alpha$, at $\lambda = 1550\,nm$, are given as[26]:

$$\triangle n = -(8.8 \cdot 10^{-22} \triangle N_e + 8.5 \cdot 10^{-18} \triangle N_h^{0.8}) \tag{1.1}$$

$$\triangle \alpha = 8.5 \cdot 10^{-18} \triangle N_e + 6.0 \cdot 10^{-18} \triangle N_h \tag{1.2}$$

where $\triangle N_e$ and $\triangle N_h$are the changes in electrons and holes concentrations. The electrical manipulation of the concentration of the free carriers interacting with the propagating light is implemented in p-i-n diode structures through different mechanisms: carrier injection, current depletion and carrier accumulation. Fig 1.2 illustrates a schematic of the structures employed for optical intensity modulation through carrier injection in a p-i-n diode embedded in a microresonator.

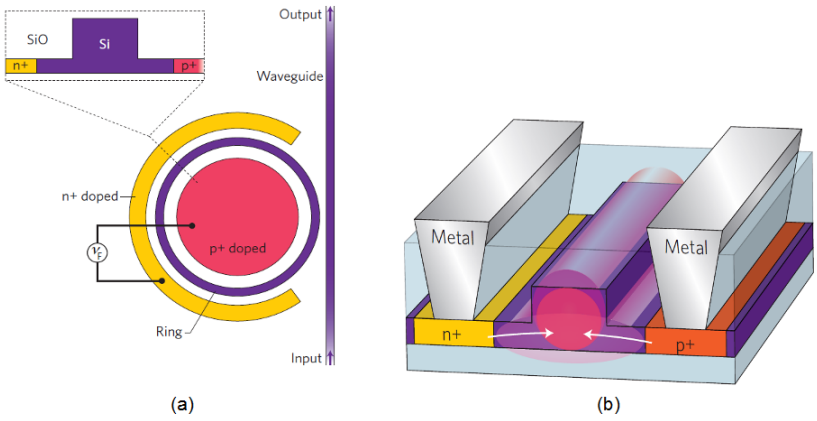

Figure 1.2: (a) Schematic of top-down and cross-sectional views of a FCD-based ring resonator structure. (b) Cross-section of a device structure implementing carrier depletion mechanism, from [19].

The plasma dispersion-based EO modulators have sub-ns to ns tuning speed and sub-mW power consumption, but the wavelength tuning range is limited by the induced FCA loss. For instance, a $2{\cdot}10^{19}\ cm^{-3}$ injected carrier concentration causing 2 nm spectral blueshift for the device represented in Fig. 1.2 induces a 100 dB/cm loss[7].

The slow response time of TO modulation and the high carrier-induced propagation loss represent major obstacle to the mass-usage of these mechanisms in modulation schemes. Furthermore, both effects exhibit non-negligible power consumption, due to resistive heating for thermo-optic effect or related to current propagation for carrier injection technique[27].

As summoned before, pure silicon doesn't show Pockels effect due to its centrosymmetric crystalline lattice arrangement. Nevertheless in 2006 it has been showed that is possible to enable the presence of this electro-optic effect depositing a high intrinsic stress film on the material. The Pockels effect presents potentially the advantages of both the described mechanisms of modulation: it allows switching speed performance as fast as FCD injection and wavelength tunability of the order to the ones obtained through TO effect. Furthermore it offers higher power efficiency since no current is required and the strained silicon technology requires much lower number of processing steps lowering the manufacturing production cost. In the next section a brief review on the history of strained silicon technology in silicon photonics is reported.

1.3 Strained silicon photonics

Lattice deformation in strained silicon photonic structures has been initially studied due to its effects on the waveguide optical anisotropy, i.e. birenfringence. In SOI waveguide, the mismatch in the thermal expansion coefficients between the silicon core and the silicon dioxide substrate and cladding layers produces stresses across the waveguide cross-section[28]. In particular, since silicon has larger thermal expansion coefficient than the oxide ($\alpha_{Si} = 3.6 \cdot 10^{-6} K^{-1}$ and $\alpha_{ox} = 5.4 \cdot 10^{-7} K^{-1}$) a significant compressive stress is generated at the Si/SiO_2 interface. The resulting deformation, through photelastic effect generates a certain amount of birefringence in the waveguide that adds to the geometrical contribution originating from the different boundary conditions for the perpendicular and transverse electric field components of the optical modes.

A large body of research has been devoted to the understanding and the control of the birefringence in SOI devices generated by the straining cladding layer. For example Xu et al[29], demonstrated that it is possible to modify or eliminate the birefringence for a wide range of waveguide cross-section shapes through the stress engineering of the SiO_2 cladding layer. In the experiment described, the silicon dioxide layer is deposited through Plasma Enhanced Chemical Vapour Deposition (PECVD). For thickness values about 1 μm the SiO_2 has a compressive stress of -320 MPa that compensates the original geometrical birerfringence reducing its value from $1.2 \cdot 10^{-3}$ down to $4.5 \cdot 10^{-5}$.

In 2006 the discovery of Jacobsen at al. promoted strained silicon as a key technology for the development of active silicon photonics[30]. Jacobsen et al. demonstrated that significant linear electro-optic effect and second-order nonlinearitites can be induced in silicon by breaking the symmetry of its crystal structure. As will be described in Chapter 2, the Pockels effect, i.e. linear electro-optic effects and second-order nonlinearities are prohibited by centrosymmetrical crystalline structure of silicon. The authors show that depositing a thick high intrinsic stress silicon nitride (Si_3N_4) layer on top of the silicon waveguide is possible to efficiently remove the silicon centrosymmetry and enable the presence of these effects. The silicon nitride film employed in the experiments, is deposited through PECVD technique on a 1.2 μm thick SiO_2 cladding layer. For thickness values of about 0.75 μm the intrinsic stress obtained is about 1 GPa. The authors demonstrated for the first time a Mach-Zender interferometer in silicon exploiting the induced Pockels effect and obtained nonlinear coefficient, $\chi(2) \approx 15\, pm\, V^{-1}$ employing slow light photonic crystal waveguide (PCW) to enhance the material nonlinearity, see Fig. 1.3.

Since the discover of Jacobsen, many works and studies on stress-induced electro-optic and nonlinear properties in silicon have been published. They aimed at the investigation of the potential of strained silicon to be a platform for a new class of integrated active optical devices. Cazzanelli at al [31]carried out second-harmonic-generation experiments and first-principle calculations on strained silicon photonic stuctures yielding second order nonlinear susceptibility up to 40 pm/V. In particular the analysis was carried out on strip SOI waveguide with micrometric dimensions stressed by silicon nitride cap layer with dif-

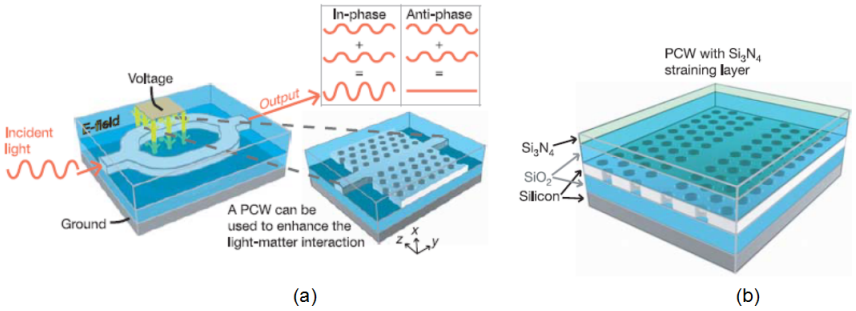

Figure 1.3: a) Schematic of a Mach–Zehnder modulator employing strain-induced Pockels effect in photonic crystal (PC) silicon waveguide. b) Diagram of the photonic crystal structure employed for the nanofabrication of the Mach-Zehnder interferometer, from [30].

ferent thickness and deposited through different techniques. The largest values for $\chi^{(2)}$ are obtained for a 150 nm thick SiN layer deposited through Low Pressure Chemical Vapour Deposition (LPCVD) technique resulting in a 1.2 GPa intrinsic stress that generated a sign inversion of the strain across the waveguide silicon core. The observed strong dependence of $\chi^{(2)}$ on the extent and the anysotropy of the induced strain field induced the authors to suggest that such a second-order susceptibility is mainly caused by the spatially inhomogeneous distribution of the crystalline deformation.

Chmielak at al demonstrated a fully integrated electro-optic Mach-Zehnder modulator based on strained SOI rib waveguide and obtainined a second-order susceptibility value of $\chi^{(2)} = 122\,pm/V$[32][33]. The considerable enhancement in the nonlinearity values in comparison to the one observed in [30] is due to fundamental differences in the device design and processes. Firstly the rib layout allows the formation of an asymmetric strain with regard to the PCW of [30] and the silicon nitride film is deposited through remote plasma-enhanced chemical vapour deposition (RPECVD) directly on the top of the waveguide. Furthermore an annealing step is added to the manufacturing processes that increased to the magnitude of the thermal stress. The electro-optic charachterization yields a strict linear dependence between the refractive index change and the applied voltage demonstrating the presence of the Pockels effect. The results of Micro-Raman spectroscopy analysis carried on strained SOI devices show the presence of the Pockels effect is mainly determined by the spatial strain gradient across the waveguide. This outcome confirmed the hypothesis suggested on the fundamental role played by inhomoegenous spatial strain distribution in the formation of the second-order nonlinearities.

Azadeh at al [37], highlighted the influence of the capacitely-induced free carrier effect in the electro-optical properties of strained silicon devices. Despite in the previous papers these effect had never been considered, the authors

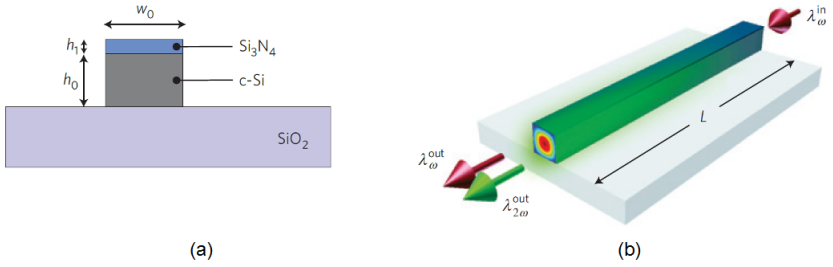

Figure 1.4: Strained SOI waveguide used in [31] for the SHG measurements. (a) Cross-section of the strained SOI waveguide. (b) Representation of the second-harmonic generation: a radiation at a wavelength λ_ω is injected into the strained SOI waveguide and two pulses, at wavelengths λ_ω and $\lambda_{2\omega}$ are observed at the output of the waveguide.

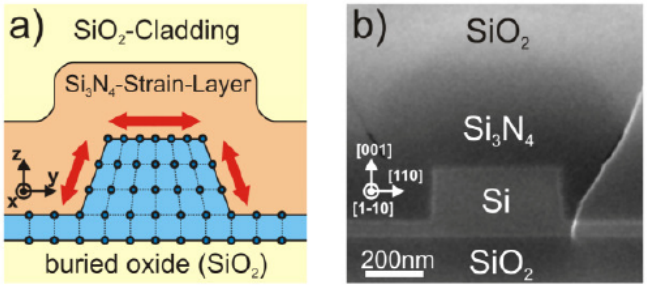

Figure 1.5: a) Schematic cross sectional view of crystalline deformation of the SOI rib-waveguide with a Si_3N_4 strain layer and a SiO_2 cladding, employed in [32]. b) A scanning electron microscope (SEM) picture of the structure.

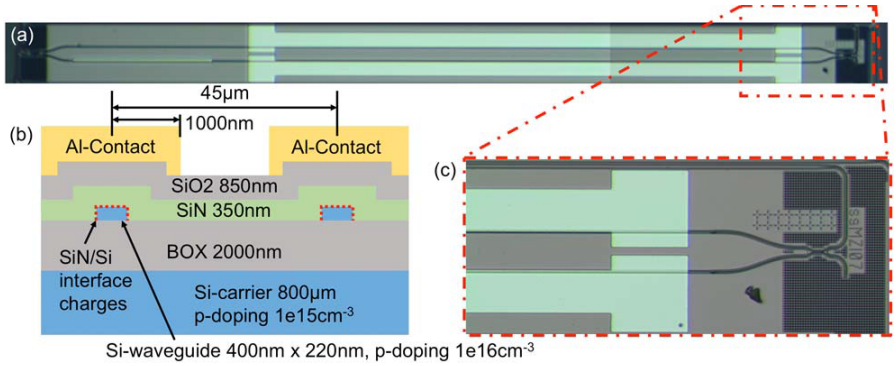

Figure 1.6: Mach-Zehnder interferometer employed in [37] for the analysis of the capacitely-induced free carrier effect (a) Layout of the Mach–Zehnder interferometer used for the experiments, (b) cross section of the capacitive structure of the and (c) particular of the waveguide junction.

demonstrate that in the devices studied in [30, 31, 32, 33] they affect severely the response of the material to an applied voltage. In particular, the Si_3N_4 stressing film accumulates surface charge due to the presence of defects at the $Si - SiN$ interface that are generated by the Si dangling bonds. Positively charged defects are thermodinamically favored over the neutral or negatively charged state but their polarity can be inverted by applying a strong positive voltage[34][35]. As demonstrated by Sharma[36], the silicon free carrier redistribution, due to the presence of the fixed charge, can induce a shielding effect on an external electric field reducing the interaction of silicon with the capacitively applied bias fields. In [37] the analysis was carried out on a Mach Zhender interferometer based on (400×200) nm SOI waveguide strained by a350 nm thick silicon nitride layer deposited through LPCVD. The experimental analysis shows an hysteresis in the phase shift response if the applied voltage sweep from -200 V to 200 V and an accompanying variation loss. These outcome are ascribable to a polarity inversion of the surface defects and to the variation of the free carriers absorption-induced propagation loss. The results highlight the necessity of taking into account these effects in the interpretation of the electro-optical measurements since under some circumstances they can cancel or reduce the stress-induced response of the device.

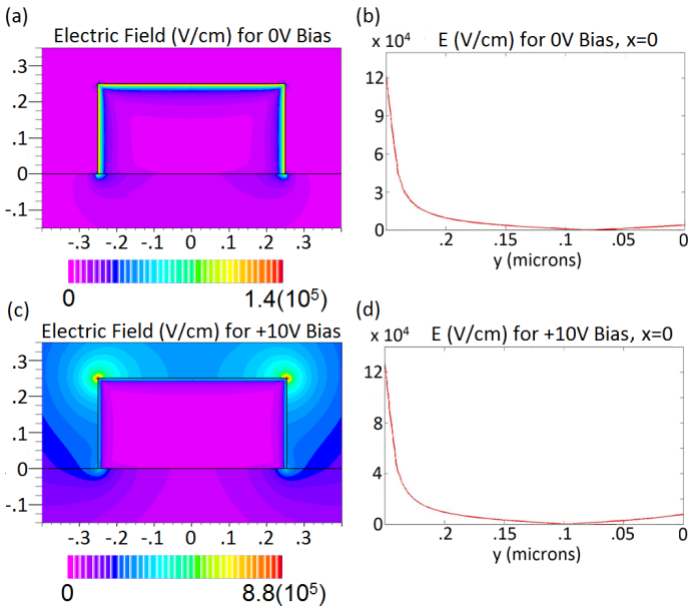

Figure 1.7: Simulative estimation of electric field distribution within strained SOI waveguide, considering the presence of the fixed charge and assuming vertical bias voltages of either $-10\,V$ (above) or $+10\,V$ (below), from [36].

Chapter 2

Theory and simulative methods

2.1 Mechanical properties of silicon

As described in Chapter 1, the presence of lattice deformation in micrometric and submicrometric optical devices can dramatically affect their performance: strained silicon structures, for example, exhibit significant values Pockels effect and second order nonlinearities which are not present in pure silicon. The theoretical framework of the simulative and experimental analysis which we have carried out on strained silicon technology is provided by the theory of elasticity; such theory studies how solid bodies deform and become internally stressed due to the applications of forces. In this section the fundamental quantities used to describe the deformation and the force distribution of a solid are introduced and the dynamic equations employed in the simulative models are described.

The theory of elasticity studies the mechanics of solid bodies regarded as continuous media. When forces are applied on solid bodies, the positions of its atoms or molecules change so that a new state of equilibrium is achieved. Given r the radius of the position of a point and r' its position after the deformation, the displacement of this point $u(r)$ is expressed by the difference between the two radii[38]:

$$u(x, y, z) = r'(x, y, x) - r(x, y, z) \tag{2.1}$$

This tensor field is called displacement vector field and represents a mathematical description of the deformation of a solid: if the values of this tensor are given as a function of the position, the deformation of the solid is entirely determined.

When a deformation is present in the body, the distances between its points change. Given the radius vector joining two points $dl' = (dx'_1 dx'_2, dx'_3)$ and the vector joining the same two points in the undeformed body, $dl = (dx_1 dx_2, dx_3)$, the difference between the modules is given by:

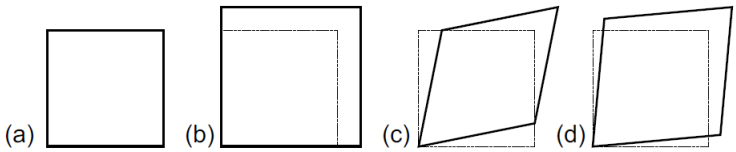

Figure 2.1: Deformation of a square structure (a). (b) Pure hydrostatic deformation ($xy = 0$), (c) pure shear deformation ($xx = yy = 0$), and (d) mixed deformation, from [39].

$$dl'^2 = dl^2 + 2u_{ik}dx_i dx_k \tag{2.2}$$

where u_{ik} is the strain tensorial field is defined as:

$$u_{ik}(x, y, z) = \frac{1}{2}(\frac{\partial u_i}{\partial x_k} + \frac{\partial u_k}{\partial x_i} + \frac{\partial u_i}{\partial x_k}\frac{\partial u_k}{\partial x_i}) \tag{2.3}$$

Since the strain tensor is symmetrical, i.e. $u_{ik} = u_{ki}$, at any given point it's possible, by a proper choice of the coordinate axis, said principal axes, to diagonalize the tensor. In this way only the diagonal terms $u^{(1)}, u^{(2)}, u^{(3)}$, named principal values of the strain tensor, are different from zero. The vector dl' can therefore be expressed as:

$$dl'^2 = (1 + 2u^{(1)})dx_1^2 + (1 + 2u^{(2)})dx_2^2 + (1 + 2u^{(3)})dx_3^2 \tag{2.4}$$

It can be shown that the induced change of an infinitesimal volume dV can be expressed in terms of the sum of the diagonal components of the the strain tensor:

$$dV' = dV(1 + u_{11} + u_{22} + u_{33}) \tag{2.5}$$

The sum of the diagonal terms, called trace $Tr(u)$, is invariant to any change of the co-ordinate system and represents the relative volume change $Tr(u) = \frac{dV'-dV}{dV}$.

The diagonal coefficients of the strain tensor describe a deformation along the main axis which doesn't change the shape of a volume (hydrostatic deformation). On the other hand, the non-diagonal coefficients, said shear strain components, represent the gradient of the displacement vectors along a transverse direction and describe a deformation the alters the shape of the the volume but not its area (shear deformation)[39]:

As described, when a solid body is deformed, the original arrangement of the atoms or of the molecules is altered. This new disposition gives rises to stresses that tend to return the body to the original equilibrium state. Such stresses are due to the forces of interactions between the atoms and molecules and are said internal forces. Singe the range of actions of these forces is really small, the internal forces exerted on a portion of the body act only on the surfaces

surrounding the infinitesimal volume. Given F_i the components of the internal forces acting on a infinitesimal volume dV, the total force acting on the portion is given by

$$\int F_i dV \tag{2.6}$$

Expressing the components $F_i$as a divergence of a vector σ_{ik}, the Green's theorem can be applied and the force exerted on the volume can be expressed as surface volume:

$$\int F_i dV = \int \frac{\partial \sigma_{ik}}{\partial x_k} dV = \sigma_{ik} ds_k \tag{2.7}$$

where ds_k is the surface element vector directed along the outward normal.

The tensor σ_{ik} is called stress tensor and represents the i_{th} component of the internal forces acting on a surface oriented along the axis k. Under conditions of equilibrium, the sum of the forces acting on each part of the body is zero and if no external forces are applied this conditions gives:

$$\nabla \cdot [\sigma_{ik}] = 0 \tag{2.8}$$

If external forces are present, the relative volume density F_{ext}must be balanced by the internal forces:

$$F_{ext} = -\nabla \cdot [\sigma_{ik}] \tag{2.9}$$

Eq. (2.9) can be expressed in terms of the tensor L:

$$F_{ext} = -L^T [\sigma_{ik}] \tag{2.10}$$

where

$$L = \begin{bmatrix} \frac{\partial}{\partial x} & 0 & 0 & \frac{\partial}{\partial y} & 0 & \frac{\partial}{\partial z} \\ 0 & \frac{\partial}{\partial y} & 0 & \frac{\partial}{\partial x} & \frac{\partial}{\partial z} & 0 \\ 0 & 0 & \frac{\partial}{\partial z} & 0 & \frac{\partial}{\partial y} & \frac{\partial}{\partial x} \end{bmatrix} \tag{2.11}$$

The reaction of a solid to internal stress depends on the crystal symmetry of the lattice and on the length and orientation of the atomic bonds. Stress and strain tensor components are usually related by constitutive equations in terms of the stiffness and compliance constants which are experimentally determined.

The elastic properties of an anisotropic material are therefore described by the fourth rank tensors stiffness tensor c_{ijkl} and compliance tensor s_{ijkl} relating stress tensor σ_{ij} and ε_{ij}[40]:

$$\sigma_{ij} = c_{ijkl} \varepsilon_{kl} \quad \varepsilon_{ij} = s_{ijkl} \sigma_{kl} \tag{2.12}$$

Due to the the symmetry of the stress and strain tensors, $\sigma_{ij} = \sigma_{ji}$ and $\varepsilon_{ij} = \varepsilon_{ji}$, most of the elastic constants are equal, and the number of independent elements reduce to 21. For orthotropic material as silicon, i.e. material having at least two orthogonal planes of symmetry, the constitutive relation between

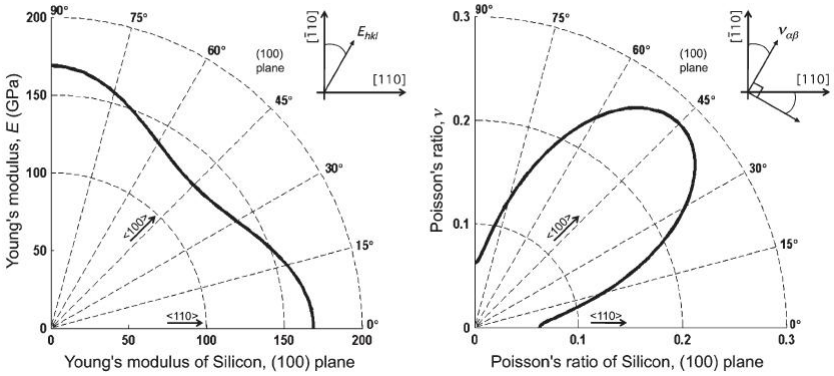

Figure 2.2: Young's modulus and Poisson's ratio versus orientation in silicon, from [41].

the strain and stress tensor can be expressed in terms of the elasticity quantities of Young's modulus E, Poisson's ratio ν and the shear modulus G as[41]:

$$\begin{pmatrix} \varepsilon_{xx} \\ \varepsilon_{yy} \\ \varepsilon_{zz} \\ \varepsilon_{yz} \\ \varepsilon_{xz} \\ \varepsilon_{xy} \end{pmatrix} = \begin{pmatrix} 1/E_x & -\nu_{yx}/E_y & -\nu_{zx}/E_z & 0 & 0 & 0 \\ -\nu_{xy}/E_x & 1/E_y & -\nu_{xz}/E_z & 0 & 0 & 0 \\ -\nu_{xz}/E_z & -\nu_{yz}/E_y & 1/E_z & 0 & 0 & 0 \\ 0 & 0 & 0 & 1/G_{yz} & 0 & 0 \\ 0 & 0 & 0 & 0 & 1/G_{xz} & 0 \\ 0 & 0 & 0 & 0 & 0 & 1/G_{xy} \end{pmatrix} \begin{pmatrix} \sigma_{xx} \\ \sigma_{yy} \\ \sigma_{zz} \\ \sigma_{yz} \\ \sigma_{xz} \\ \sigma_{xy} \end{pmatrix} \tag{2.13}$$

where E_i, ν_{ij} and $G_{yz}$are defined with regard to the axes of interest. In Fig 2.2, the values of Young's modulus and Poisson's ration as a function of orientation for the (100) plane, obtained through measurements of acoustic waves propagation, are reported.

In the silicon wafer employed for the manufacturing of the structures which we analyzed in this work, the primary flat is aligned with the [110] direction and the frame of reference is the one indicated in Fig 2.3. The elasticity values and stiffness matrix coefficients are:

$$E_x = E_y = 169\ GPa \quad E_z = 130\ GPa \tag{2.14}$$

$$\nu_{yz} = 0.36 \quad \nu_{zx} = 0.28 \quad \nu_{xy} = 0.064 \tag{2.15}$$

$$G_{yz} = G_{zx} = 79.6\ GPa \quad G_{xy} = 50.9\,GPa \tag{2.16}$$

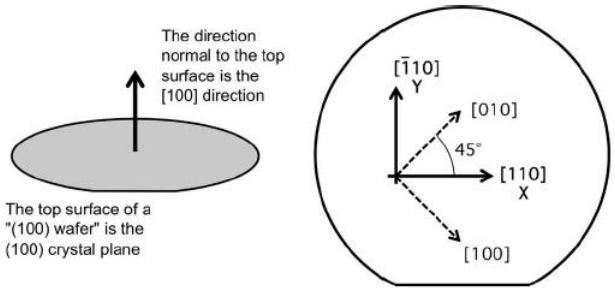

Figure 2.3: Crystal orientation in the silicon wafers, from [41].

$$C = \begin{pmatrix} 194.5 & 35.7 & 64.1 & 0 & 0 & 0 \\ 35.7 & 35.7 & 64.1 & 0 & 0 & 0 \\ 64.1 & 64.1 & 165.7 & 0 & 0 & 0 \\ 0 & 0 & 0 & 79.6 & 0 & 0 \\ 0 & 0 & 0 & 0 & 79.6 & 0 \\ 0 & 0 & 0 & 0 & 0 & 79.6 \end{pmatrix} \tag{2.17}$$

The orthotropic stiffness tensor, given by Eq. 2.17, will be used in the simulative estimations of the stress and strain distribution of the manufactured silicon rib structures.

2.2 High intrinsic stress films in silicon devices

As will be described in Chapter 3, the lattice deformation of the manufactured devices has been induced through the deposition of a thin stoichiometric silicon nitride (Si_3N_4) layer. Chemical vapor deposited Si_3N_4 layers are commonly used in microelectronic devices as diffusion barriers and passivation layer or as dielectric materials due to the electrical properties and resistance to chemical attack[42]. Silicon nitride is also one of the basic structural materials in micro electro-mechanical systems (MEMS) devices due to its mechanical properties: extreme aspect ratio structures like long cantilevers or large membranes can be built of thin silicon nitride films[43]. Recently, after the discover of Jacobsen at al [30]reported in Chapter 2, Si_3N_4 has been employed in SOI opto-electronic devices as a stressing layer film capable of inducing significant deformation on the waveguides structures.

When thin films are deposited on a substrate, a certain amount of stress, named residual stress, can arise. Residual stress, in thin films, is usually modeled as a biaxial stress. Under this assumption, the shear stress and the components in the direction orthogonal to the interface are assumed negligible in comparison to the other stress components and are equated to zero, i.e. $\sigma_{xy} = \sigma_{xy} = \sigma_{zz} = 0$, where the coordinate system is indicated in Fig. 2.4. Since the stress lies only in the film plane, the stress tensor can be expressed as a 2×2 matrix:

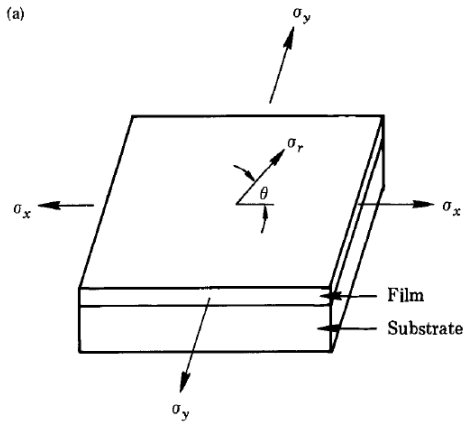

Figure 2.4: Biaxial stress in a thin film deposited on a substrate.

$$\sigma = \begin{pmatrix} \sigma_{xx} & 0 \\ 0 & \sigma_{yy} \end{pmatrix} \tag{2.18}$$

The nature (tensile or compressive) and intensity of the residual stress is determined by the interaction of the film with the substrate (extrinsic stress) and the chemical and physical variation of the thin film during the deposition (internal stress):

$$\sigma_{res} = \sigma_{int} + \sigma_{ext} \tag{2.19}$$

Both intrinsic and extrinsic contributes are strongly dependent on the type of deposition process which are employed as well as on the experimental nanofabtication parameters.

The extrinsic stress is mainly determined by the mismatch of thermal expansion between the film and the substrate upon cooling from the deposition temperature to ambient[44]. For the manufactured structures, the Si_3N_4 is deposited through Low Pressure Chemical Vapor Deposition (LPCVD) at 780 C°. When the structure is brought to room temperature, the films and substrate shrink. Since the film is attached to the substrate, the strain of the film, ϵ_{film} is expected to be that of the substrate:

$$\epsilon_{film} = -\alpha_s \triangle T \tag{2.20}$$

where α_f is the thermal expansion coefficient (CET) of the substrate and $\triangle T$ is the difference between the deposition temperature and the room temperature. On the other hand, the strain of the unattached film at room temperature would be:

$$\epsilon_{film,un} = -\alpha_f \triangle T \tag{2.21}$$

where α_s is the thermal expansion coefficient of the film. This mismatch leads to a stress in the film, called thermal stress σ_{th}, given by:

$$\sigma_{th} = \frac{E}{1-\nu}(\epsilon_{film} - \epsilon_{film,un}) = \frac{E}{1-\nu}(\alpha_f - \alpha_s)\triangle T \tag{2.22}$$

where E and v are the (isotropic) Young's modulus and Poisson's ratio of Si_3N_4[45]. If $\alpha_f > \alpha_s$ the thermal stress is positive (tensile), if the $\alpha_f < \alpha$ is negative, (compressive).

Let's consider the thermal expansion coefficient of the materials involved in the manufactured devices:

Silicon	Silicon Dioxide	LPCVD Silicon Nitride
$2.61 \cdot 10^{-6}$	$0.52 \cdot 10^{-6}$	$2 \cdot 10^{-6}$

The mismatch between the CET of silicon and silicon nitride is quite small, and generates, using deposition temperature, of 780°, an extrinsic compressive stress of:

$$\sigma_{ext} = -75\, MPa \tag{2.23}$$

As will be described in the next section, this value gives a negligible contribute to the overall residual stress value of the film.

On the other hand the large mismatch between the silicon and silicon dioxide CET leads to a significant compressive stress in silicon dioxide layer the must be taken into account for the analysis of the SOI waveguides.

The intrinsic stress is due to many factors; in particular, the technique of deposition, the chemistry employed and the conditions of deposition affect dramatically the residual stress [46, 47, 48]. For silicon nitride films, stress values sweeping from$-3\ GPa$ to $+1.6\ GPa$, have been reported in the literature due to the employment of different deposition techniques.

A fundamental role in the determination of the nature and amount of intrinsic stress is played by the $Si-$richness of the silicon nitride film. Fig 2.5 reports the values of residual stress versus refractive index of silicon nitride film, which is deposited through Low Pressure Chemical Vapor Deposition (LPCVD), Plasma Enhanced Chemical Vapor Deposition (PECVD), Atomic Layer Deposition (ALD) and Rapid Thermal Chemical Vapor Deposition (RTCVD), from[49]
.

The trend observed in the relationship between the stress and the refractive index highlights the influence of the chemical composition obtained, that is the Si/N ratio, on the the mechanical properties. All the experimental data lie in a straigth line which described a linear correlation between the residual stress values and the refractive index, i.e. to density of the material. This can be explained in this way: on one hand the increase of the Si-richness results in higher density, since silicon is more dense than nitrogen, and therefore in higher refractive index. On the other hand, the $Si-N$ chemical bonds, that are stretched due to the different bond length with regard to the substrate, are replaced by $Si-Si$ bonds. This implies that the mean stress generated by different bond length of $Si-Si$ and $Si-N$ bonds is reduced.

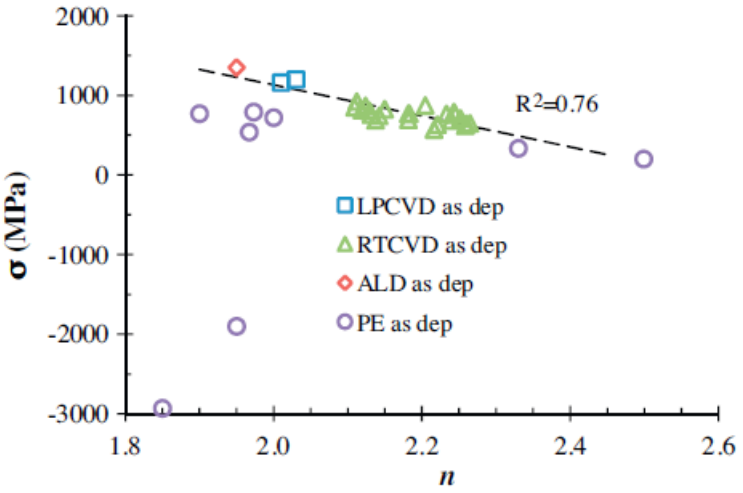

Figure 2.5: Intrinsic stress values versus refractive index n for the LPCVD (square), ALD (lozenge), RTCVD (triangle) and PECVD (circle) films, from [49].

The deposition technique employed for the microfabrication and nanofabrication of the structures analyzed is the Low Pressure Chemical Vapor Deposition (LPCVD). This technique assures uniform density in the layer and the stoichiometry of the chemical composition[50]. The residual stress obtained through this deposition technique is positive, i.e. tensile stress is observed, and of the order of $1 - 1.2GPa$. Comparing these values with the contribute of the extrinsic stress, it's clear that the main contribute to the residual stress is given by the intrinsic stress.

2.3 Electro-optic effect in silicon

The electro-optic effect is the modification of the optical property of a medium in response to an external static or slowly varying electric field. This effect encompasses several phenomena describing the variation of the imaginary part of the refractive index, such as Franz-Keldysh effect, Quantum-Stark effect and other describing the change in the real part of the refractive index such as Pockels effect and Kerr effect. In the Pockels effect, the change in the refractive index of the medium is proportional to the applied electric field. The Pockels effect is exploited in electro-optic modulator employing nonlinear crystal material as Deuterated potassium dihydrogen phosphate (KD_2PO_4) and lithium niobate ($LiNbO_3$).

As described in Chapter 1, the symmetry of silicon crystal prohibits the existence of Pockels effect. In this section, such property will be demonstrated

on the basis of simple symmetry considerations. In order to do so, it is necessary to introduce some tensorial quantities which will be useful for the description of the optical properties of anisotropic materials.

The dielectric properties of the medium can be described through the electric permettivity tensor ϵ_{ij} that relates the components of the electric flux density D_i and the components of electric field E_j in a medium[51]:

$$D_i = \epsilon_{ij} E_j \tag{2.24}$$

The impermeability tensor η_{ij} is defined by:

$$\eta_{ij} = \epsilon_0 \epsilon_{ij}^{-1} \tag{2.25}$$

and contains important information on the optical properties of the material. In particular, the coefficientsη_{ij} can be used to determine the refractive index of electromagnetic waves propagating in the medium with arbitrarily polarization through a simple geometric construction called optical index ellipsoid or optical indicatrix.

The index ellipsoid is the quadratic representation of the electric impermeability tensor η:

$$\sum_{ij} \eta_{ij} x_i x_j = 1 \tag{2.26}$$

Using the principal axes as a coordinate system, the index ellipsoid is described by:

$$\frac{x_1^2}{n_1^2} + \frac{x_2^2}{n_2^2} + \frac{x_3^2}{n_3^2} = 1 \tag{2.27}$$

where $1/n_1^2$,$1/n_2^2$,$1/n_3^2$ are called the principal values of the tensor η. A schematic representation of the index ellispoid and of the principal values of the tensor η is given in Fig 2.6.

The index ellipsoid is used for determining the refractive index of a the material in a simple way. Let's consider a wave propagating in the direction indicated by the versor u with a polarization oriented as the versor p (see Fig. 2.7). Intersecting the plane normal to the direction of propagation u with index ellipsoid, one obtains an ellipse, called the index ellipse. It can be shown that the half lengths of the major and minor axes of the ellipse are the refractive index n_a and n_b of the wave propagating along the direction u with the polarization oriented with the direction of the axes, called normal modes. The refractive index of the electromagnetic waves with arbitrarily polarization can be obtained through the decomposition as as sum of the normal modes.

It's clear that the impermeability tensor represents a generalization of the refractive index for optical anisotropic material and a change in its components results in a variation of the "anisotropic" refractive index of the material. In order to take into account the variation of the impermeability tensor, and consequently of the refractive index, in response to the application of a steady electric

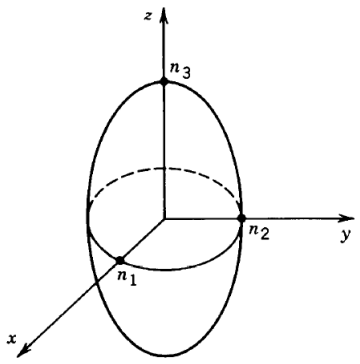

Figure 2.6: Schematic representation of the index ellipsoid, from [51].

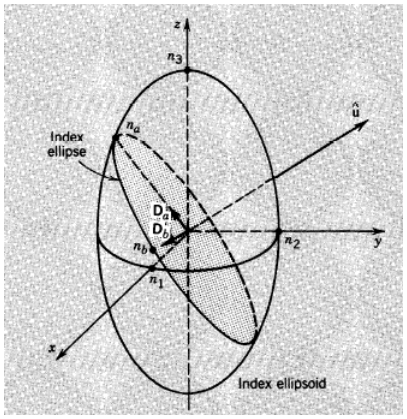

Figure 2.7: Normal modes of the crystal, determined by the index ellipsoid, from [51].

field E, each coefficient of the impermeability tensor η can be expanded in a Taylor's series around the steady electric field values$E = 0$:

$$\eta_{ij}(E) = \eta_{ij} + r_{ijk}E_k + s_{ijkl}E_kE_l \tag{2.28}$$

where E represents the applied electric field components, i.e. $E = (E_1, E_2, E_3)$ and $\eta_{ij} \equiv \eta_{ij}(0)$. The elements $\{r_{ijk}\}$are known as the linear electro-optic or Pockels coefficients and are given by $r_{ijk} = \frac{\partial \eta_{ij}}{\partial E_k}(0)$ while the elements $\{s_{ijk}\}$are known as quadratic electro-optic or Kerr effect coefficients and are given by $s_{ijk} = \frac{\partial^2 \eta_{ij}}{\partial E_k^2}(0)$.

According to the Neumann's principle[52], if a crystal is invariant with respect to certain symmetry operations, any of its physical properties must also be invariant with respect to the same symmetry operations. Silicon crystal lattice is centrosymmetric, i.e. is invariant under the inversion of the coordinates, $r \to -r$. Requiring that the impermeability tensor is invariant under this transformation, it's possible to demonstrate that the third rank tensor $\{r_{ijk}\}$vanishes. This implies that the crystal symmetry prohibits the linear response of the material to the application of the electric field: the Pockels effect is not observed in pure silicon.

In strained silicon, as described in Chapter 1, second order nonlinearity effects, such as second harmonic generation (SHG), accompany the presence of Pockels effect. The relation between the Pockels effect and second order nonlinearities in centrosymmetric and non centrosymmetric media can be explained through a microscopic model which employs an extended Lorentz model of the atom[53].

The canonical Lorentz model, that treats atom as a harmonic oscillator, provides a good description of linear optical properties of vapors and nonmetallic solids. Introducing nonlinear contributes in the restoring force exerted on the electron, it's possible to take into account the possibility of interaction between fields oscillating at different wavelengths.

Let's take the equation of motion for the electron position x to be of the form, for 1-D case:

$$m\frac{\partial^2 x}{\partial t^2} + 2\gamma\frac{\partial x}{\partial t} + F_{rest} = -qE \tag{2.29}$$

where m and q are the mass and the charge of the electron respectively and γ the dipole damping rate. F_{rest} is the restoring force on the electron and E is the electric field.

For a noncentrosymmetric medium, the resorting force contains a term with an even power of x since the potential function $U(x) = -\int F_{rest}dx$ is not symmetric, i.e. $U(x) \neq U(-x)$, Fig. 2.8

$$F_{rest} = -m\omega_0^2 x - m\,a\,x^2 \tag{2.30}$$

Let's consider a sufficiently weak applied field, $E = \lambda E$ where λ is a parameter ranging between 0 and 1, and an electric field containing terms oscillating

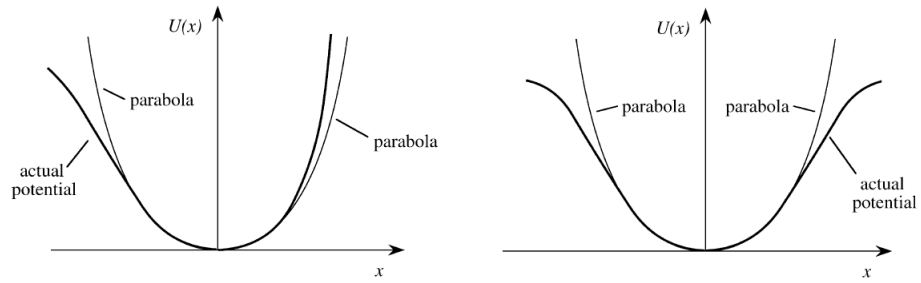

Figure 2.8: Potential energy function for a noncentrosymmetric medium (left) and centrosymmetric medium (right), from [53].

at frequency $\omega_1$and ω_2, $E = E_1 e^{i\omega_1 t} + E_2 e^{i\omega_2 t} + c.c.$ We seek a solution in the form of a power series expansion in strength λ:

$$x = \lambda x^{(1)} + \lambda^2 x^{(2)} + \lambda^3 x^{(3)} + ... \tag{2.31}$$

In order for the function given by Eq. (2.31) to be a solution of Eq. (2.29) for any value of the coupling strength λ, the terms proportional to λ, λ^2 andλ^3 must separately satisfy the equation.

These requirements lead to the following equations for the coefficients $x^{(i)}$:

$$\frac{\partial^2 x^{(1)}}{\partial t^2} + 2\gamma \frac{\partial x^{(1)}}{\partial t} + \omega_0^2 x^{(1)} = -\frac{qE}{m} \tag{2.32}$$

$$\frac{\partial^2 x^{(2)}}{\partial t^2} + 2\gamma \frac{\partial x^{(2)}}{\partial t} + \omega_0^2 x^{(2)} + a[x^{(1)}]^2 = 0 \tag{2.33}$$

$$\frac{\partial^2 x^{(3)}}{\partial t^2} + 2\gamma \frac{\partial x^{(3)}}{\partial t} + \omega_0^2 x^{(3)} + 2a x^{(1)} x^{(2)} = 0 \tag{2.34}$$

The lowest order contribution $x^{(1)}$ is governed by the equation of the linear Lorentz model. It's steady state solution is:

$$x^{(1)} = -\frac{qE_1}{mD(\omega_1)} e^{(-i\omega_1 t)} + -\frac{qE_2}{mD(\omega_2)} e^{(-i\omega_2 t)} + c.c \tag{2.35}$$

where

$$D(\omega_j) = \omega_0^2 - \omega_j^2 - 2i\omega_j\gamma \tag{2.36}$$

The expression for $x^{(1)}$ is then squared and inserted in Eq. (2.33). The square of $x^{(1)}$, contain oscillations at frequencies $\omega^{(2)} = \pm 2\omega_1, \pm 2\omega_2, \pm(\omega_1 + \omega_2), \pm(\omega_1 - \omega_2), 0$. This implies that second-order contribution $x^{(2)}$ contains terms oscillating at these frequency. The contribute given by the coefficients $x^{(2)}$ to the second order polarization at frequency ω_i , is:

$$P^{(2)}(\omega_i) = -Nqx^{(2)}(\omega_i) \tag{2.37}$$

where $x^{(2)}(\omega_i)$ is the coefficients $x^{(2)}$ oscillating at frequency ω_i and ω_i is one of the possible frequency values of $\omega^{(2)}$.

On the other hand, the second order susceptibility $\chi^{(2)}(\omega_i)$ is defined through the relation:

$$P^{(2)}(\omega_i) = \varepsilon_0 \chi^{(2)}(\omega_i) E(\omega_1) E(\omega_2) \tag{2.38}$$

Comparing (37) and (38) it's clear that nonlinear susceptibilities of the second order can be observed in noncentrosymmetric medium.

For centrosymmetric media, for the reasons explained above, the restoring force assumes the form:

$$F_{rest} = -m\omega_0^2 x + mbx^3 \tag{2.39}$$

Following the same considerations for the noncentrosymmetric medial we obtain analogous equations for $x^{(1)}$. Nevertheless, the equation for $x^{(2)}$ is different since the electronic oscillator is dumped and not driven:

$$\frac{\partial^2 x^{(2)}}{\partial t^2} + 2\gamma \frac{\partial x^{(2)}}{\partial t} + \omega_0^2 x^{(2)} = 0 \tag{2.40}$$

This implies that steady state solution for Eq. (2.40) vanishes and no contributions to second-order polarization are obtained. An important result is obtained from this analysis: second-order effects are not permitted in centrosymmetric media and the lowest-order nonlinear response, generated from the restoring force, is a third order contribution.

Now, the linear electro-optic effect can be described in terms of a second order non linear polarization that mediates the interaction between a static field E_0, oscillating at frequency $\omega_1 = 0$, and the optical field E_ω oscillating at frequency $\omega_2 = \omega$. The change in the complex dielectric constant due to the polarization term $P_\omega^{(2)}$ generated by $x^{(2)}$term is given by:

$$\Delta\varepsilon = \frac{P_\omega^{(2)}}{\varepsilon_0 E_2} = \chi^{(2)}(\omega_i = \omega + 0) = \frac{-aNq^3 E_0}{\varepsilon_0 m^2 \omega_0^2 (\omega_0^2 - \omega^2 - i\omega\Gamma)^2} \tag{2.41}$$

The variation of the dielectric constant is proportional to the static electric field E_0. It can be easily shown that the resulting variation in the refractive index is proportional to E_0 as well. This analysis shows that the Pockels effect is mediated by the second order nonlinearity and can be therefore considered a second order effect.

2.4 Photoelastic effect in silicon

As described above, the centrosymmetric crystals do not not show Pockels effect. On the other hand, the presence of a perturbation to the perfectly periodic atomic arrangement breaks the crystal symmetry and enables the presence of this effect. On a microscopic scale, when a material is subject to mechanical distortions, such as the stress induced on silicon by the deposition of a straining Si_3N_4 film, the resulting deformation changes the bond length between the atoms. The perturbation in binding force of the electrons to atoms generates a change in the optical properties: this phenomenon is said photoeleastic effect.

If a material is deformed, the impermeability changes so that the tensor components η_{ij} become a function of the strain tensor components ε_{kl}, i.e.$\eta_{ij} \equiv \eta_{ij}(\varepsilon_{kl})$. In analogy with the expression of the impermeability tensor in terms of an applied field, the components η_{ij}can be expanded in a Taylor's series about $\varepsilon_{kl} = 0$[51]:

$$\eta_{ij}(\varepsilon_{kl}) = \eta_{ij} + p_{ijkl}\varepsilon_{kl} \tag{2.42}$$

where constants $p_{ijkl} = \frac{\partial \eta_{ij}}{\partial \varepsilon_{kl}}$ form the fourth rank tensor known as photoelastic or strain-optic tensor.

In cubic crystals, as silicon, only 3 components of photoelastic tensor are non-vanishing and the variation of the refractive index with the contracted tensor notation is given by[54]:

$$\triangle \begin{bmatrix} 1/n^2_{xx} \\ 1/n^2_{yy} \\ 1/n^2_{zz} \\ 1/n^2_{yz} \\ 1/n^2_{xz} \\ 1/n^2_{xy} \end{bmatrix} = \begin{pmatrix} p_{11} & p_{12} & p_{12} & 0 & 0 & 0 \\ p_{12} & p_{11} & p_{12} & 0 & 0 & 0 \\ p_{12} & p_{12} & p_{11} & 0 & 0 & 0 \\ 0 & 0 & 0 & p_{44} & 0 & 0 \\ 0 & 0 & 0 & 0 & p_{44} & 0 \\ 0 & 0 & 0 & 0 & 0 & p_{44} \end{pmatrix} \begin{pmatrix} \varepsilon_{xx} \\ \varepsilon_{yy} \\ \varepsilon_{zz} \\ \varepsilon_{yz} \\ \varepsilon_{xz} \\ \varepsilon_{xy} \end{pmatrix} \tag{2.43}$$

where p_{11}, p_{12} and $p_{44}$are the photoelastic coefficients. The pair of indices (i, j) and $(k.l)$ have been renamed as single index in accordance with table:

j (or l)	i (or k): 1	2	3
1	1	6	5
2	6	2	4
3	5	4	3

From Eq. (2.43) the strain-induced refractive index change for light polarized along the principal axis can be obtained:

$$n_i - n_0 = -\frac{1}{2} n_0^3 p_{ij} \varepsilon_{ij} \tag{2.44}$$

with $i = 1, 2, 3$. For waveguide structures the plane strain approximation is employed: since the waveguide is usually very long in the propagation direction z , the shear strain in this direction can be ignored. Using the stress and strain relation, the expression for the refractive index for the polarizations are given by:

$$n_x - n_0 = -C_1\sigma_x - C_2(\sigma_y + \sigma_z) \tag{2.45}$$

$$n_y - n_0 = -C_1\sigma_y - C_2(\sigma_x + \sigma_z) \tag{2.46}$$

where the stress-optic constant $C_1$and C_2 are related to the Young's modulus E, the Poisson's ratio υ and the photoelastic coefficients $p_{11}$and p_{12}as:

$$C_1 = \frac{n_0^3}{2E}(p_{11} - 2\nu p_{12}) \tag{2.47}$$

$$C_2 = \frac{n_0^3}{2E}(-\nu p_{11} + (1-\nu)p_{12}) \tag{2.48}$$

The values measured by in are reported in the table

p_{11}	p_{11}	p_{12}	$C_1(10^{-12}Pa^{-1})$	$C_2(10^{-12}Pa^{-1})$
Si	-0.101	0.0094	-17.13	5.51
SiO_2	0.16	0.27	1.17	3.73

Eq. (2.45) and Eq. (2.46) will be used in the multiphysical model which we have employed for the simulative estimations of the optical properties of the strained SOI waveguide.

2.5 Optical waveguides and propagation Losses

2.5.1 Silicon-on-insulator (SOI) waveguides

A waveguide is an optical structure that allows the confinement of light within its boundaries by total internal reflection[55]. In order for the total internal reflection to occur, the refractive index of medium where most of the radiation is concentrated n_c must be higher than the refractive index of the surrounding material n_s. The rays that travel with an angle, with respect to the interfaces, greater than the critical angle $\theta_c = sin^{-1}(n_s/n_c)$ suffer total internal reflection and remain trapped inside the film, as shown in Fig. 2.9.

Optical waveguides can be classified on the base of the number of dimensions in which the light is confined: planar waveguide (1D confinement), channel waveguide (2D confinement) and photonic crystals (3D confinement), (Fig. 2.10). If a light pulse is transferred from one point to another, the broadening of the beam in the transverse plane, i.e. in the plane orthogonal to the propagation, must be minimum. In order to avoid any spread in the transverse plane, channel waveguide are required. In Fig. 2.11 the three most common structures for channel waveguide are reported: stripe waveguide, rib waveguide and buried waveguide.

When the cross-section dimensions of the waveguide are comparable to the wavelength of the radiation, the interference between the beams reflected at the interfaces limits the possible angles of propagation. To each of the permitted angle corresponds a radiation with an electromagnetic field that maintains the

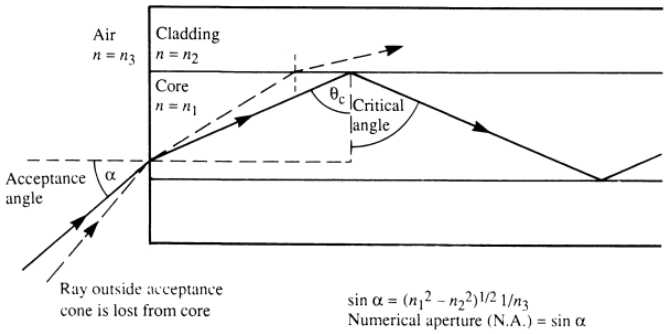

Figure 2.9: Light confinement through total internal reflection in optical waveguide, adapted from [56].

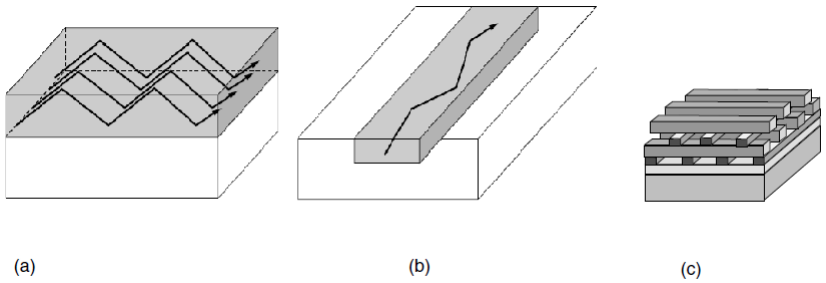

Figure 2.10: Basic types of waveguide geometries: (a) planar waveguide, (b) channel waveguide and (c) photonic crystal, from [55].

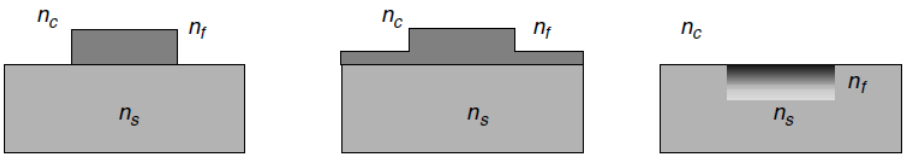

Figure 2.11: Main types of channel waveguides (2D waveguides): (a) stripe waveguide; (b) rib waveguide; (c) buried waveguide, from [55].

same transverse distribution along the propagation. These radiations propagating without diffraction are said normal modes of the waveguide[57]. The knowledge of the properties of the radiation modes in terms of propagation loss, phase and group velocity are of paramount importance in the design of a photonic circuit.

From a mathematical point of view, a normal mode represents a solution to the Maxwell harmonic equations for the waveguide in the form:

$$E(x, y, z) = E_t(x, y)e^{(i(\beta z - \omega t))} \tag{2.49}$$

where $E_t(x, y)$ is the transverse electric field distributions and β, said propagation constant, represents the wavevector along the direction of propagation. β is usually expressed in terms of the wavevector in the vacuum $k_0 = \lambda_0/2\Pi$ as:

$$\beta = k_0 \cdot n_{eff} \tag{2.50}$$

where n_{eff} is said effective refractive index of the waveguide. The boundary conditions at the interfaces, imposed by the waveguide geometry and the materials, limit the values which the propagation constant can assume. With regard to the values of the effective refractive index, the normal modes can be classified into guided modes and radiation modes. Guided modes have a discrete set of possible propagation constant and have an effective refractive index greater than the one of cladding or substrate layer. The high value n_{eff} implies that the radiation interacts mainly with the core, i.e. the radiation is well confined and propagates with no loss. The radiation modes have a continuous set of possible propagation constant values and are characterized by a non null flow of energy in the transverse direction that induces a loss in the power of the radiation along the propagation.

The reduction of the dimension of the waveguide below certain values leads to the condition at which just one guided mode is permitted. This condition is said single mode condition and for SOI stripe waveguide with rectangular shape is obtained for core dimension of about $(450 \times 220)\ nm$[58]. On the other hand, further reducing the ratio between the dimension of the waveguide and the wavelength, the guided modes tend to be progressively less confined in the core region and the cut-off region is attained: no solution to Maxwell equations in the form of guided modes are allowed[59]. The confinement of the radiation plays a fundamental role in the mechanisms underlying the propagation loss of a high-index contrast waveguide. The effects of the modal confinement on the propagation loss together with the contribute related to the effective refractive index and wavelength of the radiation are described in next section.

2.5.2 SOI waveguide propagation losses

The high index contrast in SOI waveguide allows a high confinement of the traveling radiation. The total internal reflection at the interface between the

silicon and the air or oxide cladding layer allows light to travel without diffraction inside the waveguide despite its sub-wavelength dimensions. As outlined in the previous section, for z invariant waveguide out of the cut-off condition, the mode theoretically propagates maintaining the intensity profile and conserving its power. A perfect waveguide has no loss and the totality of the modes, guided modes and radiation modes, form an orthogonal basis: no power is transferred between each other.

On the other hand, any perturbation to the waveguide section induced by nonidealities in the manufacturing processes or by the presence of sections with different geometries in the device, couples the guided mode to radiation modes and induces propagation loss. In particular, the strongest contribute is given by the light scattering induced by the roughness of the sidewalls. As a matter of fact, the photolithographic processes, in transferring the pattern of a mask onto silicon device layer, unavoidably generate corrugation on the vertical sidewalls of the waveguides[60]. The depth of the sidewall roughness is considered a stochastic process with a correlation function given by a gaussian function with variance and correlation length determined by the lithographic processes.

An analytical model, reported in [61], leads to the following expression for the propagation loss α:

$$\alpha = \frac{\sigma^2 2\Pi n_{eff}^2 h}{\lambda_0} E_s \Delta n^2 \tag{2.51}$$

where σ is the interface roughness, h is the transverse propagation constant in the core, E_s is the normalized electric field intensity at the interface and Δn is the difference between the refractive indices of core and cladding. It's worth noticing that the scattering-induced loss is expected to be weaker for longer wavelength and stronger for radiation with high intensity in correspondence of the interface.

The scattering at horizontal sidewalls is much less severe since the top and bottom surfaces of the SOI silicon device show lower values of roughness. The root mean square (RMS) square roughness is of the order of $0.1nm$ and is much smaller, approximately a order of magnitude, than the one observed at vertical sidewall. This difference is due to the chemical and mechanical polishing employed in the SOI wafers fabrication processes that smooths the surfaces to angstrom-level roughness values.

Other contributes to propagation loss given by: the surface state absorption by the silicon dangling bonds at the sidewall and the Rayleigh scattering associated to sub-wavelength perturbation of the refractive index. Furthermore, if the power carried by the guided mode is high, non-linear effects can occur such as two-photon absorption or Stimulated Raman Scattering effect (SRS) which enhance the propagation losses. Nevertheless, the sidewall roughness scattering remains the dominant effect and sets the lower limit for the propagation loss: much effort has been devoted to optimize the microfabrication process in order to reduce the surface roughness and loss values down to $2-3\,dB/cm$ have been obtained.

Figure 2.12: Simulated intensity distribution of the modal radiation of TE and TM polarization for (450×220) nm SOI strip waveguide at 1300 nm wavelength, from [62].

It can be shown, that the intensity of the coupling between two modes of a waveguide, is given by the overlap integral between the modes and the perturbation of the dielectric constant. In accordance to this consideration, the Transverse Electric (TE) mode and Transverse Magnetic (TM) mode, which are the only guided modes in a single mode SOI waveguide, are expected to be effected in a different way by the roughness scattering, (Fig. 2.12). The TE mode is confined in the vertical direction but the electromagnetic intensity outside the vertical waveguide in not negligible, due to the continuity of the displacement vector component imposed by the boundary conditions. On the contrary, the TM mode is horizontally well confined but the profile extends outside the horizontal surfaces. Therefore the overlap integral between the TE or TM mode, and the dielecric perturbation at the vertical sidewalls, are expected to be quite different.

Fig. 2.13 shows the experimental results of loss spectrum for $(445 \times 220)\, nm$ SOI stripe waveguide obtained through the employment of the cut-back method, from [62]. For wavelengths shorter than 1370 nm the losses of TM polarization are lower than those suffered by TE polarization. In this range the TM mode is out of the cut-off condition and the high confinement of the mode in the horizontal direction makes the interaction with the sidewall roughness less strong in comparison with the TE polarization case. Moving toward longer wavelengths, the TM mode reaches the cut-off condition and becomes radiative: the loss induced by the bad confinement overcome the roughness scattering contribute of the TE mode loss. As a result, in the range of wavelength longer than 1400 nm the TE losses are much smaller than those observed for TM polarization. It's worth noting that both the polarizations show a parabolic-like behavior centered around different wavelengths corresponding to their minimal losses. Such results is related to two effects: for longer wavelengths, as explained, the cut-off condition is the most important contribute to the propagation losses due to the radiant nature of the mode and its reduced confinement. On the other hand, for shorter wavelengths, the relative amplitude of the roughness over the wavelength increases and leads to an enhancement of the scattering with the mode, as expected, (see Eq. 2.51).

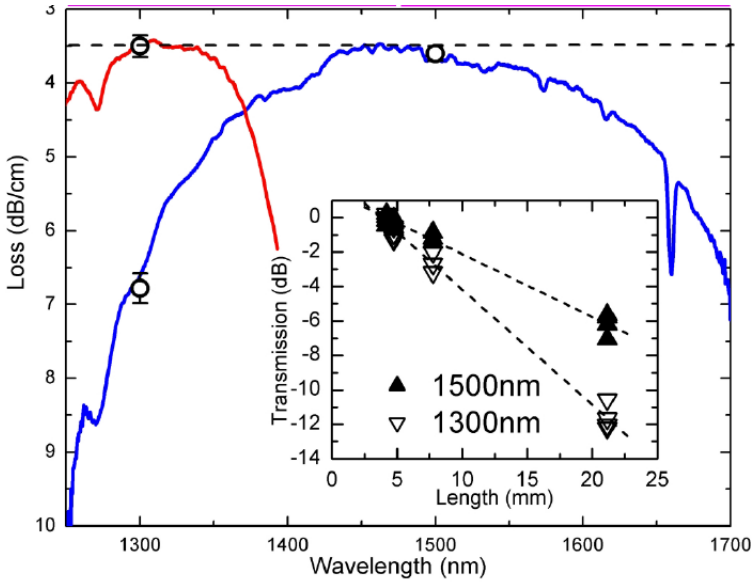

Figure 2.13: Loss spectrum for $(445 \times 220)\,nm$ SOI strip waveguide. Blue line corresponds to TE polarization and red line correspond to TM polarization, from [62].

2.5.3 Losses in SOI waveguides bends

It has been showed that guided light traveling along curved path suffers radiation losses: this contribute is commonly said bend loss and can overcome the propagation loss for not well designed devices[63]. The reason behind the bend loss can be easily understood considering a circular bend curve, as the one represented in Fig. 2.14. The radial velocity of each point of the mode increases as the distance from the axis enlarges: at some height, marked by a dashed line in figure, the evanescent field would exceeds the speed of light in the cladding layer. As this is not possible, this part of the mode curves and the energy associated is lost through radiation: i.e. part of the power carried by the fundamental mode is transferred to radiating modes. Furthermore, the bend loss is expected to be stronger for bend with smaller radius of curvature: the angular speed and the peripheral velocity of the radiation increases enhancing the radiation loss.

The bend loss α can be expresses related to the radius of curvarure R and the effective refractive index of the waveguide n_{eff} [62]:

$$\alpha = K \exp(-cR),\ c = \beta * (2\Delta n_{eff}/n_{eff})^{3/2} \tag{2.52}$$

Beside the losses induced by the curvature of the wavefront, a contribution to the bend losses is given by the enhancement of sidewall roughness scattering described in the previous section. Indeed, it can be showed that the curvature of the waveguide induced a spatial shift of the mode field distribution toward

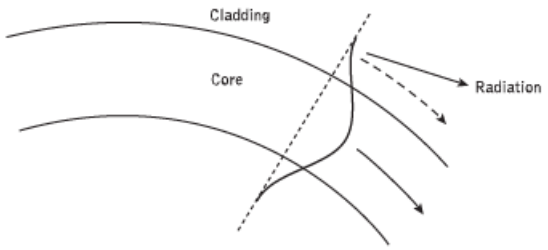

Figure 2.14: Schematic representation at a fiber bend, from [64].

the outer vertical sidewall. This implies that the fraction of radiation intensity interacting with roughness of the outer vertical sidewall increases. Since the shift of the radiation is different for TE and TM modes, as for the case of the propagation loss the two guided modes are expected to suffer different bend losses.

Fig. 2.15 reports the spectra of bending losses for SOI waveguide with the same geometry of Fig. 2.12 for different radius of curvature, from [62]. For both polarization TE and TM the bend loss increase for smaller radius of curvature but due to the high index contrast and the consequent good mode confinement the losses small: values less than 0.1 dB/turn and 0.3 dB/turn are obtained for a wide band of the spectrum analyzed and for a radius of curvature of 5 um, the losses are negligible. As for the propagation loss analysis, the obtained loss values are greter for longer wavelengths since TE and TM polarization approach to the cut-off condition. It's worth nothing that differently from the propagation losses case, the TM bend losses are higher than TE losses despite its stronger better confinement in horizontal direction. In the case of bend waveguide, the dominant effect is the difference in the overall confinement of the mode between the two polarization: for TE mode the strong confinement reduces the shift toward the outer edge in comparison with the less confined TM inducing a weaker interaction with the sidewall roughness.

2.6 Finite Element Method (FEM) numerical method

An extensive set of simulative analyses have been carried out to estimate the mechanical and electromagnetic properties of the manufactured strained silicon structures. The simulative models which we have developed and employed for such analyses are based on the Finite Element Method (FEM) numerical method. In this section, the basic principles of the FEM numerical model are provided together with a description of its application for the discretization of the differential equations which we have used in the developed simulative models.

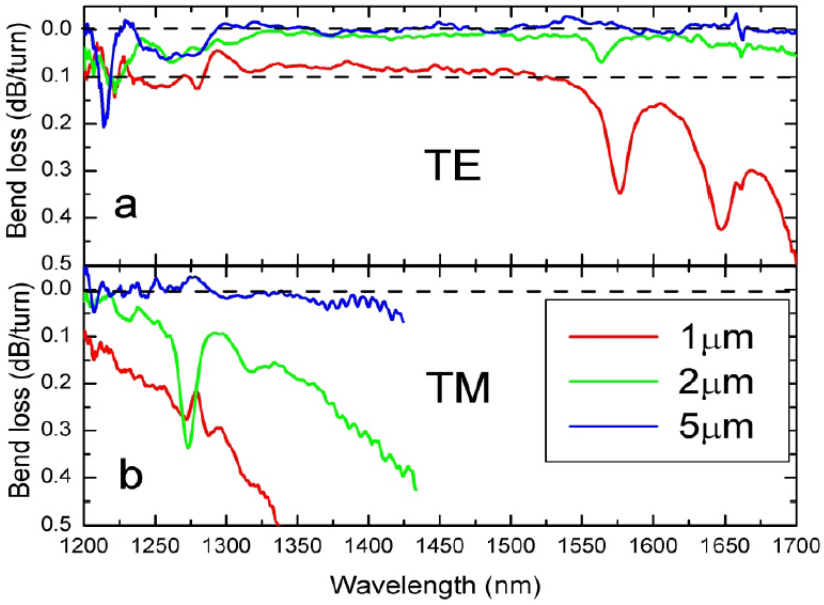

Figure 2.15: Spectra of bending losses for TE (a) and TM (b) polarizations for $(445 \times 220)\ nm$ SOI strip waveguide, from[62].

The Finite Element Method

Generally speaking, the equations governing physical phenomena usually contain time and space partial derivatives and are therefore said Partial Differential Equations (PDE). These equations cannot be solved analytically for the majority of the encountered problems and require approximate solutions. In numerical approximation schemes, the PDE are reformulated in an algebraic equations that are solved through numerical routines implemented in computer software.

The FEM numerical method uses a weak or variational formulation of the PDE that reduces the requirements on the smoothness of the solution, i.e. the required number of its derivatives which are continous [65]. Let's consider the one-dimension homogeneous Dirichlet problem for the unknown function $u(x)$:

$$\begin{cases} u''(x) = f(x) & 0 < x < 1 \\ u(0) = 0 \quad u(1) = 0 \end{cases}, \tag{2.53}$$

Multiplying both sides of the equation by a test function v and integrating over the domain Ω, one obtains:

$$\int u'v' = \int fv \tag{2.54}$$

with the assumption that v belong to the Sobolev space $H_0^1(\Omega)$, i.e. v and

their derivatives v' are square integrable on the domain aΩ and vanish at the boundary.

The weak formulation, or variational formulation, of Eq. (2.53) is obtained by requiring this equality to hold for all test functions in the Hilbert space. It is called "weak" because it relaxes the requirements of Eq. 2.53, where all the terms of the PDE must be well defined in all points. The relations in Eq. (2.54), instead, only requires an equality in an integral sense. For example, a discontinuity of a first derivative for the solution is perfectly allowed by the weak formulation since it does not hinder the integration.

The Dirichlet problem of Eq. (2.53), in the weak formulation, can be therefore expressed as:

$$\int u'v' = \int fv \quad \forall v \in H_0^1(\Omega) \tag{2.55}$$

It can be shown, see for example [65], that the field u is a solution of the problem of Eq. (2.55) solely if it minimizes the functional defined by:

$$J(v) = \frac{1}{2}\int (v')^2 - \int fv \tag{2.56}$$

This formulation is said variational and is equivalent to the weak formulation and leads to the same results.

Seeking an approximate solution for (57) in a finite-dimensional subspace of V, $V_h \subset V$, the solution can be expressed as a linear combination of the basis function φ_j of the space V_h:

$$u_h(x) = \sum_{i=1}^{N_h} u_j \varphi_j(x) \tag{2.57}$$

In the Galerkin method the same basis is used for the unknown functions u and test functions v. Inserting Eq. (2.57) in Eq. (2.55), the following matricial equations for the coefficients u_j, contained in the vector u, is given by:

$$Au = F \tag{2.58}$$

where A_{ij} are said stiffness matrix components and are given by:

$$A_{ij} = \int \varphi_i(x)\varphi_j(x) \tag{2.59}$$

and

$$F_i = \int f(x)\varphi_i(x) \tag{2.60}$$

Selecting carefully the basis function, it is possible to reduce the number of non null components of the stiffness matrix and simplify the calculations of the integrals. In particular, choosing function basis that are supported over a very small geometrical region, said finite elements, the integrals in Eq. (2.59) are zero everywhere, except in very limited regions where they overlap. The

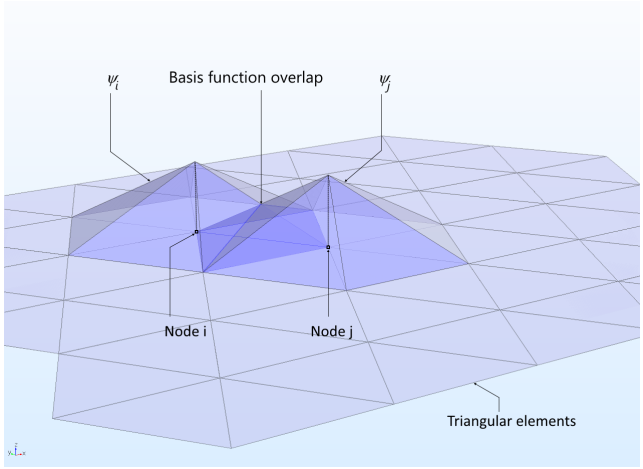

Figure 2.16: Tent-shaped linear basis functions that have a value of 1 at the corresponding node and zero on all other nodes. Two base functions that share an element have a basis function overlap, from [66].

employment of polynomial bases, such as Lagrangian polynomial, simplifies the calculation of these overlap integral.

The principles of the FEM presented for this simple 1D problem are valid for more complex analysis such as structural mechanics and electromagnetic analysis in 2D or 3D domain. In these cases the expressions of the stiffness matrix coefficients are different from those given by Eq. (2.58), Eq. (2.59) and Eq. (2.60), and the supports of the basis functions are selected to have polygonal area or volumes. Nevertheless, the weak formulation of the problem leads to matricial equations similar to the ones obtained for the 1D problem.

2.6.1 FEM formulation for mechanical analysis

For the estimations of the mechanical properties of the strained structures, the FEM numerical method has been used to solve the equilibrium equations for stress and strain tensors in linear elasticity regime. In particular, the equations governing the deformation tensor distribution $u(r)$ of a solid, caused by external forces and internal stress, are given by:

$$L^T \sigma + F = 0 \tag{2.61}$$

$$L = \begin{bmatrix} \frac{\partial}{\partial x} & 0 & 0 & \frac{\partial}{\partial y} & 0 & \frac{\partial}{\partial z} \\ 0 & \frac{\partial}{\partial y} & 0 & \frac{\partial}{\partial x} & \frac{\partial}{\partial z} & 0 \\ 0 & 0 & \frac{\partial}{\partial z} & \frac{\partial}{\partial y} & 0 & \frac{\partial}{\partial z} \end{bmatrix} \tag{2.62}$$

$$\sigma_{ij} = D_{ijkl} \varepsilon_{ij} \tag{2.63}$$

$$\varepsilon_{ij} = \frac{1}{2}(\frac{\partial u_i}{\partial x_j} + \frac{\partial u_j}{\partial x_i}) \tag{2.64}$$

where F is the external force, σ is the stress tensor and ε is the strain tensor. It can be shown that the deformation tensor which is solution of the problem, minimizes the potential energy potential functional given by:

$$\Phi(u) = \frac{1}{2}\int dV \varepsilon^T D\varepsilon - (\int dV F^T u + \int dS f^T u) \tag{2.65}$$

Seeking solutions in the form of linear combination of basis function

$$u = \sum a_i N_i(x) \tag{2.66}$$

with coefficients a_i, Eq. 2.65 can be rewritten as:

$$\Phi(a) = \frac{1}{2}a^T(\int dV Q^T DQ)a - a^T(\int dV N^T F + \int dS N^T f) \tag{2.67}$$

where a is the vector of the coefficients a_i and $Q = LN$.
The minimization of the functional brings to the following matricial equation

$$Ka = P \tag{2.68}$$

where the stiffness matrix are given by:$K = \int dV Q^T DQ$ and the equivalent force vector P is given by$P = \int dV N^T F + \int dS N^T f$. The solution of Eq. (2.68) provides the coefficients a_i that can be used to express the deformation field, the strain field and the stress field, through Eq. (2.66).

2.6.2 FEM formulation for electromagnetic analysis

The FEM-based simulative model has been also employed for the estimation of the electric and magnetic field distribution and propagation constant for the mode radiation propagating along the strained SOI waveguide. The starting point is the Maxwell equations for harmonic electric and magnetic field in dielectric materials:

$$\nabla \times H(x,y,z) = i\omega\epsilon(x,y,z)E(x,y,z) \tag{2.69}$$

$$\nabla \times E(x,y,z) = -i\omega\mu H(x,y,z) \tag{2.70}$$

Substituting Eq. (2.69) in equation (2.70), one obtains

$$\nabla \times [\epsilon^{-1}\nabla \times H] - k_0^2 H = 0 \tag{2.71}$$

where $k_0^2 = (\omega/c)^2 \varepsilon_r \mu_r$.

The unknown function for the FEM analysis is the magnetic field and it can be shown that the solutions of equation is a stationary point of the operator L given by:

$$L = \nabla \times (\epsilon \nabla \times H) - k_0^2 \tag{2.72}$$

Eq. (2.72) can therefore be rewritten as

$$L'(H) = 0 \tag{2.73}$$

Seeking a solution in the form of a linear combination of a basis function of V_h, $u_h(x) = \sum u_j \varphi_j(x)$, and imposing that a solution is a stationary point of the operator L, one obtains the following eigenvalue matricial equations for the coefficients u_j:

$$(\sum_{j=1}^{N_k} < L\varphi_j, \varphi_j > -\lambda \delta_{ij}) \cdot u_j = 0 \tag{2.74}$$

Eq. (2.74) represents a formulation of the Maxwell equations for a general geometry. As described in the previous section, cylindrically symmetric waveguide structures admits solutions in the form:

$$H(x, y, z) = H(x, y) e^{-i\beta z} \tag{2.75}$$

where β is the propagation constant of the mode and $H(x, y)$ is the transverse mode distribution. The dimensions of the problem can be therefore reduced and Eq. (2.74) can be solved in the domain given by the cross-section of the waveguide given the boundary conditions at the interfaces between the different material. The refractive index can be extracted by the attained value of β through the relation:

$$\beta = n_{eff} \cdot k_o \tag{2.76}$$

and the magnetic field H and the electric field E can be reconstructed as the linear combination of the polynomial functions chosen as basis with the obtained coefficients u_j.

2.7 Microring resonators

A part of the research activity reported in this Dissertation thesis has been focused on SiPh integrated orbital angular momentum (OAM) emitters. Such innovative devices are based on microring geometry and exploit the wavelength-dependent electromagnetic properties of the optical resonators. In this section I will describe the fundamental working equations required to understand the behavior of a microring resonator and will provide the theoretical basis for the experimental analysis, carried out on the OAM emitter devices, which is reported in Chapter 6.

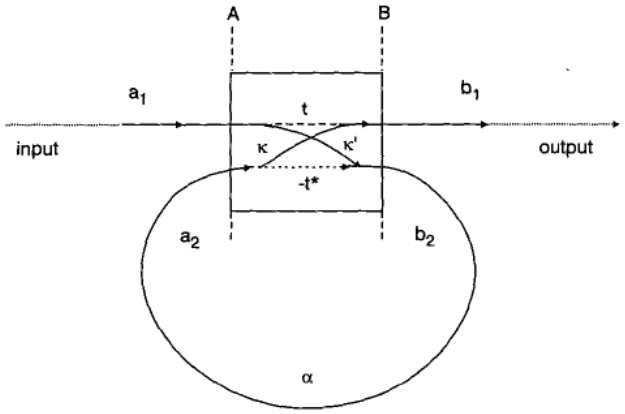

Figure 2.17: Schematic representation of dielectric waveguide coupled to ring resonator, from[69].

Optical Resonators (OR) are devices that exhibit resonance behaviors, that is the amplitude of the response is more intense for solicitations at some frequency called, resonance frequency, than the others. The OR represent a fundamental building block for each optical system that require any kind of spectral selectivity: its application sweep from frequency filtering, packet switching and modulation[67, 68]. In silicon photonics (SiPh), the OR are usually implemented in the form of microrings: the development of SiPh technology enables the manufacturing of microring resonators with radius values of few micrometers. The basic layout employed for a silicon microring consists of a looped SOI waveguide distanced from a straight waveguide by a submicrometric gap[69], (Fig. 2.17).

When the gap is sufficiently small, evanescent coupling can occur and a certain amount of radiation can be transferred between the straight waveguide and the ring. The exchange of optical power between the resonant structure and the waveguide at steady state condition is governed by the constructive and distructive infererence between the circulating radiation and the injected power.

Under the conditions that just a single mode of the resonator and waveguide is excited, the response of the microring can be described trough a matricial relation between the complex mode amplitudes a_i and b_i:

$$\begin{vmatrix} b_1 \\ b_2 \end{vmatrix} = \begin{bmatrix} t & k \\ -k^* & t* \end{bmatrix} \begin{vmatrix} a_1 \\ a_2 \end{vmatrix} \tag{2.77}$$

were r is the self-coupling coefficient and k the cross coupling coefficients. If no power is lost in the coupling section, the matrix is unitary:$|k|^2 + |t|^2 = 1$.

The radiation after a round trip undergoes a phase shift and looses a certain amount of power due to propagation loss, bending loss and other effects:

$$a_2 = b_2 e^{i\phi} e^{i\alpha} \tag{2.78}$$

where $\phi = (2\Pi/\lambda)nL$ is the round trip phase shift, α is the propagation loss and L is the round trip length.

Solving Eq. (2.77) and Eq. (2.78) , one obtains the transmission spectrum T_n given by:

$$T_n = \frac{|b_1|^2}{|a_1|^2} = \frac{a^2 - 2ra\,cos(\phi) + r^2}{1 - 2ra\,cos(\phi) + (ra)^2} \tag{2.79}$$

The ring is said to be on resonance when the phaseϕ is a multiple of 2π, or when the wavelength of the light fits a whole number of times inside the optical length of the ring. In this case the transmission reduces to:

$$T_n = \frac{a^2 - r^2}{1 - (ra)^2} \tag{2.80}$$

When the internal losses a equal the coupling power r the transmitted power vanishes, i.e. the transmission resonance drops to zero. This condition, known as critical coupling is the effect of complete destructive interference in the outgoing waveguide between the transmitted radiation and the internal field coupled out[70]. Under critical coupling, the microring acts as an optical power "collector": a significant part of the injected power is stored as circulating radiation. Due to the increase of the optical intensity inside the ring with regard to the single-pass waveguide, intensity-dependent effects as well as nonlinear effects are enhanced. In the vortex beam emitters described in the Chapter 6, this condition is required to enhance the interaction of the field with the sidewall grating and achieve a good radiation efficiency.

Fig. 2.18 shows a typical transmission spectrum of a microresonators with Lorentzian linseshape dips in correspondence of the resonance wavelength and an almost flat transmission out of the phase matching condition.

Useful parameters characterizing the wavelength dependent response of the microring are the free-spectral range (FSR) and the full-width hal maximum (FWHM):

$$FSR = \frac{\lambda_{res}^2}{n_g L} \tag{2.81}$$

$$FWHM = \frac{(1 - ra)\lambda_{res}^2}{\Pi n_g L \sqrt{ra}} \tag{2.82}$$

where $n_g$is the group index given by $n_g = n_{eff} - \lambda \frac{dn_{eff}}{d\lambda}$.

2.8 Diffraction gratings

The vortex beam emitters are basically microrings with gratings patterned on the vertical sidewalls of the rings. In analogy with the described-above mechanism of scattering induced the vertical roughness at the vertical sidewall of a

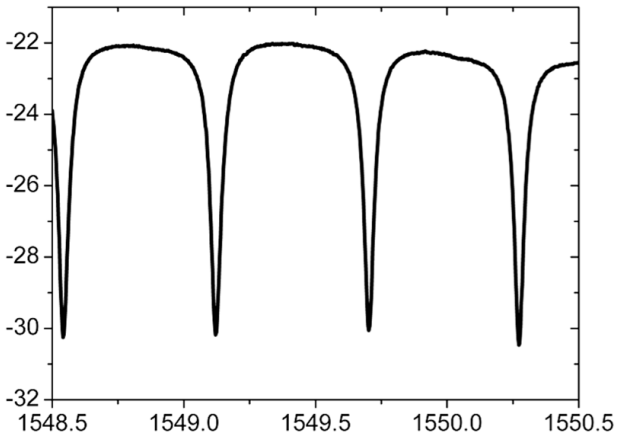

Figure 2.18: Typical transmission spectrum of a microring resonator, from [71].

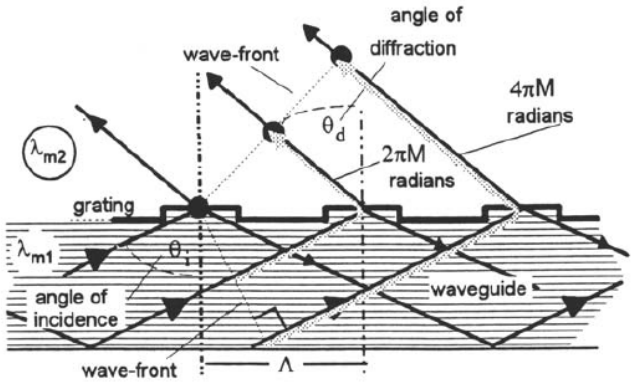

Figure 2.19: Schematic representation of a diffraction grating, from [72].

SOI waveguide, the sidewall grating leads to a transfer of power from the guided circulating mode and radiation modes. Nevertheless, in this case the distribution of the scattering elements is designed so that the scattered waves coherently interfere and giving rise to a well-defined phase pattern of the emitted beam. In this section a general analysis on the functioning mechanisms of a diffraction grating will be provided. A thorough analysis of the radiation efficiency of the grating and on the properties of the radiated beam will be provided in Chapter 6.

Let's consider a plane wave with a wavelength λ incident at an angle $\theta_i$on a periodic grating structure with which contain elements spaced at a period Λ, (Fig. 2.19).

Given θ_d the angle of diffraction, the phase shift ϕ between radiations scattered by two consecutive elements is $(2\Pi/\lambda)(sin(\theta_i) - sin(\theta_d))$. In order for the

Order of diffraction	M = 0	M = 1	M = 2	M = 3
First-order grating, p=1	Feed-forward	Feed-back		
Second-order grating, p=2	Feed-forward	Radiation at $\theta_d \sim 90°$	Feed-back	
Third-order grating, p=3	Feed-forward	Radiation at $\theta_d \sim \sin^{-1}(-1/3)$	Radiation at $\theta_d \sim \sin^{-1}(1/3)$	Feed-back

Figure 2.20: Feedback and radiation loss for a diffraction grating, from [72].

two beams to constructively interfere, the phase shift between the incident and scattered radiation need to be a multiple of the wavelength[72]:

$$\Lambda(sin(\theta_i) - sin(\theta_d)) = M\lambda \tag{2.83}$$

The integer valued M is called diffraction order and represents the phase shift, normalized to the wavelength, between the waves that are diffracted by adjacent elements. Considering the diffracted waves in the medium 2, it is necessary to take into account the different values of wavelength in the media and Eq. (2.83) becomes:

$$\frac{\Lambda(sin(\theta_i)}{\lambda_1} + \frac{\Lambda(sin(\theta_d)}{\lambda_2} = M \tag{2.84}$$

where λ_1 and λ_2 are the wavelengths in the semi-planes defined in Fig. 2.19.

Such considerations are general and can be applied for the analysis of any reflection or transmission gratings. Considering the case of a optical mode which propagates in the medium 1, as the case of a guided mode traveling in an optical waveguide. In this case the radiation travels in the parallel direction with regard to the interface, $\theta_i = 0$, and the diffraction angle θ_d in the medium 1 is:

$$sin(\theta_d) = (\frac{2M}{p} + 1) \tag{2.85}$$

where $p = 2\frac{\Lambda}{\lambda_2}$ is called grating order. In order for the radiation to be scattered forward or backward in the waveguide, the left-hand side of Eq. (2.85) needs to be -1 or $+1$. It's easy to show that feed-forward and feed-back scattering, corresponding to diffraction angles $\theta_d = -\Pi$ and $\theta_d = \Pi$, are always possible and occur for diffraction order 0 and p.

Considering the case of diffraction in medium 2, normal diffraction ($\theta_d = 1$) is obtained if the following condition is satisfied:

$$\frac{2M}{p} = 1 \tag{2.86}$$

Since the order of diffraction is integer valued, the condition described by Eq. (2.86) requires the grating order to be an even number. In the table reported in Fig. 2.20, such results are summarized assuming normal incidence, i.e. $\theta_i = 0$:

It's clear from this analysis that structures the exploit feedback in guided structures, such as distributed feedback (DFB) laser, employ grating with odd power in order to avoid radiation out of the waveguide. At the same time devices that requires an efficient radiation, as the beam vortex emitters, are expected to embed diffraction gratings with even diffraction order.

Chapter 3

Micrometric and nanometric silicon and SOI devices manufacturing

In order to carry out the experimental study on strained silicon technology that is reported in this work, various types of silicon structures and devices have been realized. Firstly, micrometric strained silicon straight ridges have been manufactured on silicon wafer and utilized in the lattice deformation measurements accomplished through the Convergent Beam Electron Diffraction (CBED) technique. This technique is carried out at Transmission Electron Microscope (TEM) facility and will be described in Chapter 4. The experimental results have been compared with the simulative analysis obtained through the Finite Element Method (FEM) based model described in Chapter 2.

Subsequently silicon ridge-based structures with nanometric dimensions have been fabricated on silicon wafers, through the Spacer Patterning Method (SPM) technique. These structures are shaped as microrings resonators, Mach-Zehnder interferometers and other optical devices. The rib geometry and the dimensions are the ones commonly employed for single mode Silicon-On-Insulator (SOI) waveguides-based devices. CBED strain measurements have been carried out on the nanofabricated structures in order to validate the FEM-based simulative model for structures similar to SOI single mode waveguides and to estimate the variation in the strain distribution induced by the shrink of the ridges dimensions.

Finally, the same nanometric structures have been manufactured, through SPM method, on SOI wafer realizing real SOI devices with single mode stripe waveguide geometry. The SOI devices have been optically characterized in terms of guiding properties and propagation loss. The results of all the experimental and simulative analysis carried out on the microfabricated and nanofabricated devices are reported in Chapter 5.

As described in Chapter 1, the attractiveness of Silicon Photonics (SiPh)

lies in the possibility to cheaply manufacture optical devices using standard semiconductor fabrication techniques and integrate them with the electronic devices. In particular the SiPh leverages the mature and low-cost Complementary Metal-Oxide Semiconductor (CMOS) nanofabrication technique that represents the state of the art for the manufacturing of microprocessors, micro controllers, RAM and other semiconductor based digital logic circuits. Since the framework of this study on strained silicon technology is the silicon photonics, only CMOS compatible fabrication steps have been employed. In particular the used photolitographic and etching processes and deposition techniques are commonly utilized in CMOS front-end-of-line and the materials employed, such as the stoichiometric silicon nitride covering the manufactured silicon structures, are compatible with the electronic devices.

In this Chapter the technological processes employed for the manufacturing of the strained silicon devices are described. In the first section, the process flow for the microfabrication of the straight silicon ridges is detailed and the operating principles of the main fabrication steps, such as the photolithography and dry etching, are analyzed. In the second section the fabrication processes employed for the realization of the nanometric structures on silicon substrate and SOI platform are detailed and the spacer technique, utilized for the manufacturing of the submicrometric feature and gaps, is analyzed. Some images of the devices are reported in correspondence of different fabrication steps: these images have been taken at optical microscope, TEM and Scanning Electron Microscope (SEM) facilities. The results of SEM and TEM analyses have been presented in works: [86, 87, 88, 89, 90, 91, 92]. In the Chapter 4 further results of TEM and SEM analyses are reported together with a thorough analysis of the obtained manufacturing quality.

3.1 Manufacturing of silicon micrometric ridges

In this section of the Chapter, the CMOS compatible processes employed for the manufacturing of the micrometric strained silicon ridges are described. The layout featured micrometric straight silicon ridges on silicon substrates covered by a 350 nm thick stoichiometric silicon nitride layer. The width values of the ridges and of the trenches that separate the structures range from 2 um to 10 um and from 3 um to 8 um respectively.

Firstly a 500 nm thick silicon dioxide film is deposited on the silicon substrate wafer. This deposition has been carried out at low temperature (420 $^{\circ}C$) in a low pressure chemical vapor deposition (LPCVD) reactor and utilizes a reaction of silane SiH_4 and molecular oxygen to form a SiO_2 layer.

Subsequently photolitographic processes have been employed to define the geometries of the analyzed structure in the low temperature silicon dioxide layer. These processes consist of several steps and allow to transfer a geometry from a mask, a plate containing clear and opaque features defining the pattern to be created, to a substrate layer.

In particular the photolitographic process carried out for the devices under

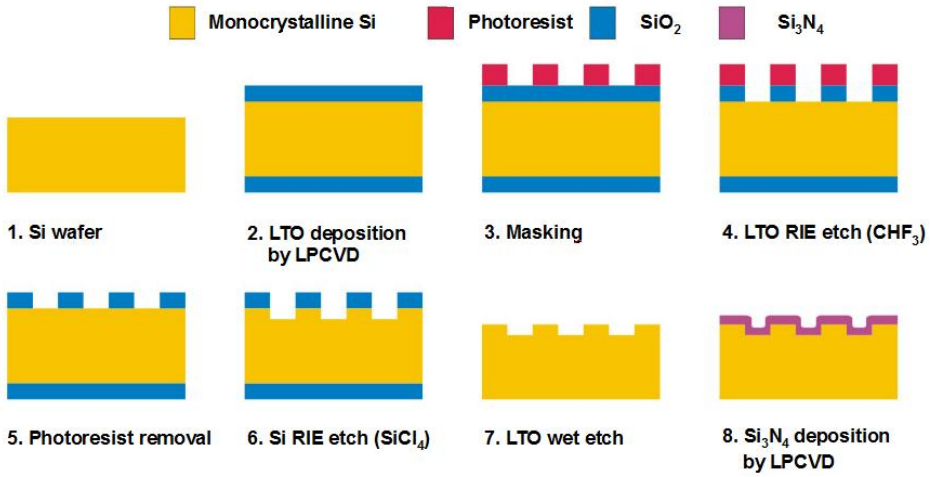

Figure 3.1: Process flow for the fabrication of the micrometric strained silicon ridges.

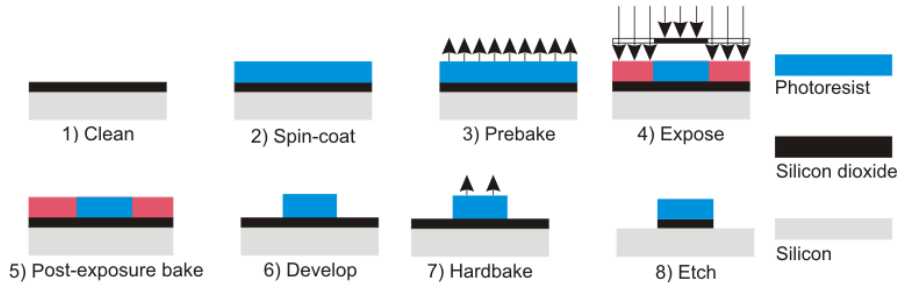

Figure 3.2: Schematic of the main photolithographic processes employed for the transfer of a geometry from a mask to a layer.

analysis requires:

- deposition of the photoresist
- thermal treatment: soft bake
- exposition
- development
- thermal treatment: hard bake.

Firstly, the surface wafer containing the deposited silicon dioxide layer is coated with a pre-resist layer of Hexamethyldisilazane (HMDS) said primer. This layer, deposited in form of vapor, makes the wafer surface hydrophobic increasing the adhesion of the photoresist.

Then the photoresist (PR) is deposited as a thin film on the substrate. The PR responds to exposing ultra violet (UVA) radiation in such a way that the mask image can be replicated and protects the underlying layer to the subsequent processes. It's made up of a organic photosensible resin, a catalyst enhancing the PR sensitivity to the UVA radiation and an organic solvent that controls the PR viscosity keeping it the the liquid state. The PR employed for these process is HPR-504 produced by Fujifilm. In order to obtain a uniform and controlled PR deposition, a spin coating technique has been utilized: $4\ ml$ of PR has been dispensed on the wafer that is spun at $5000\ rpm$ for 30 seconds through rotational stages. Given the viscosity of PR, with the spin velocity and time employed the thickness of the PR is around $1080\ nm$.

After the PR has been coated, the wafer is undergone to a soft bake at $110\ ^{\circ}C$ for 60 seconds. This temperature step drives off solvent from the span resist, improves the adhesion of the resist the substrate and anneals the eventual shear forces the PR and wafers induced by the rotation that could damage the sample.

In the next step the resist is exposed to UV radiation through a mask made up of sodalime, a UVA transparent material with the geometries to be transferred in crome Cr, opaque to radiation. In the contact printing photolitographic method, employed in the reported process, the mask is clamped to the spin-coated wafer with sub micrometric precision alignment through a mask aligner and exposed through UV light. The resolution, defined as the minimum feature size of the mask geometries replicable on the wafer, is affected by the wavelength of the radiation employed in the exposition and the thickness of the PR. For the processes under analysis the minimum feature size is approximately $1250\ nm$.

The wafer is therefore immersed in a solvent solution, said developer, that removes the area of the PR exposed to the radiation. The HPR-504 employed is indeed a positive PR, i.e. contains a stabilizer that slows down the dissolution rate of the resist in a developer and that breaks down when exposed to light, leading to the preferential removal of the exposed regions.

Finally the wafer is undergone a thermal process, hard bake, at $105\ ^{\circ}C$ that removes residual solvent and humidity traces, improves the adhesion and increase the PR resistance to the following etching processes.

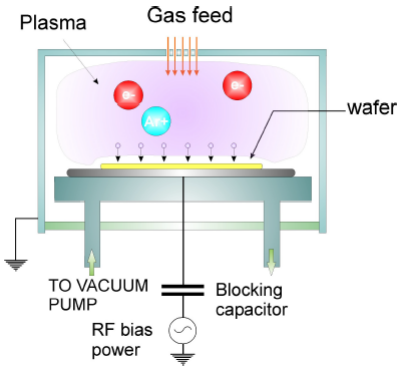

Figure 3.3: Schematic of a RIE setup.

The resist pattern is then transferred to the underlying low-temperature oxide (LTO) through dry etching (RIE). This process is carried out in a high-void chamber said Reactive Ion Etcher: applying an high frequency tension (in this case 13.56 MHz) between the electrodes to a mixture of gas, a plasma is obtained: a partially ionized gas composed by ions, electrons and neutral species [73].

With regard to the type of dry etching employed, the generation of plasma accomplishes different purposes: if the etching action is purely chemical the plasma plays no role than to produce the reactant species. In this case the produced energetic species react chemically with the exposed region of the material to be etched. This kind of etching is usually isotropic, i.e no preference in direction is observed and the removal of substrate material proceeds laterally under the resist as well as vertically toward the silicon surface with the result that the etched features are generally larger than the dimensions of the resist patterns. On the other hand chemical dry etching offers high selectivity in the species to be etched. In the physical dry etching the removal is carried out through sputtering: the ions produced in the plasma are directed by the potential toward the substrate and hit the surface vertically: the etching in this case is highly directional but no selection in the removed material is realized. By proper choices of the chemical species of the gas employed and pressure and potential values, a trade-off between the pure physical and pure chemical etching can be obtained with suitable selectivity and anisotropy.

In the microfabrication of the analyzed devices, plasma containing CHF_3 is employed: the fluorine atoms produced by the collision between electrons and gas molecules break the covalent bonding of silicon dioxide. The oxygen in vapor leaves the substrate and the remaining silicon atom bonds to fluorine ion or radial present in plasma and the resulting product SiF_4 is volatile.

Subsequently the photoresist present after the dry etch is removed from the wafer through plasma ashing: reactive atom oxigen present in the plasma

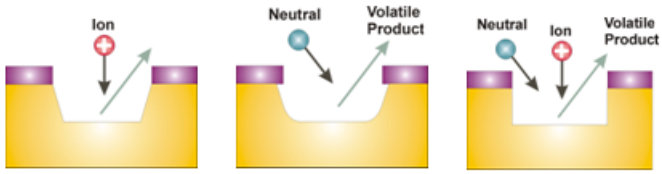

Figure 3.4: Etching profiles generated with physical RIE (left), chemical RIE (center) and ion-assisted RIE (right).

produced employing microwave combines with the photoresist to form ash that is removed by vacuum pump.

At the next step, the geometries defined in the silicon dioxide layer are transferred on the silicon layer with the SiO_2 ridges acting as protective masks. As for the SiO_2 case, energetic ion-assisted etching is accomplished: the plasma employed for the silicon dry etching contained $SiCl_4$. Chlorine chemistry, due to simultaneous physical and chemical contributes to the silicon etching assures an high anisotropic, i.e vertical, patterning and a good etching depth control. Furthermore the chlorine chemistry exhibits a good selectivity on SiO_2: this implies that no significant variation in the geometry of the SiO_2 mask during the etching process expected. It's worth pointing out that a chlorine chemistry could not be employed on silicon with PR masks due to its aggressiveness with organic compounds.

After the LTO mask is removed through a solution a 7% HF solution said buffered oxide etch (BOE), superficial organic and metallic contaminants are removed through an accurate sequence of aqueous acid and basic solutions (RCA cleaning procedures) [74].

Fig. 3.5 and Fig. 3.6 show optical images of one set of micrometric silicon ridges after the removal of the silicon dioxide mask. The shown structures are expected to be 2 μm wide and distanced by 3 μm wide trenches.

Finally a thin layer of stoichiometric silicon nitride film is deposited on the silicon structures through low pressure chemical vapor deposition. The LPCVD silicon nitride is obtained by reacting dichloro silane $SiClH_2$ and ammonia NH_3 at 780 $^{\circ}C$.

In Fig. 3.7 is reported a STEM image of a microfabricated silicon ridge after the deposition of the silicon nitride layer. The white color corresponds to the silicon nitride layer, the gray color to silicon and the black to the epoxy resin utilized in the sample preparation.

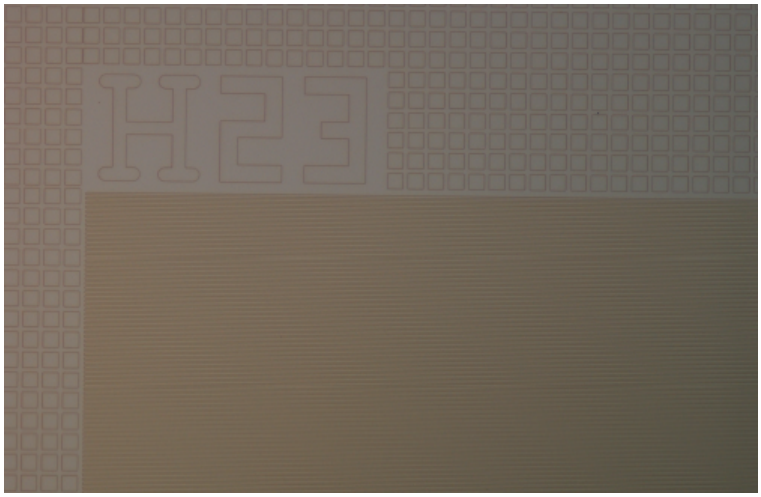

Figure 3.5: Optical image of a set of micrometric silicon ridges after the removal of the silicon dioxide mask.

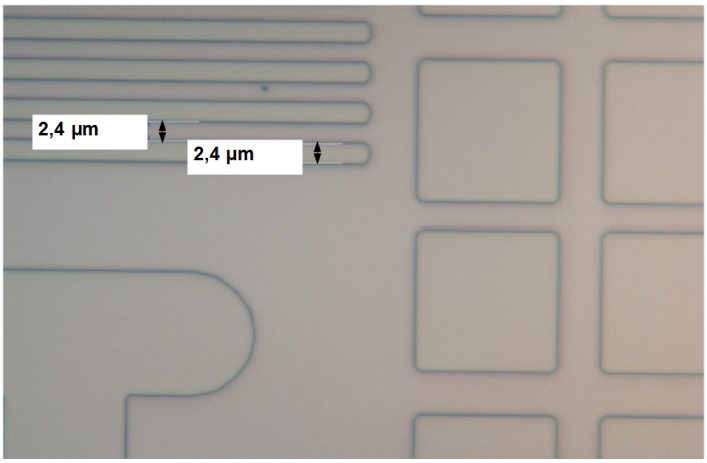

Figure 3.6: Particular of a set of micrometric silicon ridges after the removal of the silicon dioxide mask.

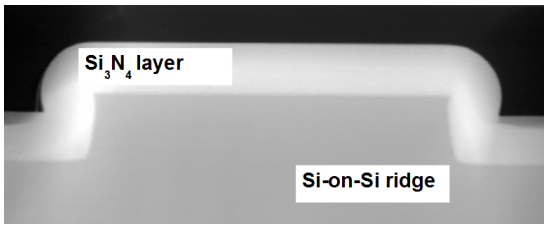

Figure 3.7: STEM image of a microfabricated silicon ridge after the deposition of the silicon nitride layer.

3.2 CMOS nanofabrication processes through the spacer technique

In the second part of the study, various nanometric silicon structures have been fabricated on silicon substrates and silicon-on-insulator (SOI) substrates . These devices, based on (450×220) nm silicon nanowires geometry, have been shaped as microring resonators, Mach-Zender interferometers and directional couplers in order to study the strain distribution on structures with the geometry typically employed for SOI devices. The process flow for the fabrication of the micrometric rib structures, described in the previous section, is not suitable for the manufacturing of these structures since the dimensions of the silicon wires and of the gaps and voids present in the layout, are far smaller than the resolution of the lithographic technique employed. This limit has been overcome through the employment of a multiple patterning technique that required the addition of several intermediate steps with regard to the processes described in the previous section. A detailed description of the multiple patterning technique utilized and of the manufacturing steps employed for the nanofabrication is reported in the next sections.

3.2.1 Spacer patterning method

The patterning of the nanometric silicon structures has been accomplished through the spacer patterning method (SPM): this technique is commonly employed in microeletronics manufacturing processes that require an enhancement of the feature density imposed by the lithographic processes. The SPM technique has been adopted, for example, for sub-20 nm logic nodes, such as 14 nm and 10 nm [75]. In particular the SPM enables the realization of geometries with structures or gaps smaller than the minimum feature size that can be transferred by the photolithographic processes employed through the exploitation of the high anisotropy of dry etching processes. Recently the SPM nanofabrication technique has been employed for the fabrication of Micro Electro-Mechanical Systems (MEMS) devices in SOI technology [76].

In Fig. 3.8 is reported a sketch describing the most important steps of the SPM process flow:

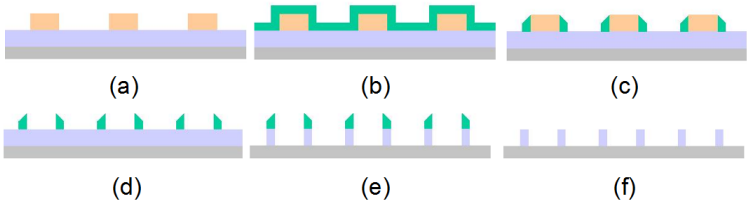

Figure 3.8: Process flow employed for the Spacer Patterning Method nanofabrication technique.

Firstly, the initial pattern (a) contains structures and gaps with the dimension imposed by the photolithographic processes. A conformal layer is deposited on the initial pattern (a) and etched back: due to the anisotropy of the dry etching processes the spacer portion covering the initial structure is removed while the portion on the sidewall remains (c). Once the first pattern is removed only the spacer features remain (d) and act as a mask for the etching of the underneath layer (e). The width of the SPM outcome features (e) is then controlled by the spacer deposition parameters and the gap value obtained is given by the difference of initial mandrel gaps and the features width. This technique can be cascaded in order to obtain narrower widths, as for the case of the manufacturing flow of the devices under analysis: in this case the technique is said multiple SPM. It's clear from this description that the conformal deposition of the spacer layer and the anisotropy of the dry etching process play fundamental roles in the SPM.

3.2.2 Manufacturing of nanowires-based structures

As described above, the nanofabrication of the the structures and devices under analysis required the use of the SPM. The photolitographic system use deep ultraviolet (DUV) ligth ($\lambda = 250\ nm$) and allows a minimum feature size down to about 700 nm and is not suitable for the dimensions of the structures and the gaps to pattern: in particular single mode SOI waveguide are 450 nm wide and the distance between the waveguides in the coupling section of the devices are shorter than 300 nm. The SPM enables the realization of the designed geometries avoiding the employment of other technologies which are commonly employed for the fabrication of silicon photonic devices, such as Electron Beam Lithography (EBL) [77].

In the Fig. 3.9 is reported the process flow for the realization of the nanometric structures and devices. In particular the technological processes have been carried out starting from a 4" silicon wafers for the manufacturing of the structures used for the Convergent Beam Electron Diffraction measurements whereas the SiPh devices have been nanofrabricated starting from a 4" SOI wafer.

Firstly a 300 nm thick film of stoichiometric silicon nitride Si_3N_4 is deposited through LPCVD at 780 $^{\circ}C(2)$ on the silicon substrate followed by a 1 um thick

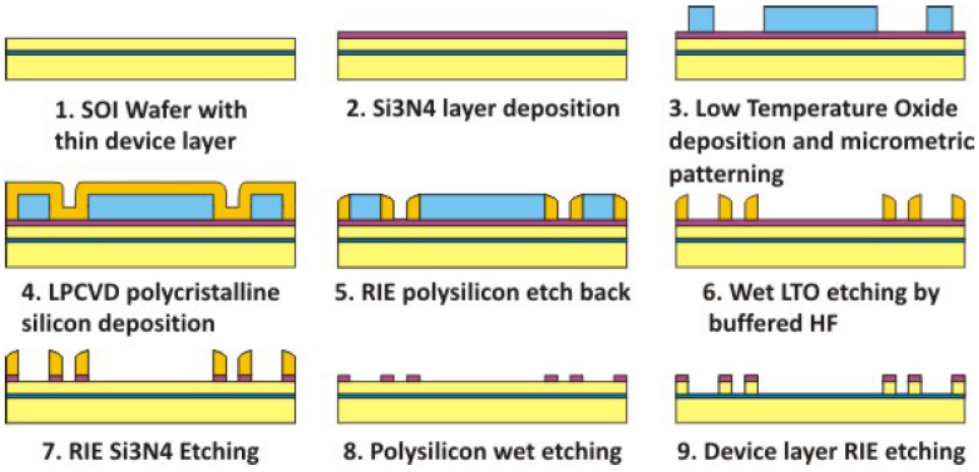

Figure 3.9: Process flow for the fabrication of the micrometric strained silicon ridges for the Si-on-Si optical test structures and SOI devices.

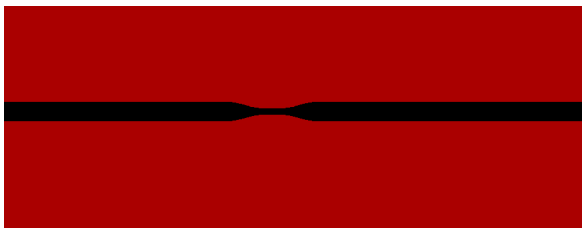

Figure 3.10: Layout mask of a directional coupler.

SiO_2 film. As for the case of the micrometric structures, the LTO deposition has been carried out in a low pressure chemical vapor deposition (LPCVD) reactor utilizing a reaction of silane SiH_4 and molecular oxygen. Subsequently the mask geometry is transferred on the SiO_2 layer through DUV photolithographic process. Some structures contained in the mask pattern are reported in Figg. 3.10, 3.11 and 3.12.

The red part corresponds to the chrome pattern: due to employment of a positive PR this part will not be removed by the developer and will act as a mask for the etching processes. It's worth noting that due to the employment of the SPM technique, the layout patterned on the mask do not duplicate the devices geometry as shown in Fig. 3.13.

The width of the nanowires are not defined and only the outer edge with regard to the gap is patterned in the LTO, (light blue). The gap has to contain the waveguide spacer of polysilicon (yellow), and is enlarged in comparison to the real one: the real one is of $300\,nm$ while the one patterned in the mask is

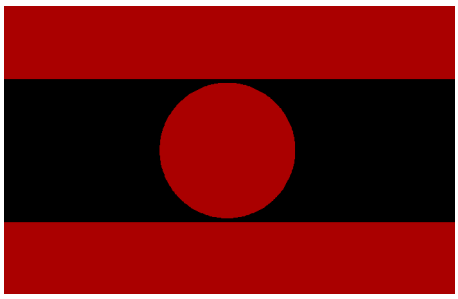

Figure 3.11: Layout mask of a microring resonator.

Figure 3.12: Layout mask of a Mach-Zehnder interferometer.

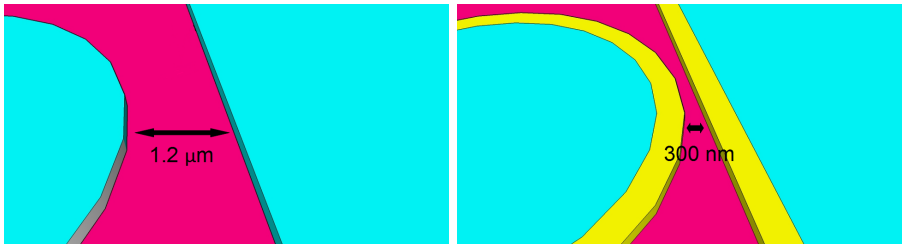

Figure 3.13: Schematic of the coupling sections of the nanofabricated structures. The yellow, purple and light blue colors represent polycristal silicon, silicon nitride and silicon, respectively.

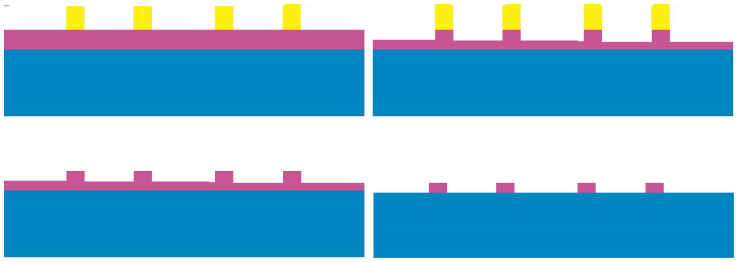

Figure 3.14: Technological steps for the definition of the Si_3N_4 nanometric structures. Yellow, purple and blue colors represent polycrystalline silicon, silicon nitride and silicon, respectively.

1.2 um since, to the width the of the real one are added the width of 2 waveguides of the coupling section.

The positive DUV photoresist UV6 was spun at 2000 rpm obtaining a 800 nm thick layer. After a softbake treatment at 130 $^{\circ}C$ for 3 minutes, the photoresist is exposed to the mask and is undergone to a post exposure bake at 140 $^{\circ}C$ for 90 seconds. The exposed area of the photoresist is removed through the DUV developer AZ 726 MIF and the LTO is dry etched with a fluorine-based plasma.

After the removal of the PR by a oxygen plasma and the surface wet cleaning, a 480 nm thick polysilicon layer is deposited through LPCVD at 610 $^{\circ}C$ through pyrolysis of sylane (SiH_4) on the patterned LTO layer acting as spacer layer for the SPT patterning. The polysilicon film was etched back without additional mask by anisotropic chlorine-based plasma. As for the silicon, chlorine plasma is found to carry out a anisotropic etching of polysilicon and to exhibit excellent selectivity over SiO_2. As a next step the LTO hard mask are removed through BOE solution and the silicon nitride layer is partially etched by an anisotropic fluorine-based plasma with the polysilicon acting as hard mask. The polysilicon spacers are then wet etched using the aqueous solution $H_2O : HNO_3 : HF(20 : 50 : 1)$. In order to prevent the silicon device layer to be removed by the polysilicon wet etching, a thin layer of silicon nitride layer has been left during the Si_3N_4 etching. This protective layer is then removed through a second Si_3N_4 etch back while a thin Si_3N_4 layer is left in correspondence of the structures to pattern acting as an hard mask for silicon patterning (see Fig. 3.14).

In Figg. 3.15, 3.16 and 3.17 are reported optical images of the devices following the second Si_3N_4 etching. In particular the area of the sample containing the spacer masks for a directional coupler, a microring and a microring network are observed. The green pattern corresponds to the Si_3N_4 mask laid on the silicon substrate (lighter color). The layout appear sharply defined for the

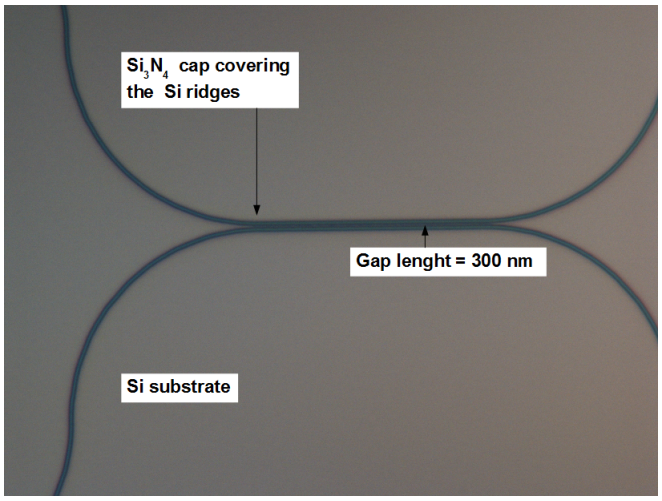

Figure 3.15: Optical image of a directional coupler manufactured on silicon wafer, after the RIE etching of silicon.

straight section and bent sections and no interruptions and discontinuity can be observed.

The silicon layer is finally patterned by a chlorine chemistry plasma etching with the Si_3N_4 acting as a hard mask. As described above, the chlorine chemistry assures a good etching depth control: the etching rate is about 50 nm/min. The time etching is set to obtain a height value of 220 nm for the realization of the silicon structures employed in the CBED measurements. As for the SOI devices, the silicon nanowires are patterned by a deep-etch through the silicon device layer using the silicon dioxide as an etch stop layer.

In Fig. 3.15 and 3.16, optical images of the samples containing a directional coupler and a microring resonator which have been manufactured on a silicon wafer, are reported at the step following the RIE etching of silicon. The silicon nitride cap (green) covers the silicon ridges laid on the silicon substrate (light color).

In Fig. 3.17 is reported an optical image of one directional coupler which has been manufactured on SOI platform. The silicon nitride (brown) was used as mask for the RIE "deep" etching that removed the unprotected silicon device layer exposing the buried oxide (BOX) (light brown).

Fig. 3.18 shows SEM images of a single silicon rib (top) and of two "coupled" silicon ribs (bottom) patterned on the silicon wafer. The images have been taken before the silicon nitride layer deposition. The silicon nitride cap that has been used as protective mask in the SPM method is visible on the top of the rib.

Fig.3.19 reports a SEM image of a manufactured SOI waveguide after the FIB ablation used to expose the device cross-section (this technique will be described in the Chapter 4). The nanowire on the BOX layer has been patterned

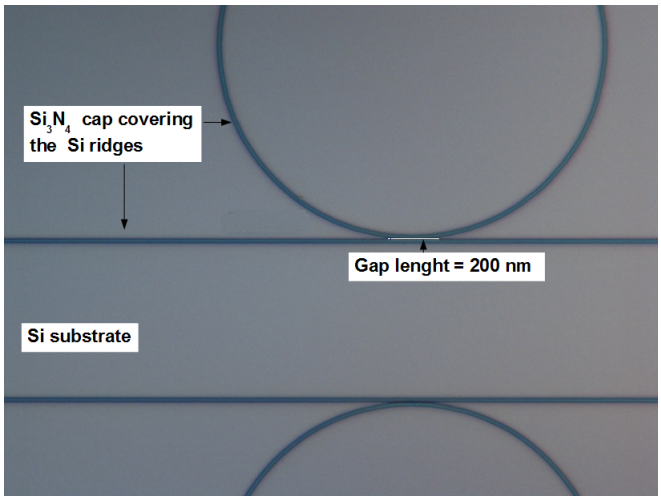

Figure 3.16: Optical image of a microring resonator manufactured on silicon wafer, after the RIE etching of silicon.

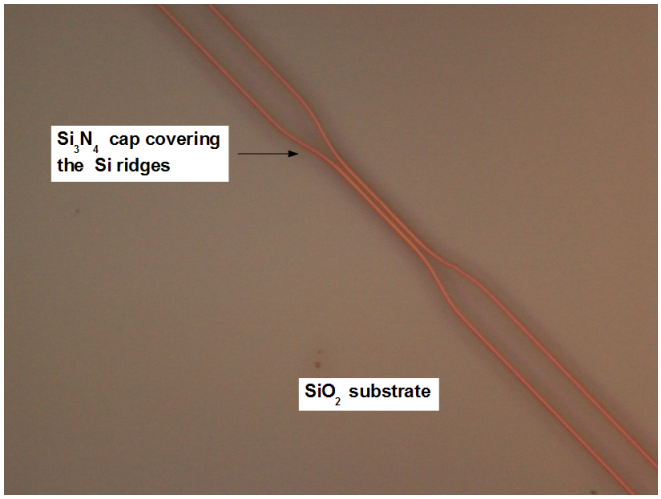

Figure 3.17: Optical image of one directional coupler manufactured on SOI platform after the RIE etching of silicon.

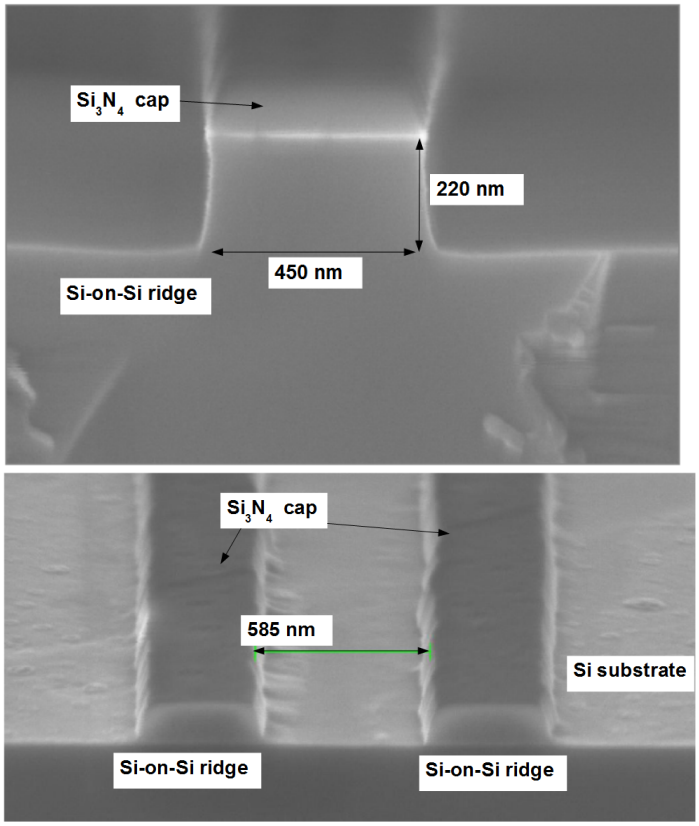

Figure 3.18: SEM images of a Si-on-Si single (up) and coupled (down) ridges before the Si_3N_4 deposition.

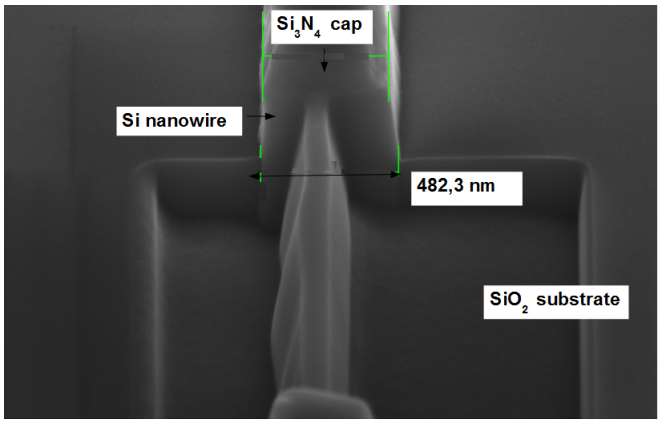

Figure 3.19: SEM image of a manufactured SOI waveguide before Si_3N_4 deposition.

in the silicon device layer and is covered by the silicon nitride cap.

Finally300 nm thick stoichiometric layer Si_3N_4 layer is deposited through LPCVD at 780 $^{\circ}C$.

Chapter 4

Electron microscopy analysis of the microfabricated and nanofabricated devices

4.1 Electron microscopy analysis

The microfabricated and nanofabricated strained silicon devices have been characterized through an extensive set of experimental measurements and analyses of their structural and mechanical properties. Firstly, we have evaluated the quality of the technological processes as well as the accuracy of the Spacer Patterning Method nanofabrication technique which we have employed for the manufacturing of the strained silicon and silicon on insulator (SOI) devices. Then, we have estimated, through the employment of the Convergent Beam Electron Diffraction (CBED) technique, the lattice deformation on the manufactured silicon micrometric and nanometric structures; the observed strain, as described in Chapter 2, is generated by the high intrinsic stress silicon nitride film which is deposited, through Low Pressure Chemical Vapor Deposition (LPCVD), on the structures. Such analyses have been performed through the employment of experimental measurements techniques carried out at Transmission Electron Microscopy (TEM) and Scanning Electron Microscopy (SEM) facilities. The aim of such analysis is to provide information on the possible use of the employed microfabrication processes and SPM technique for the manufacturing of silicon photonic devices and assess their compatibility with the strained silicon technology. Furthermore, the outcomes of the CBED measurements are expected to provide useful information for the validation of the FEM based simulative model, described in Chapter 2, which we have used in the analysis of the strain distributions of the manufactured devices, reported in Chapter 5. The results of the comparative analysis between the FEM-based simulative method and CBED measurements are reported in Chapter 5.

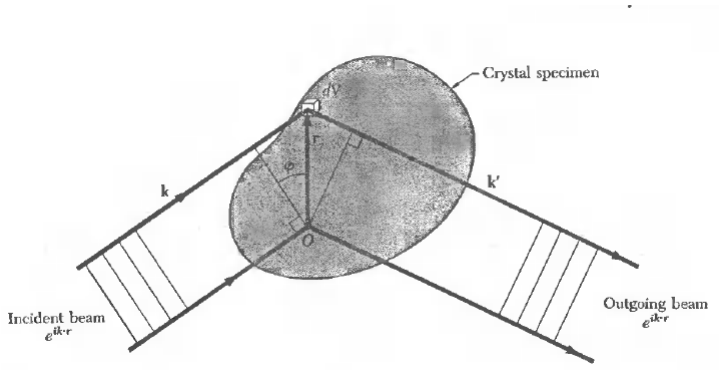

Figure 4.1: Schematic representation of the difference path length of the incident wave $\mathbf{k}$ at the point $\mathbf{O}$ and $\mathbf{r}$ for the diffracted wave $\mathbf{k}'$, from [78].

In this Chapter we describe the physical principles underlying the electron diffraction microscopy (section 1) and the operating principles of the transmission electron microscopy (TEM) for structural analyses (section 2). In section 3 we describe the CBED technique, which we have employed for the structural characterization, and the procedure used to obtain the components of the strain tensor starting from the analysis of CBED patterns. In section 4 and 5 we report some results of the STEM and SEM analyses which we have performed on the manufactured silicon structures and silicon on insulator (SOI) devices. Part of such results has been presented in the works: [86, 87, 88, 89, 90, 91, 92].

4.1.1 Electron diffraction

The crystal structure of matter can be studied through the analysis of the diffraction pattern which results from the interaction of an electron beam with the atoms constituting the material. The relation between the crystal structure and the diffraction pattern allows to extract useful information on the symmetries, lattice parameters and deformations of the sample.

The Coulomb interaction between the incident electrons and the charged particles of the material produces a scattering of the waves associated to the beam electrons. Considering an electron beam with a wavevector $\mathbf{k}$ directed toward a specimen, as depicted in Fig. 4.1., the phase difference between the electron waves scattered by the two elements of volume at wavevector $\mathbf{k}'$ is given by:

$$\exp(i(\mathbf{k}-\mathbf{k}')\cdot\mathbf{r}) \tag{4.1}$$

The amplitude of the electronic wave scattered by the infinitesimal volume is proportional to the charge concentration $n(\mathbf{r})$ with the same periodicity of the lattice. Under the assumption that the amplitude of the incident beam is

constant throughout the sample volume (Born approximation) and that absorption, refraction and multiple scattering can be neglected (kinematic diffraction regime), the contribute to the amplitude of the scattered electronic beam given by whole volume is:

$$F = \int dV n(\mathbf{r}) e^{(i(\triangle \mathbf{k})\cdot \mathbf{r})} \tag{4.2}$$

where $\triangle \mathbf{k}$ is said scattering vector and is given by

$$\triangle \mathbf{k} = \mathbf{k}' - \mathbf{k} \tag{4.3}$$

Expanding $n(\mathbf{r})$ in terms of the reciprocal vectors of the lattice$\mathbf{G}$ with coefficients $n_{\mathbf{G}}$

$$n(\mathbf{r}) = \sum_{\mathbf{G}} n_{\mathbf{G}} e^{-i\mathbf{G}\cdot\mathbf{r}} \tag{4.4}$$

Eq. (4.2) can be expressed as:

$$F = \sum_{\mathbf{G}} \int dV n_{\mathbf{G}} e^{(i(\mathbf{G}-\triangle \mathbf{k})\cdot \mathbf{r})} \tag{4.5}$$

. When the scattering vector equals one of the reciprocal lattice, i.e.

$$\triangle \mathbf{k} = \mathbf{G}, \tag{4.6}$$

the exponential vanishes and the amplitude is simply given by $F = V\, n_{\mathbf{G}}$. Considering the case of elastic scattering, the modulus of the incident beam and of the emergent beam are the same $|\mathbf{k}| = |\mathbf{k}'|$ so that:

$$2\mathbf{k}\cdot\mathbf{G} + \mathbf{G}^2 = 0 \tag{4.7}$$

The equation can be rewritten as:

$$2d\sin(\theta) = n\lambda \tag{4.8}$$

where d is the distance between the parallel lattice planes normal to the direction of $\mathbf{G}$, θ is the angle between the planes and the incident beam and λ is the wavelength of the electron beam. The condition expressed by Eq. (4.8) is said Bragg condition. Taking the scalar product of Eq. (4.6) with the primitive vectors of the lattice $\mathbf{a}_1$, $\mathbf{a}_2$ and $\mathbf{a}_3$, one obtains the so called Laue equations:

$$\mathbf{a}_1 \cdot \triangle \mathbf{k} = 2\Pi v_1 \tag{4.9}$$

$$\mathbf{a}_2 \cdot \triangle \mathbf{k} = 2\Pi v_2 \tag{4.10}$$

$$\mathbf{a}_3 \cdot \triangle \mathbf{k} = 2\Pi v_3 \tag{4.11}$$

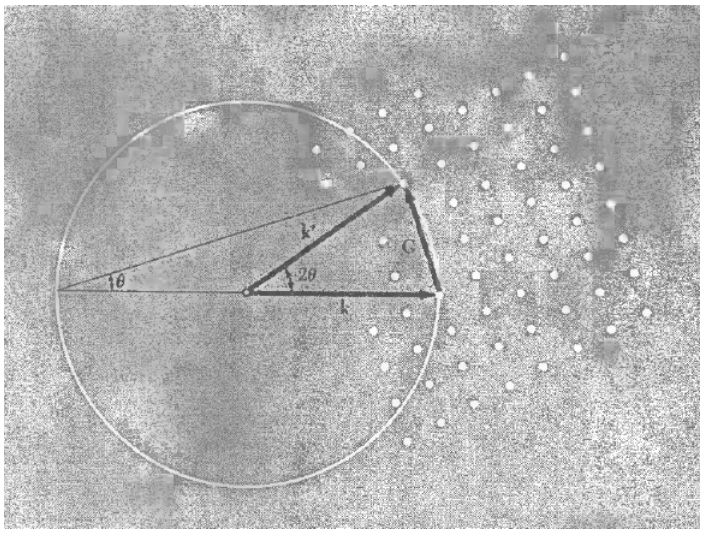

Figure 4.2: Representation of the Ewald sphere for the diffraction condition, from[78].

The Laue equations can be interpreted in a simple way: Eq. (4.9) tells us that$\triangle\mathbf{k}$ lies inside inside a certain cone about the direction$\mathbf{a}_1$, Eq. (4.10) that $\triangle\mathbf{k}$ lies inside inside a certain cone about the direction $\mathbf{a}_2$ and Eq. (4.11) that$\triangle\mathbf{k}$ lies inside inside a certain cone about the direction $\mathbf{a}_3$. Therefore, in order for the reflection to takes place, the scattering vector $\triangle\mathbf{k}$ lies at the common line of intersection of such 3 cones.

A geometrical construction, said Ewald sphere, helps to visualize the Laue condition: the vector $\mathbf{k}$ is drawn in the direction of the incident beam and terminates in the origin of the reciprocal space which are drawn as void points (see Fig. 4.2). If the sphere of radius $2\Pi/\lambda$,centered about the origin of $\mathbf{k}$ intersects a point of the reciprocal lattice, then constructive interference occurs in the direction $\mathbf{k}'$.

Because of the thin nature of the specimen, the reciprocal lattice points can be considered to have an elongated shape with an height inversely proportional to the sample thickness (Fig. 4.3).

The intersection of the Ewald sphere with points laying on different planes gives rises to the so called Laue Zones: the Zero Order Laue Zone (ZOLZ) corresponds to the reciprocal space vectors orthogonal to the incident beam while Higher Order Laue Zone (HOLZ) give rise to interference with vectors possessing non vanishing parallel components. The diffraction pattern, according to the electron beam characteristics and the imaging technique carried out, can contain points or lines belonging to ZOLZ and HOLZ and can be used to obtain information on the structural properties of the material.

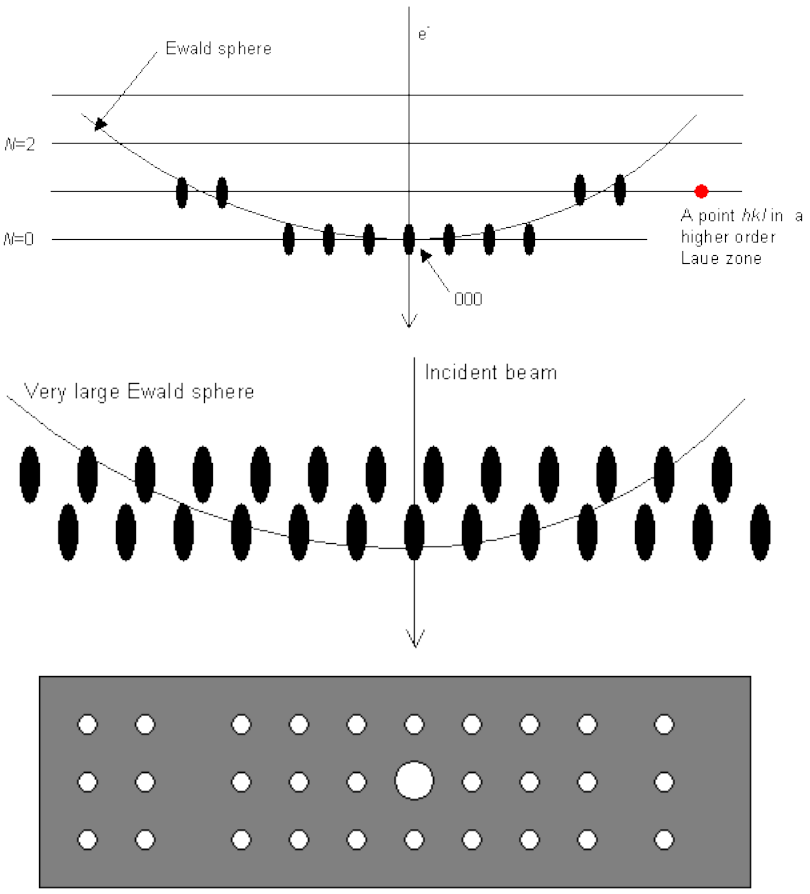

Figure 4.3: Schematic representation of the intersection of the Ewald sphere with the reciprocal lattice at Zero Order Laue Zone and Higher Order Laue Zone.

4.2 Transmission Electron Microscopy (TEM) analysis

4.2.1 Transmission electron microscope

A schematic of the TEM microscope employed for the CBED analysis is reported in Fig. 4.4. The electrons used for "illuminating" the sample are extracted from a source and accelerated along the optical axis toward the specimen in the electron gun. In a field emitter gun (FEG), as the Schottky FEG of the TEM facility which we have used for the STEM and CBED analysis, the electrons are extracted from a source made by coating a tungsten tip with a layer of zirconium oxide by applying a large electric potential between the tip and an anode. The beam generated by this type of FEG possesses a high degree of intensity collimation and coherency which are necessary for high resolution analysis. Particular electron lenses, said condenser lenses, representing TEM's equivalent of the glass lenses in a visible light microscope, collect the electron beam and modify its dimension, intensity and incidence angle in accordance to the type of the analysis to perform: for CBED and STEM analysis the beam in focused on an area of the sample with nanometric dimensions. The electron beam is directed on the sample holder which can be tilted in two orthogonal planes. The objective lens, placed below the sample, collects and focuses the transmitted electrons setting the magnification of the image and producing the diffraction pattern. The objective aperture limits the collection angle of the lens allowing certain beam of the diffraction image to pass through and exclude the others causing them to hit the metallic diaphragm. In particular for bright field (BF), the transmitted field is selected while for dark field (DF) imaging the diffracted beam is passed through the aperture. The focal plane of intermediate lens is conjugated to the image plane of the objective lens in the imaging modality or to the back focal plane in the diffraction modality. The projector lenses enlarges the images of the intermediate lens to form the final image on the phosphor screen or on other detection systems.

4.2.2 TEM sample preparation procedure

The sample is undergone to a procedure aimed at the achievement of the suitable thickness, dimensions and shape for the TEM/CBED analysis. First of all, the TEM specimens are required to be at most some hundreds of nanometers thick in order for the analyzing electron beam to penetrate it and the approximations described in section 1 to hold (Born approximation and kinematic diffraction). In particular, the thickness values of the sample which we have employed is about 200 nm. On the other hand, in order to avoid breaks and fragmentation during the movement and rotation of the specimen, it's required that the sample is mechanically sound and cohesive. Furthermore, the dimensions and the shape of the sample must perfectly fit with the holder's ones so that a good contact is assured and mechanical, electrical and thermal drifts are prevented.

Firstly the die containing the devices is glued with epoxy resin to various

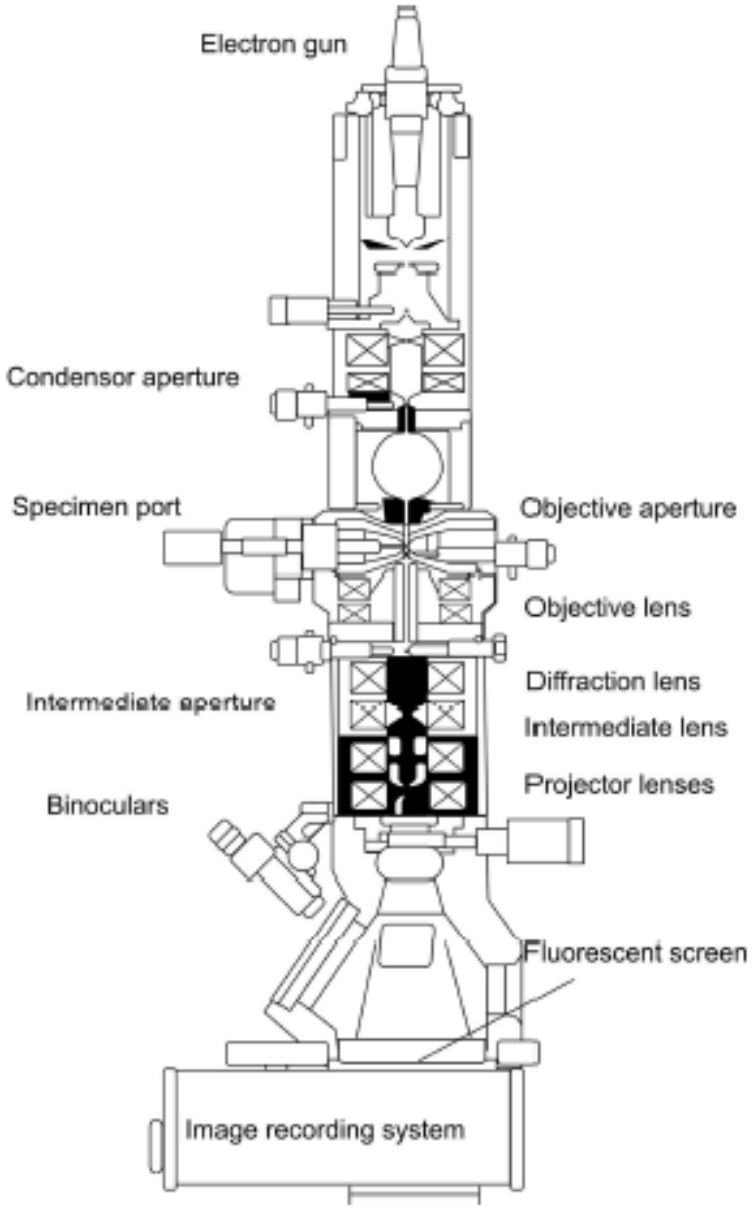

Figure 4.4: Schematic representation of a Transmission Electron Microscope.

silicon handles so that a 3 mm thickness is achieved. Then the sample is undergone to acetone ultrasonic cleaning bath in order to remove impurity and increase the adhesion of the glue. The specimen is then cut into 2 mm thick slices and a lapping process with abrasive materials with sequentially decreasing grit sizes (from 20 um to 10 um) is employed to slim the thickness down to approximately 20 um. Then a polishing process with abrasive liquids is employed to reduce the superficial inhomogeneity down to submicrometric level and 3 mm wide donuts shaped metallic disks are applied on the area of the cross-section to be analyzed. The thickness of the sample is further reduced through ion milling: ions of an inert gas, Ar, are accelerated from a wide beam ion source into the surface in order to remove material until a hole is produced in the center of the disk. Given the incidence of the ion beams, the thickness values of the sample grows, approximately, as a linear function from the hole to the 20 um thick border of the specimen. Finally the metallic disks are removed and through a low energy ion beam milling, the superficial damages and amorphous layer of redeposited material are carried away.

4.3 Convergent Beam Electron Diffraction (CBED) technique

4.3.1 CBED technique

The CBED technique is the oldest electron-diffraction technique used in TEM analysis: it was developed in the late '40 by Kossel and Mollenstedt well before LePoole developed the Selective Area Diffraction (SAD) that employs a parallel beam incident on the sample[79]. While much of the electron diffraction-theory was historically developed for SAD and standard imagine technique are based on such patterns, the CBED offers an improved spatial resolution with regard to its parallel-beam counterpart and CBED patterns contain much more crystallographic data though harder to extract. Since '70 the CBED technique is employed for structural characterization of crystals and analysis of lattice deformation for analysis which require a submicrometric resolution.

As mentioned, in CBED analyses the electron beam is focused in an area of nanometric dimensions: due to the increased range of the incident electron angles, instead of usual diffraction spots, diffraction disks are observed in CBED patterns (see Fig. 4.5 (A) and (D)). Under particular incidence conditions, the disks overlap and the diffraction intensity within a disk shows specific symmetry, which enables to determine the local crystalline structure of the sample, as shown in Fig. 4.5 (B),(C),(E) and (F).

If the beam convergence is sufficiently high, spots belonging to higher order Laue zones (HOLZ) will appear.

As described above, reciprocal lattice points in the HOLZ, unlike the ZOLZ ones, have non vanishing components along the axis parallel to the incident beam. This implies that the CBED diffraction patterns give fully three-dimensional information on the crystal lattice. If the Bragg condition is satisfied, a bright

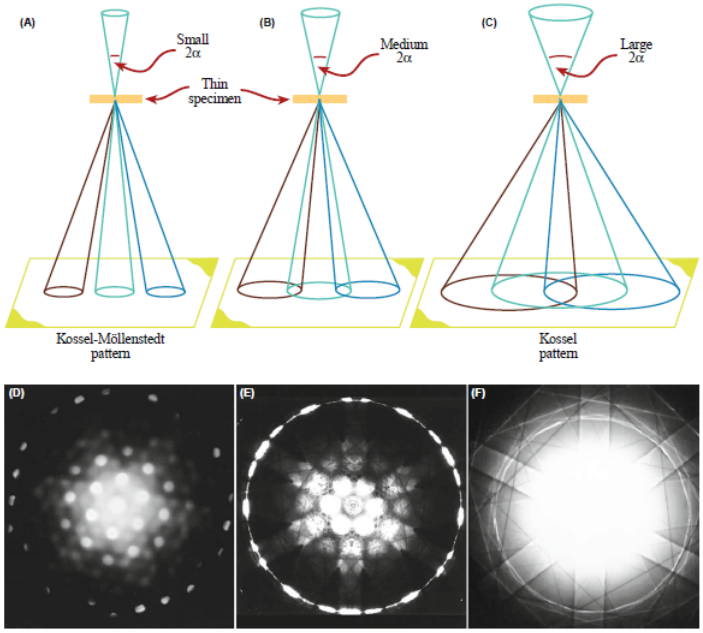

Figure 4.5: Ray diagrams, (A), (B) and (C), and CBED patterns (D), (E) and (F), for different convergent angle α, from [80].

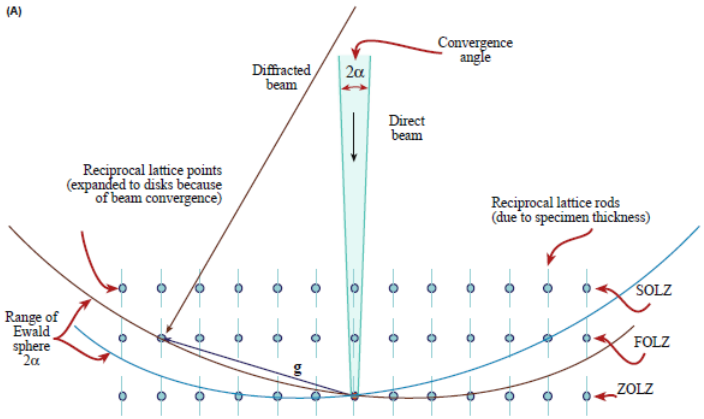

Figure 4.6: Ewald sphere, for a convergent electron beam, intercepting reciprocal-lattice points from planes not parallel to the beam, from [80].

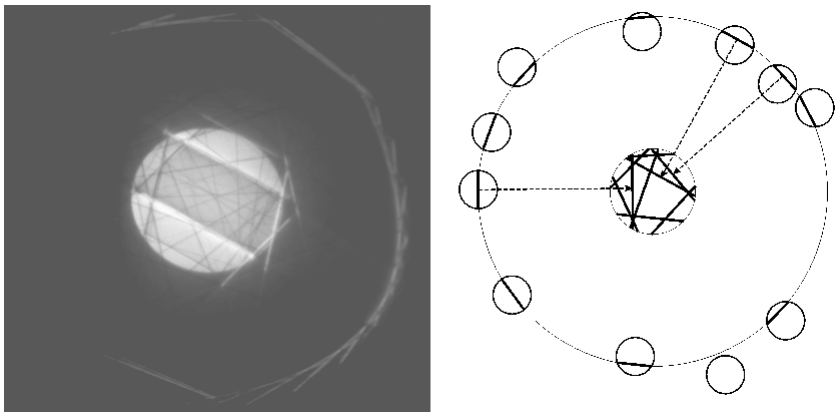

Figure 4.7: CBED pattern with a set of HOLZ lines inside the central disk (left). Sketch of the same pattern: 3 pairs of HOLZ lines are evidenced (right), from [81].

line will be observed inside each diffracted disk, located at the exact intersection of the reciprocal lattice disk with the surface of the sphere. Since the electron wavelength is short, the modulus of vector **k** and the radius of curvature of the sphere is big: the Ewald sphere is relatively flat and HOLZ lines appear approximately straight. The electrons are transferred from the incident to a diffracted beam making the HOLZ lines to occur in pairs: to each bright line in a diffracted disk (excess line) corresponds a dark line (deficit line) in the central disk of the CBED pattern (left pattern of Fig. 4.7). The formation of the HOLZ lines is clearly represented in the sketch in the right pattern of Fig 4.7, where a number of bright (excess) HOLZ lines, due to the intersection of the Ewald sphere with the reciprocal lattice points, are shown. The corresponding dark (deficit) lines appear in a disk at a distance imposed by the imaging lens system.

Since the position of the excess or deficit lines depend on the crystal lattice arrangement, slight variations in the lattice parameters result in shifts of the HOLZ lines in the central disks. Consequently the TEM/CBED technique can be exploited to analyze strain tensors in crystals; since the diffraction pattern is the result of the interaction of the beam with the nanometric area of sample irradiated, this analysis can be performed on a nanometric scale.

4.3.2 Analysis of localized strains in crystals by CBED

The techniques currently available to measure lattice strain, such as crystal X-ray diffraction, Rutherford backscattering spectrometry and Raman spectrometry, offer a spatial resolution in the micrometric scale. It's clear that these techniques are not suitable for mapping the crystalline deformation along the cross-section of the manufactured devices given the submicrometric dimension of the structures. On the other hand, as described above, through the analysis of

the HOLZ lines in the CBED diffraction pattern is possible to extract information on the atomic arrangement of a material with nanometric resolution; this implies that the CBED technique could be employed for localized strain analysis of the nanofabricated structures. In this section we describe the procedure for deducing the values of strain tensor components from the CBED diffraction patterns.

Considering an isotropic deformation on a cubic crystal, within small angle approximation (which holds for the electron energies typical of a TEM) the differentiation of the Bragg law gives:

$$\frac{\triangle\theta}{\theta} \propto -\frac{\triangle a}{a} \propto -\frac{\triangle E}{E} \tag{4.12}$$

where a is the the lattice parameter and E is the energy of the electron beam. Eq. (4.12) shows that a variation in the distance between the reflecting plane generates a deviation of the Bragg angle at which reflection occurs. It's worth noticing that since the analyzed HOLZ lines are generated by high angle diffraction, small lattice variations can be measured.

As summoned before, any variation or uncertainty in the evaluation on the electron beam energy leads to misinterpretation on the diffraction pattern. In order to remove this ambiguity, in the preliminary step of the pattern analysis, a CBED pattern of an undeformed region of the sample is used a reference for a comparison with simulative diffraction pattern obtained through through the routine HOLZFIT. The kinematical diffraction is assumed in the simulative estimations and different diffraction patterns are simulated varying the electron accelerating voltage. The 'effective' voltage that best fits the experimental results is obtained using a χ^2 minimization criterion and is used as the effective voltage assuming that it to hold in the strained region. The kinematical character of the set of HOLZ lines chosen for the strain analysis is checked through simulative estimation of the dynamical CBED pattern for different angle of incidence of the beam, through the use of EMS software package by Stadelmann. An example of a dynamically simulated pattern at 200 kV for the case of a $< 230 >$ oriented, 240 nm thick silicon sample is shown in Fig. 4.8. If the HOLZ lines are rectilinear and their position are not dependent on the sample thickness, the kinematical diffraction regime correct: this condition has been verified for the $< 230 >$ zone axis of silicon at 200 kV, which can thus be safely employed for the strain analysis, according to the procedure that will be discussed.

The position and the distance between the HOLZ lines are then recorded through the Analysis software SIS and compared with the simulated pattern with the effective energy obtained in the preliminary stage and for different lattice parameters set $(a^x, a^y, a^z, \alpha, \beta, \gamma)$. The simulations have been carried out through the routine HOLZFIT. In Fig. 4.9 we report the CBED pattern for a $< 230 >$200 kV detected by the analysis software superimposed to the one obtained through HOLZFIT simulative software. All six lattice parameters are then extracted from a single CBED pattern, as the output of a minimization routine and the strain tensor components are calculated using the equations:

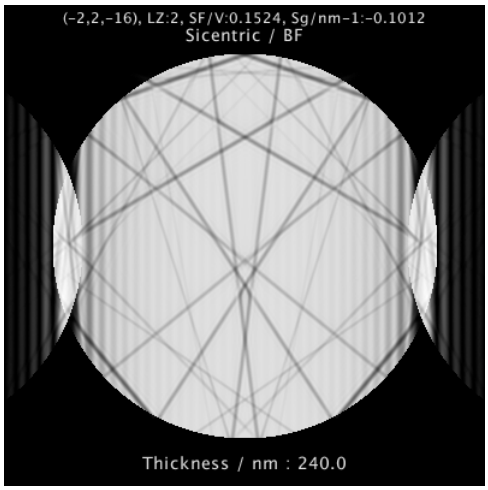

Figure 4.8: Dynamically simulated CBED pattern in $< 230 >$ zone at 200 kV of a 240 nm thick sample, from [81].

$$\varepsilon_{xx} = \frac{a_s^x - a}{a} \tag{4.13}$$

$$\varepsilon_{yy} = \frac{a_s^y - a}{a} \tag{4.14}$$

$$\varepsilon_{zz} = \frac{a_z^y - a}{a} \tag{4.15}$$

$$\varepsilon_{xy} = \frac{1}{2}(\frac{\Pi}{2} - \gamma_s) \tag{4.16}$$

$$\varepsilon_{xz} = \frac{1}{2}(\frac{\Pi}{2} - \beta_s) \tag{4.17}$$

$$\varepsilon_{yz} = \frac{1}{2}(\frac{\Pi}{2} - \alpha_s) \tag{4.18}$$

For small strain measurements and for poor quality patterns, the uncertainty associated to the HOLZ lines positions give raise to different cell parameters matching with the obtained pattern. In order to reduce the number of parameters to calculate, the symmetry on the geometry of the structures under analysis can be exploited. Let's consider for example the structure of Fig. 4.11 , similar to the ones under analysis: it's easy to show the deformation and the stress, if present, along the the crystallographic directions X ([100]) and Y ([010]) are expected to be the same since both directions form a 45° angle with [110] direction.

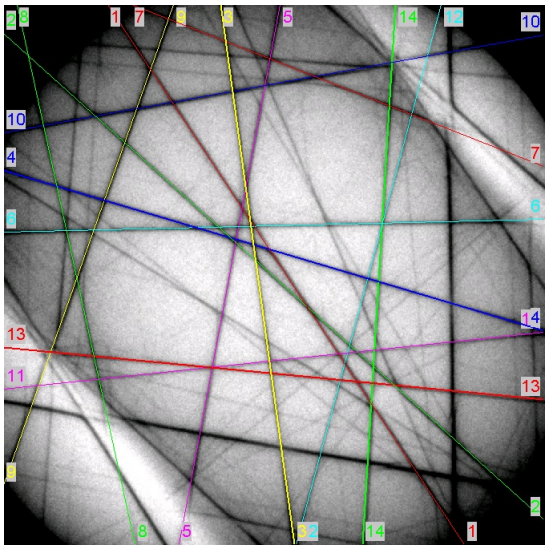

Figure 4.9: Undeformed silicon CBED pattern for a $< 230 >$ and 200 kV electron beam. The HOLZ lines, detected through the Analysis software (colored lines), have been superimposed to the experimental ones, from [81].

$$a_x = a_y \tag{4.19}$$

$$\alpha = \Pi - \beta \tag{4.20}$$

A good quality pattern can be obtained only if a sufficiently large, homogeneously strained volume of crystal is probed by the electron beam: this 'bulk' region increases with the specimen thickness. On the other hand the extension of area where a stress gradient is present is bigger for bulk high stress values, (see Fig. 4.10).

It's worth noting that the information visible in the diffraction pattern comes from the whole analyzed specimen volume. Then, as a general rule, if a good quality (analyzable) pattern is recorded in sufficiently thick specimens, it can be concluded that in that region the strain relaxation that causes the pattern to blur or disappear, although present, can be neglected. This consideration leads to the conclusion that the bulk condition can be assumed for the sample, and consequently the so-called plane strain approximation $a_z = 0$, can be used. Due to this assumption, the number of parameters is further reduced, as shown in Fig 4.12, $a_x = a_y$ and $\alpha = \Pi - \beta$, and the deformation can be expressed as:

$$\frac{\triangle a_x}{a_x} = \frac{\triangle a_y}{a_y} = \frac{\triangle \gamma/2}{1 - \triangle \gamma/2} \simeq \triangle \gamma/2 \tag{4.21}$$

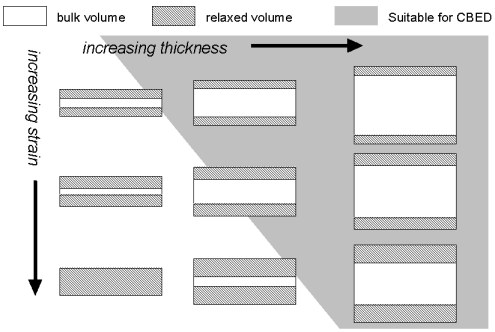

Figure 4.10: Schematic of the bulk and relaxed volume, sampled by the electron beam as a function of sample thickness and strain, from[81].

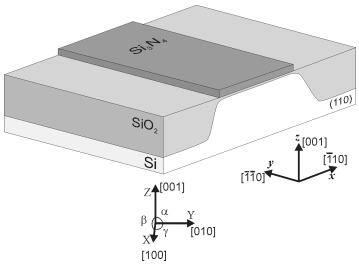

Figure 4.11: Crystal axes orientation (X,Y,Z) with regard to the sample reference axes (x,y,z) for a Shallow Thrench Isolation structure, from[81].

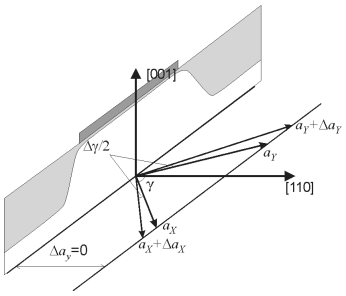

Figure 4.12: Relation between the strain tensor components $\varepsilon_{xx}(=\varepsilon_{yy})$ and the parameter $\triangle\gamma$ under plain strain approximation ($\Delta a_y = 0$), from [81].

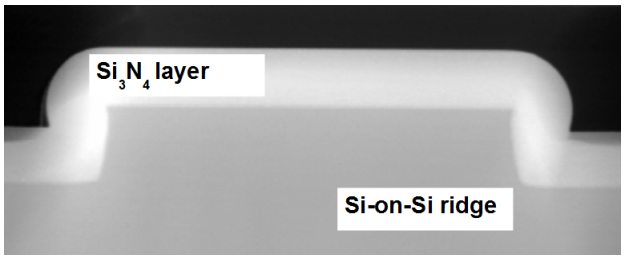

Figure 4.13: STEM image of the micrometric silicon ridge.

4.4 Results of Scanning Transmission Electron Microscopy (STEM) analysis

Scanning transmission electron microscopy (STEM) is an analysis technique carried out at TEM facility that combines the principles of TEM and SEM. The electron beam is focused on a submicrometric area, as for the CBED technique, and scanned across the sample section in a raster pattern. Through an high angle annular disk detector the scattered electrons are collected and the produced signal is amplified and used for the generation of the image. This kind of signal is the result of the incoherent scattering between the beam and the atomic nuclei and provides point-to-point information on the elements of the sample. In particular, the contrast between the signal corresponding to 2 different points is due solely to the atomic number Z and not to the orientation of the specimen, as for low-angle coherent diffraction. Therefore this technique allows to observe details at the interfaces between regions of different Z with nanometric resolution limited only by the spot diameter since no objective lenses are used for directing the images on the screen.

In Fig. 4.13 a STEM image of the micro fabricated silicon ridge is reported. As described, in STEM images a correspondence between the image contrast, coded in gray scale, at any point and the atomic number of the area irradiated by the electron beam is observed. In the images under analysis the white color corresponds to the silicon nitride layer, the gray color to silicon and the black to the epoxy resin uses in sample preparation.

The geometry of the ridge is well defined: the vertical and the horizontal sidewalls are sharp and no cracks or jaggedness are observed. The ridge shape is trapezoidal as expected due to the chemistry employed in the plasma based dry etching processes. The silicon nitride layer has been conformally deposited on the silicon structure. Despite the high intrinsic stress of the Si_3N_4 film, no delaminations or detachments have occurred at the interface due to the good adhesion between the films which has been obtained through the deposition technique employed. Swellings at the upper vertices of the ridge can be observed as a result of the kinetics in the step coverage; the dimension and the shape of the bumps are dependent on the aspect ratio of the structure and on the deposition technique parameters.

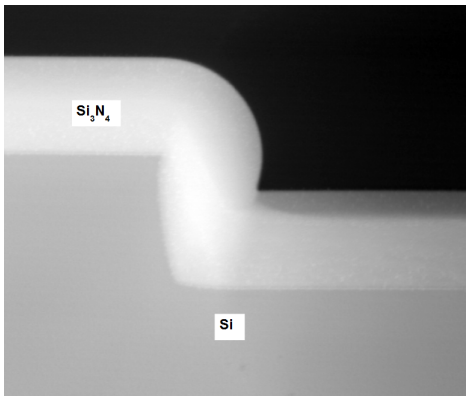

Figure 4.14: Particular of Fig. 4.13, focused on the vertical sidewall of the microfabricated silicon ridge.

Fig. 4.14 reports a particular of Fig 4.13 focused on the shape of the vertical sidewall. The edge is not straight and a slight a curvature toward the inner part of the ridge is observed. As described in Chapter 3, the chlorine chemistry based dry etching employed is not purely physical and the chemical contribute brings to a partially isotropic etching which generates a spherical shaped patterning.

Fig. 4.15 reports a STEM image of the silicon ridge which has been nanofabricated through the employment of the spacer pattering method technique.

As for the microfabricated ribs, the geometry is well-defined: the sidewalls of the structure do not present any appreciable defects and no jaggedness or undulations, that in SOI waveguides would cause scattering and losses on the traveling radiation, are observed along the vertical edges. The silicon nitride spacer dimensions and the anisotropy of the dry etching processes employed proved to be suitable for the patterning of the silicon nanowire: the observed dimensions, around $(220 \times 450)\ nm$, match the expected dimensions of a single mode SOI waveguide. The trapezoidal shape of the ridge and the light curvature in the vertical sidewalls directed to the interior of the waveguide are similar to those observed for micrometric silicon ridge. No flaws ascribable to the fabrication process is present in the inner area of the ridge or in the surrounding area: the shading observed under the structure are induced by the lapping processes and the FIB milling employed in the TEM sample preparation procedure. The observed dark spots, which are scattered in a disordered pattern inside the waveguide and in the substrate, are the points where the high energetic electron beam has been focused.

Fig 4.15 shows a conformal adhesion of the stoichiometric silicon nitride layer which has been deposited through the LPCVD technique. The Si_3N_4 film uniformly covers the ridge sidewalls and the substrate and does not show any detachment or irregularity in the adhesion along the interface. Despite the high intrinsic stress of the film and the significant expected strain along the ridge section, no cracks or delaminations are observed in the ridge or in the cladding

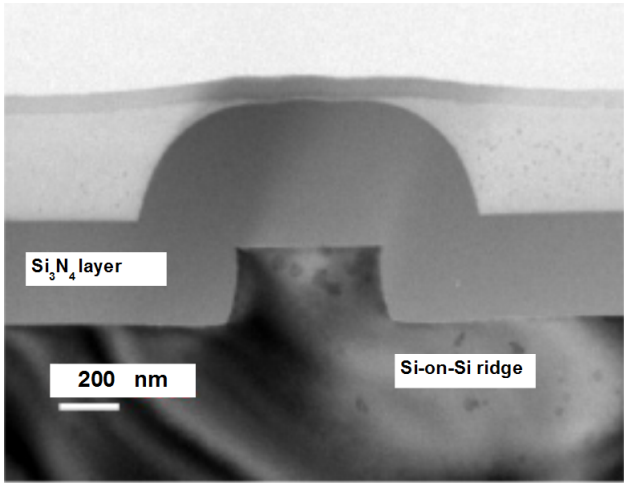

Figure 4.15: STEM image of the nanometric silicon rib structure (rib-cross section $(450 \times 220)\ nm$).

layer. It's worth noting that the shape of the silicon nitride layer is quite different from the one observed for the micrometric waveguide: no bumps are visible in correspondence of the ridge vertices. This absence is likely to stem from the different height of the structure with regard to the micrometric structures: the reduced aspect ratio of the nanometric structures limits the insurgence of the step coverage phenomenon.

The thickness of the silicon nitride layer on the top of the ridge is greater than the one observed in the rest of the interface: this difference is due to the presence of the spacer mask topping the horizontal sidewall of the structure. In Fig. 4.16, the discontinuity in SiN distribution reveal the presence of the thin layer used as a hard mask for the nanopatterning that has been covered by the 300 nm thick SiN layer subsequently deposited. The different timing of the deposition causes the distribution of the silicon nitride layer not to be uniform.

Fig. 4.17 reports a STEM image of the coupling region in one of the nanofrabicated structures. The definition of the geometry is good and the shape of the ridges is trapezoidal as the case of the single nanometric guide. No imperfections in the inner sidewalls of the structure or any asymmetry in the patterning of the structures can be observed. The height values of the ridges on both sidewalls don't show appreciable differences; this implies that the patterning has been successfully carried out over all the coupling section. The STEM analysis show that the etching processes have not been impaired by the closeness of the silicon ribs and the technologically challenging submicrometric gap definition, in this case around 300 nm wide, has been correctly accomplished. The silicon nitride layer has been conformally deposited on the waveguides in the coupling section and no delaminations or imperfections are observed in correspondence of the center of the gap. It's worth noting that the Si_3N_4 distribution is uniform

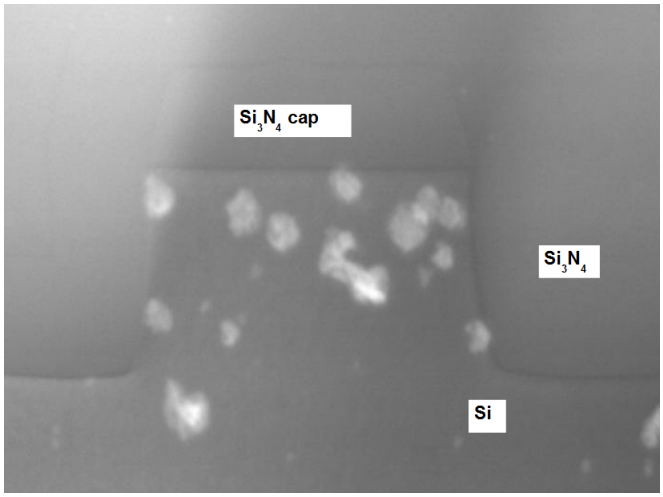

Figure 4.16: STEM image of the nanometric silicon ridge geometry.

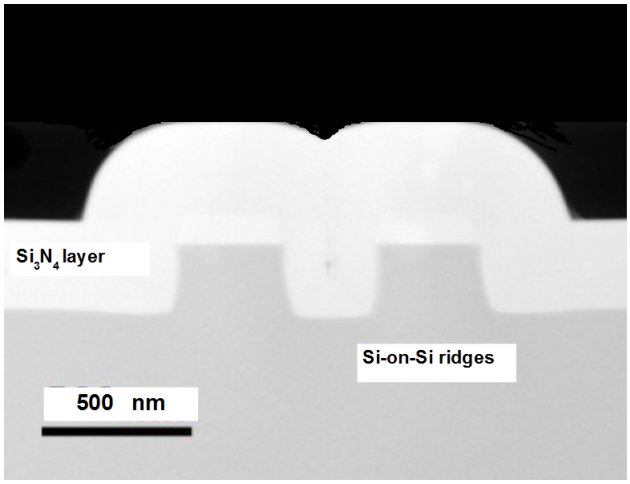

Figure 4.17: STEM image of the nanometric coupled silicon rib structure (rib-cross section $(450 \times 220)\ nm$)).

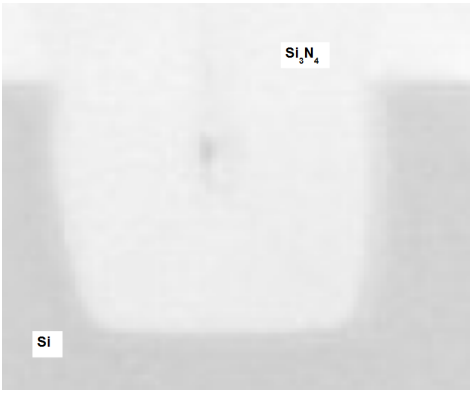

Figure 4.18: Particular of Fig. 4.17: step coverage at the coupling region of the rib structure.

across all the section except a tiny section, as shown in Fig. 4.18 where a small void is observed: the presence of this nonideality is probably the result of the junction between the two Si_3N_4 layers covering the two waveguides occurred at an intermediate step of the deposition. At height values greater than this point the Si_3N_4 distribution is uniform; this implies that deposition of the upper layers has been approximately planar.

4.5 Results of scanning electron microscopy (SEM) analysis

The scanning electron microscope (SEM) uses a focused beam of high-energy electrons to generate a variety of signals at the surface of solid specimens. The signals that derive from electron-specimen interactions reveal information about morphology, chemical composition, crystalline structure and orientation of the materials of the sample[83]. In particular, when the electron beam is irradiated on a specimen surface, the interaction with the atoms at different depth values produce various kinds of signals carrying different types of information, (see Fig. 4.19), as listed in table reported below:

Signal	Information Carried
Secondary Electrons	Topographical observation of the surface
Backscattered Electrons	Compositional observation of the surface
X-Rays	Elemental analysis of specimen
Transmitted Electrons	Internal structure observation
Cathodoluminescence	Internal characteristic observation
Electromotive Force	Internal characteristic observation

SEM analyes has been carried out on the nanofrabricated devices in order to obtain topographical information on the quality of the structures and on the

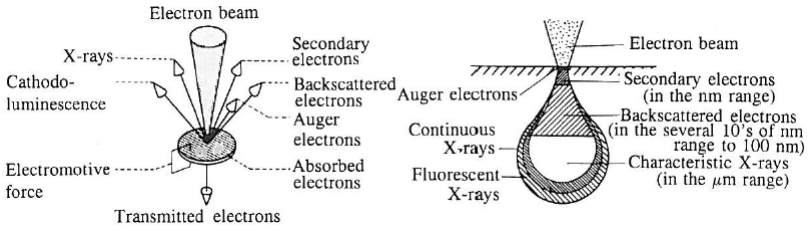

Figure 4.19: Schematic representation of the signals emitted from the sample (left) and the theirs interaction volume (right), from [84].

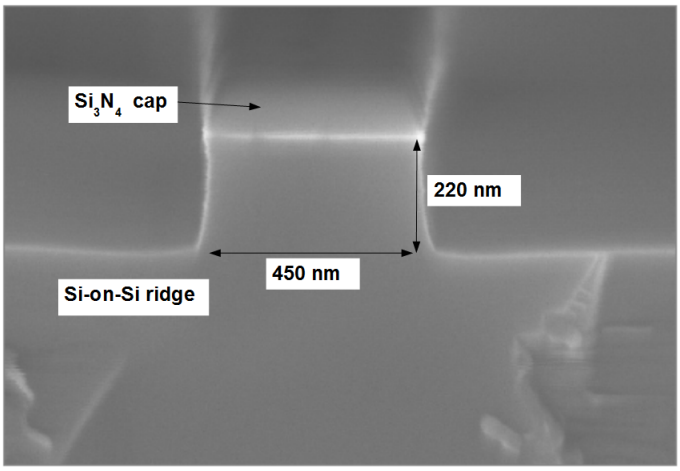

Figure 4.20: SEM image of a silicon rib structure (rib-cross section (450×220) nm)).

reliability of the nanofabrication processes employed for the manufacturing.

Fig. 4.20 reports a SEM image of a silicon rib cross-section at the intermediate fabrication step preceding the silicon nitride layer deposition. The geometry is well defined and width and height values of the ridge observed are the ones observed at at STEM analysis.

Fig. 4.21 reports STEM images of two waveguides, distanced by a submicrometric gap (less than 600 nm), which are observed at tilted angle with regard to the sample plane. As for Fig. 4.21, the image has been captured before the deposition of silicon nitride straining layer. This inclination allows to observe both the planar geometry of the nanofabricated devices and the transverse section of the facets. The two ridges are straight and parallel and no interruptions or discontinuities are observed along the direction of propagation. The SEM analysis shows that the structure geometry does not vary in the observed area of the sample and that no defects or unwanted microbending, that could impair

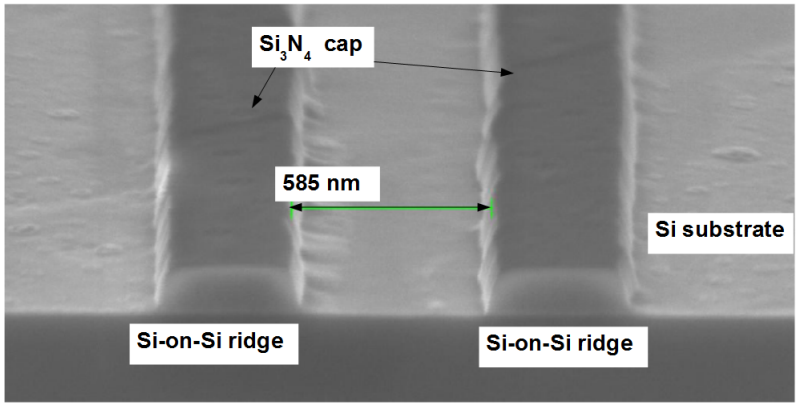

Figure 4.21: SEM image of the nanometric coupled silicon rib structure (rib-cross section $(450 \times 220)\ nm$)).

the propagation of light traveling in SOI devices with the same geometries, are present. At the same time, it's possible to observe undulations on the vertical sidewalls, which are uniformly distributed along the structures. As described in Chapter 2, such nonidealities stem from the dry etching patterning process employed and can't be avoided. The impairment which the radiation scattering, induced bu such surface roughness, induces on the SOI waveguides performance, has been estimated through propagation loss measurements. The results of such measurements are reported in Chapter 5.

Fig. 4.22 reports a SEM image of the coupling section of a nanofabricated silicon rib microring. The obtained geometry are equal to those observed in the straight single and coupled rib structures and no flaws are shown. The ring coupling section lies in the center of the sample, at a distance of about 2.3 mm from the facets of Fig. 4.21 and Fig. 4.22. Comparing such STEM images, it's possible to observe that all structures are equally sharply defined; these results, together with other STEM images non reported here, show that the patterning of the structures has been uniformly accomplished across the the whole area of the sample. The bent section, despite the relatively small values of the microring radius of curvature (about 30 μm), is well defined; comparing the observed results with the STEM images of straight waveguides, no appreciable differences in surface roughness at vertical sidewalls can be observed.

Fig. 4.23 reports a SEM image of ridge silicon waveguide, which as been manufactured on SOI platform, before deposition of the silicon nitride cladding film. The observed structure is solely topped by the Si_3N_4 cap used as hard mask in the nanopatterning processes. The buried oxide (BOX) layer is visible due to the deep etching of the silicon device layer. The SEM analysis shows that the geometry of the waveguide is uniform in the whole are of the sample which is represented in the image. No abrupt variation in the cross-section the waveguide or microbendings, that could impair the optical propagation of the

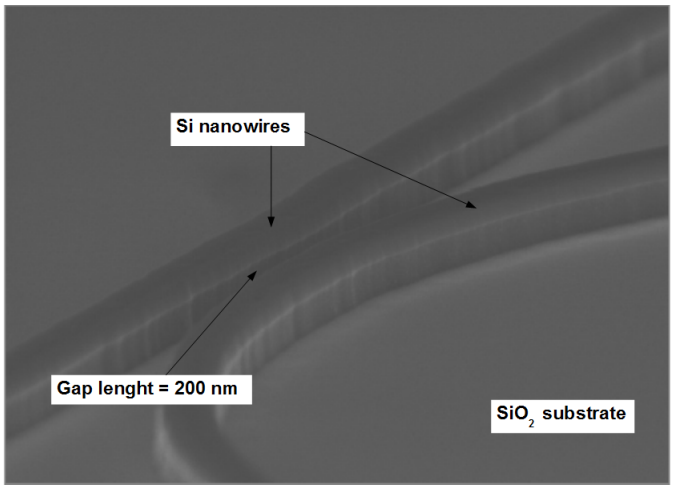

Figure 4.22: SEM image of a nanofabricated silicon microring at the coupling region (rib cross-section $(450 \times 220)\ nm$)).

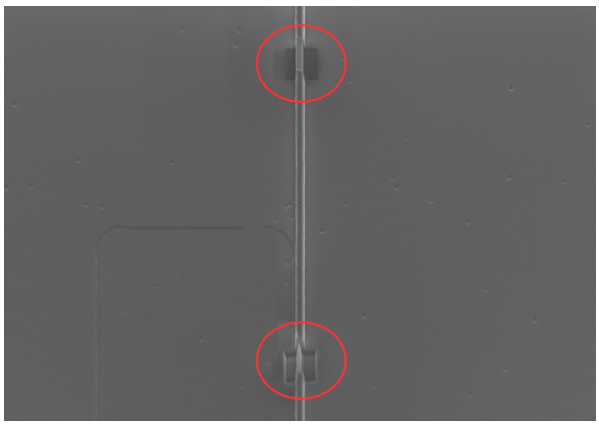

Figure 4.23: SEM images of a nanofabricated SOI waveguide (ridge cross-section $(450 \times 220)\ nm$)).

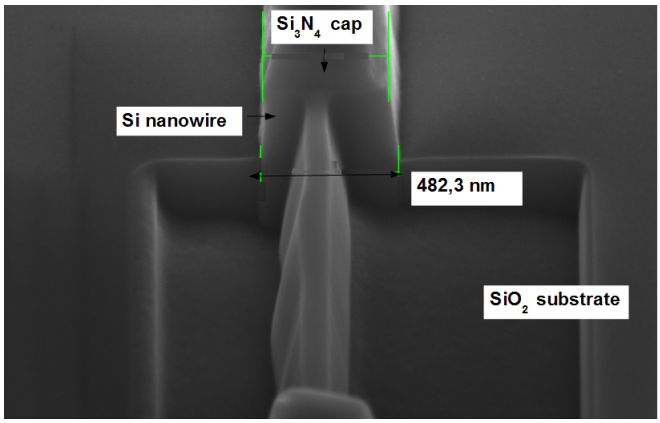

Figure 4.24: SEM images of a manufactured SOI waveguide in correspondence of the FIB ablation.

device, are observed.

In the SEM images some holes can be observed where the width of the waveguide is reduced and the BOX layer is partially etched. In such area we have used a Focused Ion Beam (FIB) to bare a cross-section of the device and obtain information on the geometry and dimensions of the silicon nanowire. This ablation technique requires an ion beam, with a nanometric spot, to be focused the sample surface and scanned across a micrometric area. The high-energy gallium ions strike the sample and sputter atoms from the surface removing the material in the selected area uncovering part of the section.

A detail of the area undergone to the FIB ablation is reported in Fig. 4.24. The ion beam caused the thinning of the waveguide and the removal of the superficial layer of the BOX that allowed us to observe the cross-section of the structure. The observed geometry of the silicon nanowire is well defined and the shape is trapezoidal as the case for the nanometric structures manufactured on silicon substrate. The obained dimension of the silicon nanowire (450×220) nm), match the expected dimensions of a single mode SOI waveguide.

Fig. 4.25 reports a SEM image of a waveguide endface undergone to the lapping process, described in Chapter 5 after the deposition of the silicon nitride layer. The waveguide structure does not appear damaged by the polishing process: the geometry is still neatly visible and no fragmentation or cracks in correspondence of the sidewalls or in the inner part have occurred. Furthermore, the adhesion of the silicon waveguide to the buried oxide has proved to be resistant to the pulling action produced by the lapping. Due to the strong adhesion of the silicon nitride layer to the silicon, the Si_3N_4/Si interface does not show any detachment or fragmentation. Also for the SiN/SiO_2 interface, the adhesion proved to be strong enough to withstand the mechanical stress induced by the lapping processes.

Along the horizontal direction, at approximately 100 nm below the base of

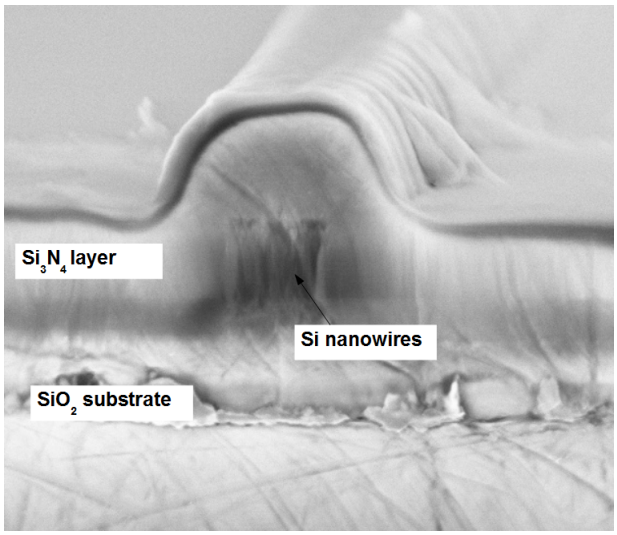

Figure 4.25: SEM image of the facet of a manufactured SOI waveguide undergone the lapping process.

the waveguide, it's possible to observe a delamination in the BOX layer. Similar cracks in the BOX have been observed in other SOI waveguide facets undergone lapping process or or other polishing processes, such as those employed for TEM sample preparation. The detachment extends along the width of the sample distancing the substrate from the pulled part containing the waveguide and a thin layer of silicon dioxide. Inside the crack, few nanometers high, particulate dirt can be collected, as shown Fig. 4.26.

The structural weakness shown by BOX layer is likely to be determined by the wafer bonding technique employed in the SOI fabrication processes which make that part of the section more to break or delaminate. In comparison with the Si/SiO_2 or Si/Si_3N_4 interfaces, the bonding area is weaker and if it is undergone to mechanical stress as those induced by the lapping processes, could break. On the other hand the waveguide does not have interruptions or breaks along the direction of propagation. Only a slight bend, directed upward, can be observed near the edge of the sample; nevertheless, due to the smoothness of the curvature we don't expect that impairments on the optical properties of the waveguide could stem form this defect. The experimental meaurements of the propagation losses of the manufactured SOI waveguides have confirmed such hypotheses and are reported in Chapter 5.

In conclusion, the TEM and SEM analyses, which we have carried out on the manufactured silicon structures and SOI waveguides, show that the employed CMOS nanofabrication processes and the SPM technique can be fruitfully employed for the manufacturing of micrometric and nanometric silicon structures. Furthermore the SPM techniques allowed us the accurately define nanomet-

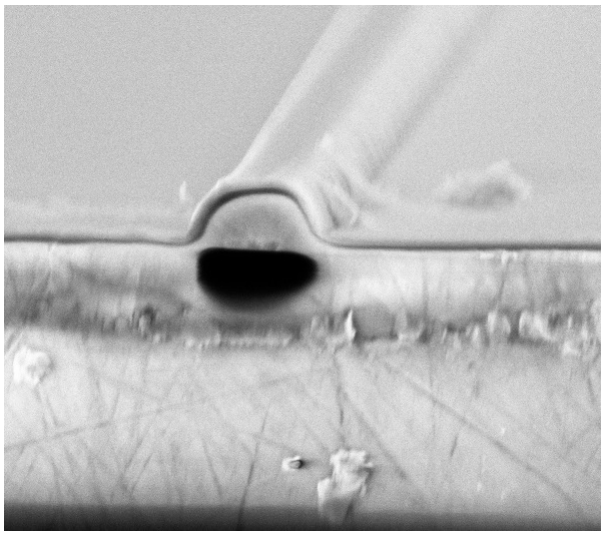

Figure 4.26: SEM image of the SOI waveguide of Fig. 4.25 at a distance. A small bend is observable in correspondence of the detachment of the layer containing the SOI waveguide.

ric features and gaps starting from micrometric lithography and, in particular, to nanofabricate SOI waveguides with the expected geometry and dimensions. Nevertheless, such analyses show that the strained silicon technology and SPM technique are compatible and can be employed for the manufacturing of strained silicon photonic devices.

Chapter 5

Results: strain analysis of silicon structures and electromagnetic properties of SOI devices

As discussed in Chapter 1, the optical properties of strained silicon photonic devices are strongly dependent on the extent and spatial distribution of the lattice deformation. In order to perform reliable analysis on the behavior of such devices, it is therefore necessary to have accurate tools for the estimation of stress and strain distributions on photonic structures. In the light of these considerations, we have developed a simulative model, based on the finite element method (FEM), for the estimation of the mechanical properties of strained silicon devices. We have employed the developed FEM simulative model to estimate the lattice deformation on the manufactured silicon rib structures and compared these results with the strain distributions which have been experimentally estimated through the convergent beam electron diffraction (CBED) technique. The CBED technique is carried out at TEM facilities and provides nanometric spatial resolution as well as sensitivity of the order of tens of microstrain. The comparative analyses allowed us to validate the FEM model and assess the accuracy of the strain estimations. Then, we have employed a multiphysical simulative model, based on the validated FEM model, to estimate the optical properties of the strained silicon-on-insulator (SOI) waveguides, and the impact of experimental technological nanofabrication parameters on the performance of such devices. Finally, we have carried out a simulative and experimental analysis on the guiding properties of the nanofabricated (SiPh) devices in order to assess the quality of the manufacturing processes employed as well as the compatibility the Spacer Patterning Method technique with the strained silicon technology. In particular, we have performed the characterization of the

manufactured strained SOI waveguides in terms of guiding properties and the propagation loss, through the employment of the Fabry-Perot (FP) resonance technique.

In this Chapter we report some results of the discussed-above simulative and experimental analysis which we have carried out on the mechanical, structural and electromagnetic properties of the strained silicon photonic devices. Part of the reported results has been presented in the works: [86, 87, 88, 89, 90, 91, 92]. In Section 1 of this Chapter we report the outcomes of the simulative estimations of stress and strain distributions on the microfabricated and nanofabricated silicon ridges. Then, we present the results of the comparative analysis between such estimations and the measurements of lattice deformation which have been obtained through the employment of the CBED strain measurement technique. In section 2 we describe some results of the simulative analysis which we have carried out on the electromagnetic properties of the strained SOI devices, focusing on effective refractive index, effective group index and birefringence of the manufacured waveguides. Finally, in section 3, we present the results of the propagation loss measurements, performed on the manufactured SOI devices, through the employment of the Fabry-Perot resonance technique.

5.1 Lattice deformation analysis of the micrometric and nanometric strained silicon ridges

As discussed above, induced strain and stress fields on fabricated micrometric and nanometric silicon rib structures have been numerically estimated using the simulative model which we have described in Chapter 2. Such model is based on the finite element method (FEM) numerical technique and has been implemented through the employment of the commercial software COMSOL. The geometries and dimensions of the structures and other experimental technological nanofabrication parameters, such as the Si_3N_4 film thickness, have been inferred through the analysis of Scanning Transmission Electron Microscopy (STEM) images and Scanning Electron Micorscopy (SEM) images, which we have reported in Chapter 4.

5.1.1 Strain analysis

The performed STEM analyses show that the shape of the micrometric silicon ridges, determined by the dry etching patterning processes, is trapezoidal. The vertical sidewalls are inclined at 7° to the normal direction to the substrate plane. The observed width and height values of the manufactured silicon ridges are 2.32 μm and 465 nm, respectively. A 345 nm thick silicon nitride film has been conformally deposited on the structures and swelling, induced by the occurrence of the step coverage phenomenon, can be observed at upper ridge vertices, as shown in Fig 5.1.

Fig. 5.2 reports the STEM images of the nanofabricated silicon ridge and the corresponding geometry employed in the simulative model. With regard to the

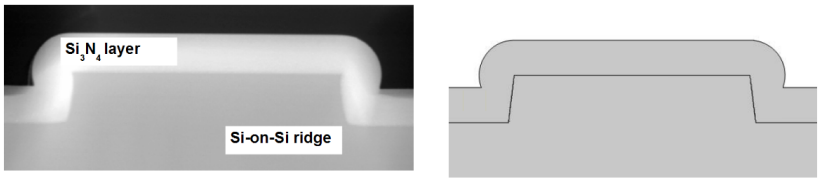

Figure 5.1: STEM image of a manufactures micrmetric silicon rib structure (left) and corresponding geometry employed in the FEM-based simulative estimation (right).

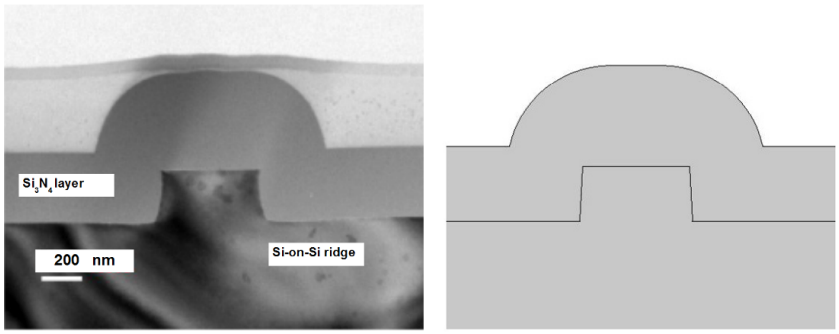

Figure 5.2: STEM image of a nanofabricated silicon rib structure (left) and corresponding geometry employed the simulative estimation (right).

micrometric ridge, the inclination of the vertical sidewalls is reduced to 3° and the swellings in the silicon nitride film are less pronounced. Furthermore, the Si_3N_4 thickness is not uniform: a difference of more than 100 nm between the part covering the waveguide and the one topping the silicon substrate is observed due to the presence of the Si_3N_4 cap used as hard mask for the patterning of the structure, as described in Chapter 2. The obtained values for height and basis width of the ridge are 220 nm and 481 nm, respectively, and the silicon nitride thickness values for the cladding layer of the substrate and the waveguide are 325 nm and 440 nm respectively.

In order to estimate the stress and strain distributions on the ridge cross-section, the elastostatics equilibrium equations, described in Chapter 2, have been numerically solved through the FEM method using the inferred geometries. The stiffness tensor given in Eq. (2.17) has been employed in the constituive equations for silicon, in order to take into account the anisotropic mechanical properties of such material, as described in Chapter 2. As for silicon nitride, the following isotropic elastic values for the Young's modulus E and Poisson's ratio ν have been used:$E = 270MPa$ and $\nu = 0.27$. The intrinsic stress of the Si_3N_4 layer σ_{int}, evaluated through experimental measurements of wafer curvature, is $1.1\,GPa$.

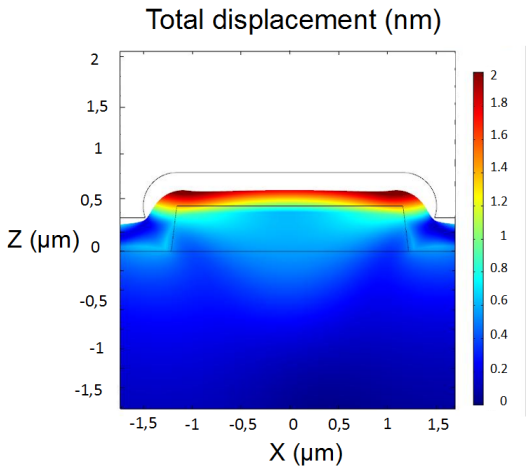

Figure 5.3: Simulative contour plot of total displacement over the manufactured micrometric rib cross-section.

Fig. 5.3 and Fig. 5.4 show the estimated total displacement distributions $|u|$, defined in Eq. 2.1, for the silicon micrometric ridge and nanometric ridge. The displacement distributions, enhanced by a 100× deformation scale factor, show that for both the nanometric and micrometic ridges, the high tensile intrinsic stress film tends to curve the substrate so that the silicon wafer is bent upward. As a result, the waveguide is expanded in the horizontal direction and shrunk in the vertical direction as can be observed through the comparison between the displacement distributions (the contour plot) and the original geometry (continuous black line).

Then, we have estimated the distributions of the in-plane strain tensor components $\varepsilon_{xx}, \varepsilon_{zz}, \varepsilon_{xz}$, where x and z directions are the horizontal and vertical directions of the cross section, respectively. The simulative results for the micrometrc ridge, reported in Fig. 5.5, show strain values of the order of the millistrain with maximum values obtained at the Si/Si_3N_4 interface. The ε_{xx} and ε_{zz} components are symmetrically distributed with regard to the rib vertical axis and their sign is positive and negative around the entire rib cross section, respectively. The maximum values for the ε_{xx}component are 2.3 $m\varepsilon$ while for $\varepsilon_{zz}$the maximum values obtained are -2.2 $m\varepsilon$. The silicon nitride film is compressive-strained in both directions; this gives rise to a discontinuity in the strain distribution across the interface for the ε_{xx}component. The spatial distribution of the shear strain component ε_{xz} is found to be anti-symmetric to the rib vertical axis, as expected from theory. The maximum values for the strain tensor component ε_{xz} , which have been obtained at the ridge vertexes, are ± 1.8 $m\varepsilon$. Vertical and shear strain components do not show discontinuity across the $Si - Si_3N_4$interface.

The FEM-based simulative model has been therefore employed for the es-

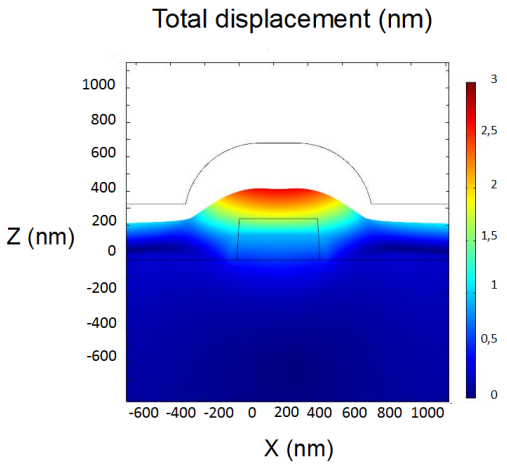

Figure 5.4: Simulative contour plot of total displacement over the nanometric rib cross-section.

timation of the strain distributions on the nanofabricated single and coupled rib structures. The results for the strain tensor components ε_{xx}, ε_{xz} and ε_{zz} are reported in Fig. 5.6. The strain field spatial distribution across the nanometric single waveguide cross-section are similar to the ones observed for the micrometric ridge analysis: we have obtained symmetric behaviors for ε_{xx} and ε_{zz} components and anti-symmetric behavior for ε_{xz} component. Large strain values of the order of a few $m\varepsilon$ for all tensor components are observed near rib sidewalls. In particular, maximum strain values of 2.8 $m\varepsilon$ for ε_{xx}, -3.1 $m\varepsilon$ for ε_{zz} and ± 3.5 $m\varepsilon$ for ε_{xz} have been obtained. The simulative results show that no remarkable differences are expected to occur between the strain distributions of the micrometric and nanometric structures. On the other hand, the reduced dimensions of the ridge leads to an increase of the surface/volume ratio of the silicon wire; this implies that the nanometric area where remarkable strain values are observed, which is confined at Si/Si_3N_4 interface in the micrometric ridge, extends over the entire nanometric structure. In particular, horizontal and vertical strain tensor components, ε_{xx} and ε_{zz}, show values of the order of the millistrain in correspondence of the center of the waveguide. Since the TE mode intensity distribution, as described in Chapter 2, is mainly concentrated in the center of the silicon nanowire, the strain field induced by the high intrinsic stress Si_3N_4 film is expected to significantly affect the optical properties of the SOI waveguide.

The simulative results which we have obtained for the coupled rib structures, (Fig. 5.6 (b)), do not show significant differences with regard to analysis carried out on the single rib: the attained order of magnitude of the strain tensor components values together with the symmetry of their spatial distribution are comparable. A slight deviation from the results obtained for the single rib structure is observed for the vertical strain component: Fig 5.6 (b) shows greater

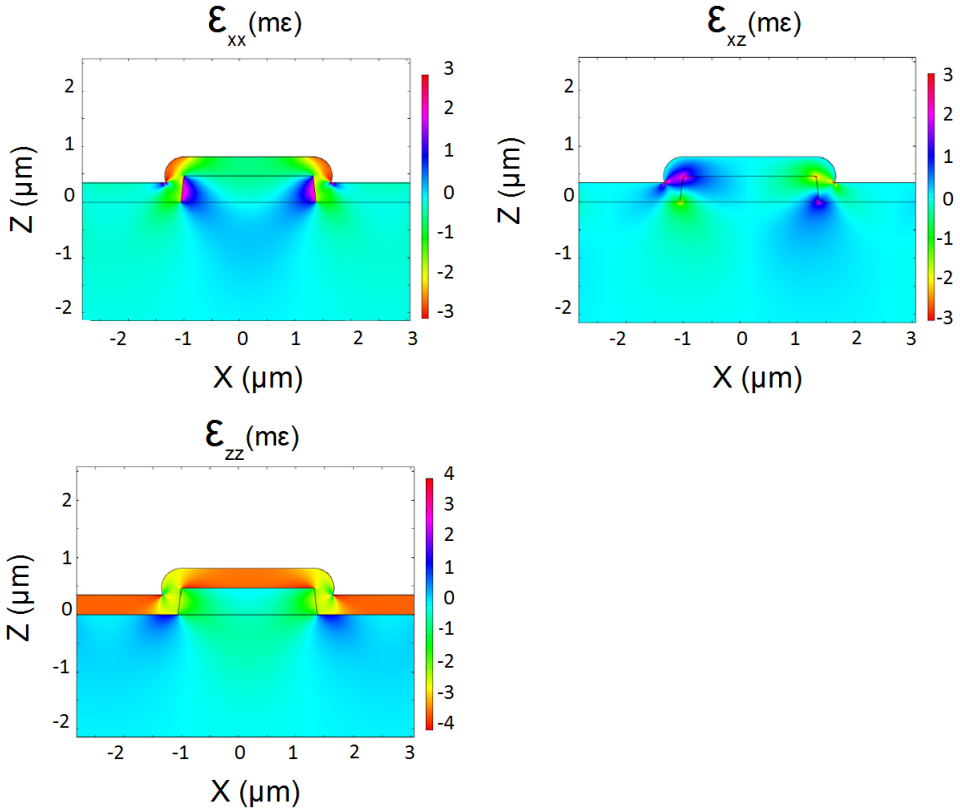

Figure 5.5: Simulative contour plots of strain distribution over the micrometric rib cross-section (ε_{xx}, ε_{xz} and ε_{zz} components).

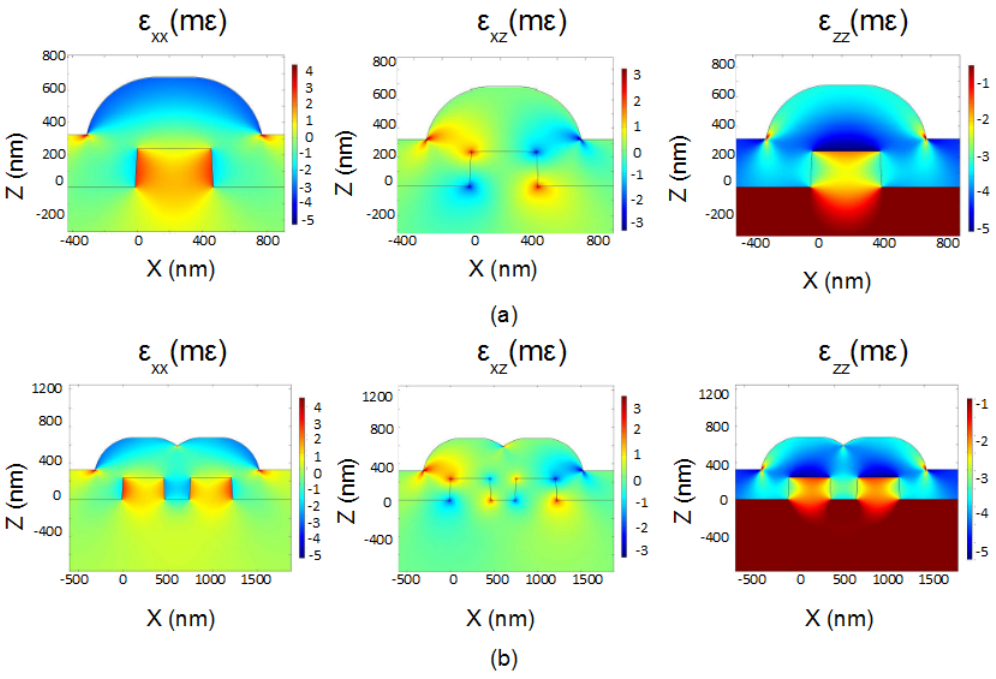

Figure 5.6: Simulative contour plots of strain distribution (ε_{xx}, ε_{xz} and ε_{zz} components), over the cross-section for single rib (a) and coupled rib (b) structures.

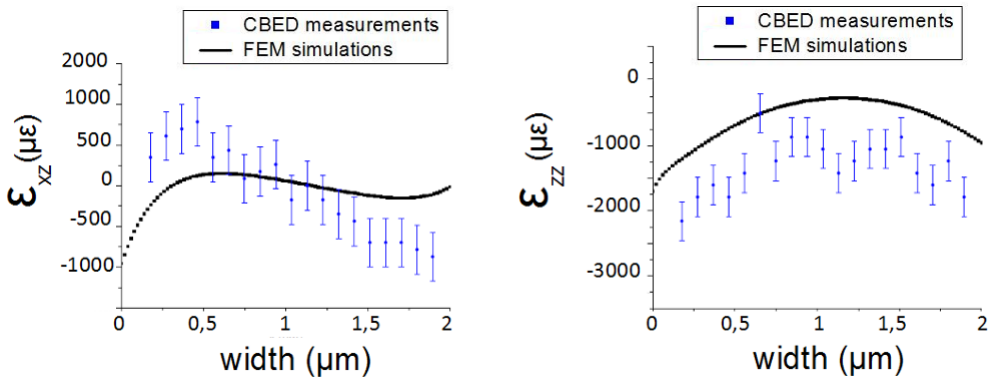

Figure 5.7: Estimated and measured distributions for strain tensor components ε_{xx} and ε_{zz}, along the micrometric rib width at 65 nm from rib bottom floor.

ε_{zz} values at the inner vertical sidewall and an asymmetric distribution with regard the center of the rib. Such result is likely to stem from the different amount of silicon nitride that is deposited on the sidewalls . We therefore expect that the optical properties of the SOI waveguides, in the coupling section, do not significantly differ from those of single waveguides and the performance of such devices is not impaired by modal mismatch between the single and coupling sections that could be generated by different strain distributions.

5.1.2 CBED strain measurements

We have carried out a comparative analysis between the results reported in the previous section and the strain values distributions, obtained through TEM/CBED measurements, on the manufactured strained structures. The aim of such investigation is to evaluate the possible use of such analysis techniques for the study of micrometric and nanometric silicon structures and the accuracy such simulative and experimental estimations. As described in Chapter 4, the commonly employed techniques for measuring lattice strain, such as crystal X-ray diffraction and Raman spectrometry, have micrometric spatial resolution and are not suitable for the analysis of nanometric devices. This implies that no experimental data on lattice deformation of similar structures are available and that the accuracy of the FEM-based method and CBED technique cannot be evaluated through a comparison with literature data. We therefore believe that a comparative analysis between the values obtained through the FEM simulative method and the CBED technique can provide important information for the validation of the two analysis techniques as well as the evaluation of the accuracy of theirs results.

Some results of the comparative analysis between the FEM-based simulative estimations and the CBED measurements are reported in Fig. 5.7 and Fig 5.8. Fig. 5.7 reports the ε_{xz} andε_{zz} strain tensors components distributions along

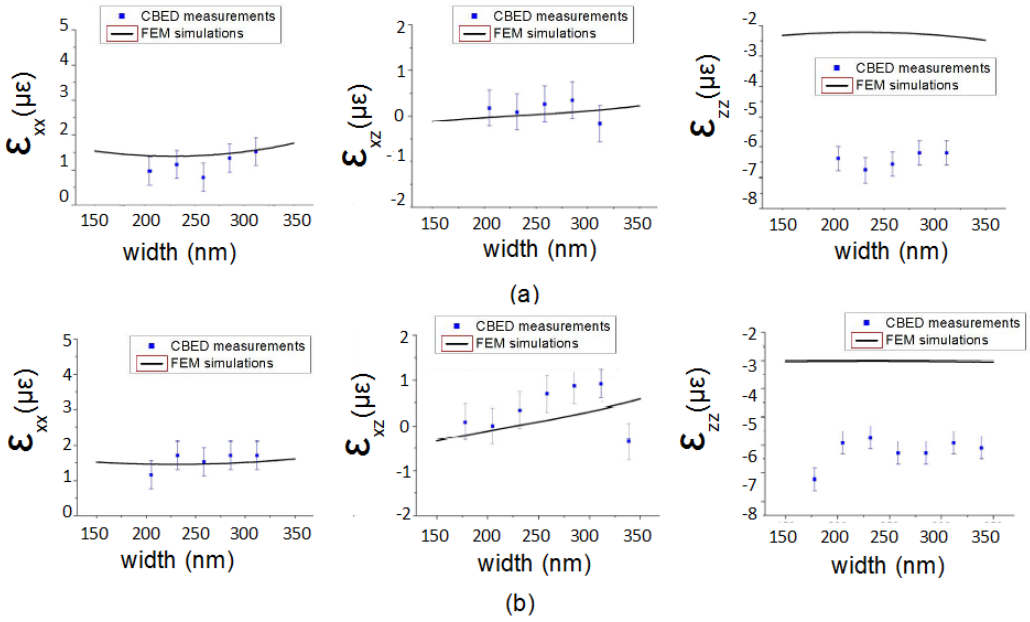

Figure 5.8: Estimated and measured strain distributions, for strain tensor components ε_{xx}, ε_{xz} and ε_{zz}, along the nanometric width (at 92 nm and 12 nm height from rib bottom floor).

the silicon micrometric ridge at 65 nm height from the rib bottom floor. Fig. 5.8 shows the distributions of the strain tensor components ε_{xx}, ε_{xz} and ε_{zz} along the silicon nanometric ridge at 92 nm (a) and 12 nm (b) height from the rib bottom floor. A qualitative agreement can be observed for both micro-ridge and nano-ridge analyses: simulative and experimental data show a symmetric behavior with regard to the center of the waveguide for ε_{xx} and ε_{zz} components and an asymmetric behavior for ε_{xz} component; the sign and the order of magnitude of the strain values of all the analyzed components match. Furthermore, the measured values of ε_{xx} and ε_{xz} show a quantitative agreement with the estimated ones while for ε_{zz} a systematic discrepancy is observed. The results show that the vertical deformation extent is systematically underestimated: for the nanometric ridge at 12 nm height, the CBED measurement yield strain values around t$-6\,\mu\varepsilon$ while the estimated ones reach values of about$-2\,\mu\varepsilon$. On the other hand both data sets are distributed in an approximately flat line along the region of analysis. This offset is likely to be determined by the preparation technique employed for the TEM analysis. This procedure, described in Chapter 4, requires the thinning of the sample, along the direction normal to cross section, down to200 nm. The reduction of slices thickness down to submicrometric values alter the bulk condition assumed for the simulative model and make the sample subject to deformations until an equilibrium state is achieved. This phenomenon, named strain relaxation, could also cause a variation on the orthogonal deformation of the sample and consequently a discrepancy with the estimated data, since, as summoned before, the simulative model assumes a plain strain condition and does not take into account the insurgence of this effect. It's worth noting that the observed discrepancy in the micrometric ridge analysis is less evident. As explained in the Chapter 4, the stress relaxation and consequently the volume in witch the strain is relaxed is larger for greater amount of strain. Since in the micrometric analysis the extend of the obtained strain is less the one observed in nanometric structure, the stress relaxation induced by the thinning is expected to effect less severely the sample justifying the better agreement between the simulative and experimental data.

In conclusions, the comparative analysis between the FEM-based developed model and CBED measurement technique, which we have carried out on the manufactured silicon structures, has demonstrated a good agreement between the simulative estimations and the experimental measurements. The investigated analysis techniques have been shown to provide accurate evaluations of lattice deformations on micrometric and nanometric silicon structures which can be used for the investigation of the electromagnetic properties of photonic devices based on strained silicon technology.

5.2 Electromagnetic properties of the manufactured strained SOI waveguides

In the previous section, we reported the results of a comparative analysis between the developed FEM-based simulative model and the CBED measurement technique that allowed us to estimate the accuracy of the two analysis techniques. In particular, the FEM-based model has been shown to provide reliable estimations of strain distribution and can be therefore employed for the analysis of strained silicon devices. In the following section, we report some results of a simulative study which we carried out on the electromagnetic properties of the nanofabricated strained SOI waveguides; in particular we have estimated the effective refractive index, effective refractive group index, modal intensity distribution and birefringence of the strained SOI waveguide basing our analysis on the validated FEM-based model.

In such analysis we have employed a multiphysical simulative model, described in Chapter 2, in order to evaluate the effects which the crystalline deformation induces on the optical properties of the silicon nanometric devices. In particular, the validated FEM model has been used to estimate the strain and stress distribution across the section of the SOI waveguide using the geometries of the manufactured devices, which are inferred through the SEM analysis of the structures. The variation of the impermeability tensor, due to the photoelastic effect, is estimated through the theoretical model described in section 2.4 and the electromagnetic properties in the strained SOI waveguide are evaluated through the FEM-based numerical model described in section 2.6.

As discussed above, the geometries employed in the multi-physical simulative estimations have been extrapolated through the analysis of SEM images of the SOI waveguides, see for example Fig. 4.25. The SEM analysis shows that the manufactured waveguide is 482 nm wide and 220 nm high and that the thickness values of the deposited silicon nitride layer is 325 nm for the cladding layer on the silicon substrate and 440 nm for the part covering the waveguide. The simulative estimations of the TE mode intensity distribution for the strained SOI waveguide, with the inferred geometry, is reported in Fig. 5.9 for wavelength $\lambda = 1.55\ \mu m$.

Fig. 5.9 shows that a large amount of TE mode radiation is confined in the silicon nanowire despite the presence of the high refractive index silicon nitride film ($n_{Si_3N_4} \sim 2$). The high index-contrast between Si and SiO_2 and between Si ans Si_3N_4 leads most of the modal intensity to be impounded in the silicon structure. Since most of the optical power carried by the mode is confined in the center of the silicon nanowire, the interaction between the radiation and the vertical sidewall roughness is expected to be weak. As described in Chapter 2, due to the nature of the lithography fabrication processes, roughness on the vertical sidewalls of the waveguide is unavoidable and generates light scattering that is considered the strongest effect of propagation loss. The small amount of electromagnetic power at the vertical sidewall suggest that the manufactured strained SOI waveguide should be weakly effected by manufacturing non ide-

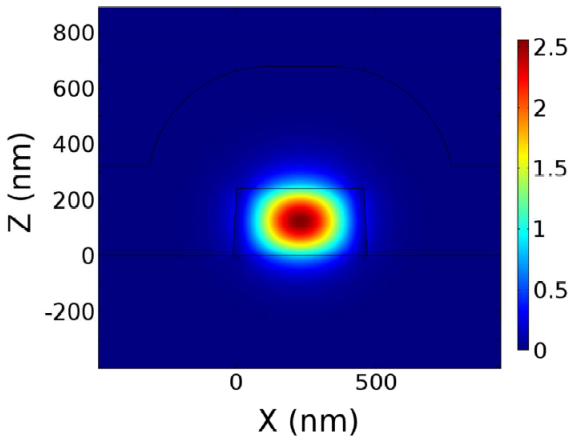

Figure 5.9: Simulation of TE-mode power distribution on the plane perpendicular to propagation direction for the manufactured SOI waveguides. The intensity is expressed in arbitrary units.

alities and are expected to show low scattering-induced propagation losses. At the same time, the simulative estimations show that SOI waveguides with the observed geometry operate in single mode regime for $\lambda = 1.55\ \mu m$: no other guided modes are obtained in the range of wavelengths $1545 - 1555\ nm$. These results show that manufactured geometries allow good modal confinement, small interaction of the radiation with surface roughness and single mode condition and can therefore be employed in low-loss single mode SOI waveguides.

Fig. 5.10 reports the obtained dispersion curves for the stress-free SOI waveguides TE mode and strained SOI waveguide TE mode, in the wavelength range of $1545 - 1555\ nm$.

The results show that the presence of the high intrinsic stress film affects the electromagnetic properties of the SOI waveguide, as expected. The mode effective refractive index and effective group index values of the strained SOI waveguide show a variation of about +0.005 and +0.009, respectively, with regard to the stress-free structures. On the other hand, the obtained behaviors are not altered by the presence of the lattice deformation: effective group index values are approximately constant in the considered range while the effective refractive index decreases as a linear function of the wavelength, for both strained and unstrained structures. Furthermore, the high values which we have obtained for the effective refractive index show that the radiation mode is well confined, assuming the geometry observed in the manufactured waveguides, and that the radiation is far from the cut-off condition, confirming the results of the modal intensity distribution analysis. Such results show that, despite the interaction between the optical field and the strain fields affects the elecotromagnetic properties of the manufactured waveguides, no impairments on the guiding properties are expected.

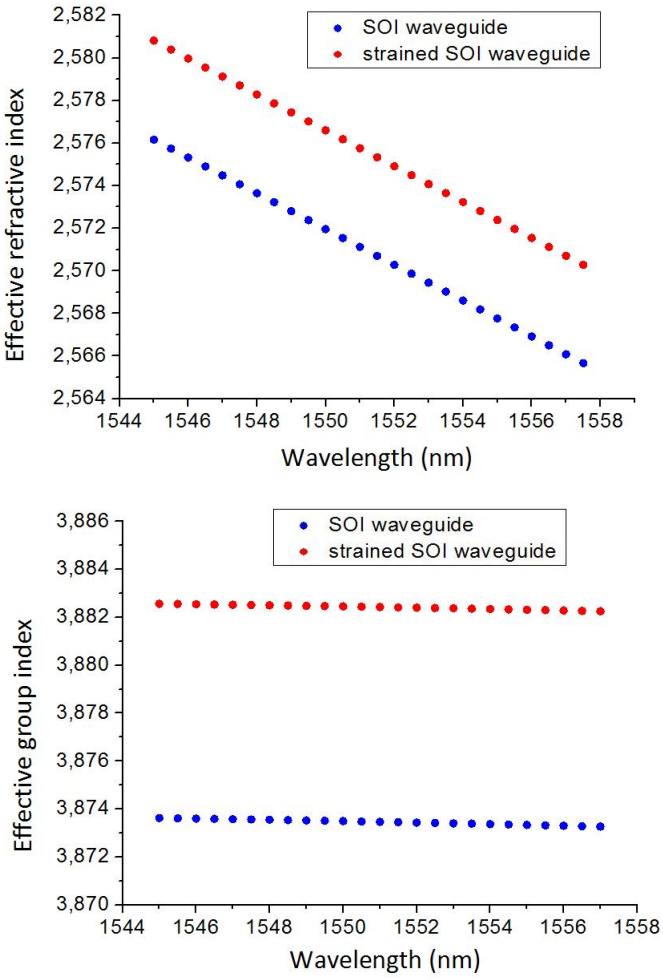

Figure 5.10: Estimated effective refractive index and effective group index of the manufactured SOI waveguides.

The multyphyisical model described above has been employed to evaluate the optical anisotropy of the strained SOI waveguide through the estimation of the induced birefringence. In particular, the refractive index $n_x$and n_z for the TE and TM polarization, i.e. the radiation with polarization vector oriented in the horizontal and vertical direction, are estimated and theirs difference, said birefringence, $n_x - n_y$, is averaged across the section of the silicon core. In order to assess the impact of the experimental nanofabrication parameters as well as the amount of induced strain on the optical properties of the waveguides, different values of thickness for the silicon nitride film have been considered. The results, reported in Fig. 5.11, show that the birefringence values increase with the growing of silicon nitride thickness values, as expected. While for low thickness, the amount of silicon nitride is not enough to induce an appreciable crystalline deformation in the silicon nanowire, with the growing of the Si_3N_4 amount deposited, the stress in the layer tend to deform and bend more and more the wafer until a steady state is reached at witch the $Si - N$ bonds at the interface are not effected anymore by the deposition of other layers. For the range of values of SiN thickness that we have analyzed ($<$400 nm), a neat saturation has not been achieved yet; this suggests that the thickness can be increased up to values grater to0.5 um to induce grater values of birefringence. On the other hand, thickness values greater than 450 nm, due to the high intrinsic stress, would bring to tensions which could excessively bend the wafer and induced cracks or delaminations. For thickness values around 400 nm, the obtained mean birefringence is 0.014. It's worth noting the lithium niobate ($LiNbO_3$), commonly employed in modulator devices, shows values of birefringence of the same order of magnitude: for wavelength around 1550 nm the birefringence is about $0.08 - 0.09$. The simulative estimations show that the deformation induced by the presence of the high intrinsic stress SiN is capable of effectively modifying the optical properties of the SOI waveguide and to induce significant values of mean birefringence on the silicon nanowire.

5.3 Measurements of propagation loss of the nanofabricated strained SOI waveguides

5.3.1 Fabry-Perot resonance method

The optical performance of the manufactured strained SOI waveguides has been evaluated through an experimental analysis of the propagation loss of such devices. The aim of these measurements is to estimate the quality of the CMOS nanofabrication processes which have been employed for the manufacturing of the SOI waveguides as well as to assess the possible use of the innovative Spacer Patterning Method technique for the realization of photonic devices. Furthermore, since SPM technique has never been employed for the manufacturing of strained silicon devices, these results can provide useful information on the compatibility of such nanofabrication processes with the strained silicon technology. The propagation losses of the manufactured SOI waveguides have been

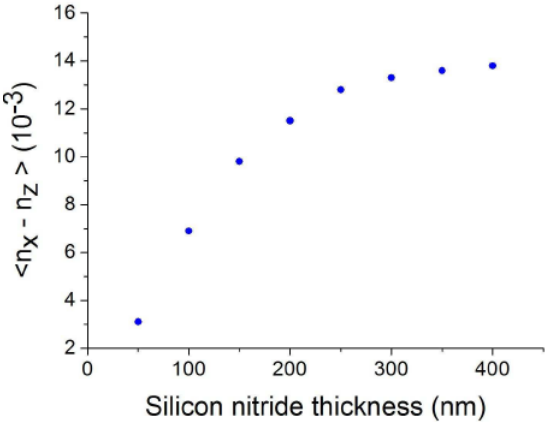

Figure 5.11: Estimated mean birefringence of the nanofabricated SOI waveguide as a function of silicon nitride thickness.

performed through the employment of the Fabry-Perot (FP) resonance method.

The (FP) resonance method is one of the most commonly employed experimental techniques for propagation loss measurements of SOI devices: this technique exploits the resonant cavity constituted by the optical waveguide with polished facets for extracting information on the loss suffered by the radiation [85]. The propagating light is reflected at either facets by an amount which is determined by refractive index contrast between the waveguide and the cladding layer or air and undergoes several reflections along the path. The structure can therefore be regarded as a Fabry-Perot resonator with the optical intensity transmission I_t , normalized to the incident light intensity I_i, given by:

$$\frac{I_t}{I_i} = \frac{(1-R^2)e^{-\alpha L}}{((1-Re^{-\alpha L})^2 + 4Re^{-\alpha L}sin^2(\phi/2)} \tag{5.1}$$

where R is the reflectivity at the facet, L is the waveguide length and ϕ is the phase difference between successive radiations. The coefficient α is the loss suffered by the radiation and has the dimensions of $[cm^{-1}]$. The ratio between the maximum I_{max} and minimum value I_{min} of Eq. (5.1), corresponding to wavelengths with $\phi = 0$ and $\phi = \Pi$ respectively, is given by:

$$\zeta = \frac{I_{max}}{I_{min}} = \frac{(1+Re^{-\alpha L})^2}{(1-Re^{-\alpha L})^2} \tag{5.2}$$

Rearranging Eq. (5.2) it is possible to extract the loss coefficient α :

$$\alpha = -\frac{1}{L} ln(\frac{1}{R}\frac{\sqrt{\zeta}-1}{\sqrt{\zeta}+1}) \tag{5.3}$$

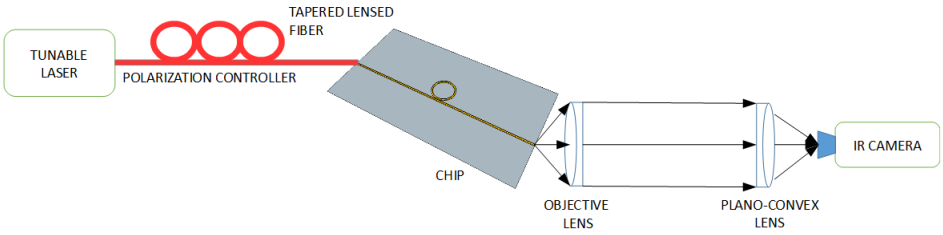

Figure 5.12: Experimental set-up for the propagation loss measurements.

Eq. (5.3) shows that the loss coefficient loss α can be evaluated simply measuring the ratio of the maximum intensity to minimum intensity ζ . It's clear from Eq. (5.3) that, under the assumption that the coupling efficiency is not dependent on the radiation wavelength, propagation loss measurement is not affected by the coupling loss and can be easily evaluated starting from the transmission spectrum of the waveguide.

5.3.2 Results of the propagation loss measurements

Fig. 5.12 shows the experimental set-up that we employed for the loss measurement of the singlemode strained SOI waveguides. The radiation is generated by a tunable laser source sweeping frequencies in the C-band. The field passes through a polarization controller and a polarizer in order to control the ratio of TE and TM modes power excited in the waveguide and is injected into the chip containing the waveguides through a polarization single mode tapered lensed fiber. This type of fiber, with regard to cleaved standard single mode fibers, improves the coupling efficiency and the mode matching between the fiber mode and the waveguide mode. In particular, due to its laser shaped tapered lensed end, the fiber shrinks the dimensions of the traveling radiation in correspondence of the final tip and focuses it at distance of few microns. The lensed fiber employed in this set-up have a nominal spot size of less than 2 μm. The light injected in the waveguide is collected at the end facet through a 20$\times$ magnification objective lens. Due to the micrometric precision required by the coupling between the fiber and the waveguide and the alignment between the waveguide and the lens, 3 axis stages with micrometric precision control have been employed for the movement of fiber lens and lens, while 2 axis and rotating stage have been used for the sample. The collimated ligth passes through an iris in order for spurious light not to be collected and is then focused by a plano-convex lens at IR camera recording the intensity distribution of the radiation.

Fig. 5.13 shows an image, taken at the IR camera, of the radiation collected by the objective lens at the endface of a manufactured waveguide.

A spot light is clearly visible in the center of the figure: it corresponds to the light exiting the endface of the SOI waveguide. The dimensions of the bright point match those of the nanometric silicon core, i.e (482×220) nm, with a 20$\times$

Figure 5.13: Infrared image of the collected at the endface of the waveguide.

magnification due to lens system used in the setup. The tunable laser light has been efficiently injected in the waveguide through the butt-coupling technique and confined in the sub-wavelength silicon nanowire that directs the radiation toward the endface of the sample. Other small bright points can be observed at the same height of the waveguide. Their presence is due to spurious light which is scattered by the other silicon structures of the chip or dirt at the boarder of the sample. Such spurious light is due to radiation that has not been collected by the waveguide due to the modal mismatch between the silicon core and the injected light and to light that is scattered out of the waveguide through surface roughness. The silicon nitride straining layer acts a slab waveguides confining the spurious light in vertical direction and directing toward the endface of the sample. The scattered light is therefore directed toward the camera giving rise to the observed blurry point. The different brightness between the waveguide and the scattering elements show that a significant amount of the injected power has been collected in the device and efficiently directed to the endface of the sample.

The graphs reported in Fig. 5.13 and Fig. 5.14 show the obtained transmission spectra, expressed in arbitrary unit, for one of the manufactured strained SOI waveguide. The spectra have been recorded at the IR camera at two wavelength intervals, namely at$1545 - 1547\ nm$ range and at$1555 - 1557\ nm$ range. The graphs show quite sharp peaks arranged in pattern similar to a typical Fabry Perot resonator transmittance spectrum. The quality of the waveguide facets is high enough to induce a significant part of the power carried by the mode radiation to be reflected feeding a feedback resonance mechanism. The peak-to-peak amplitude is approximately constant over the frequency range while an overall increase of the mean intensity is observed for longer wavelengths. This phenomenon is probably induced by the mechanical drift on the micropositioners or to the polarization instability of the laser along the interval of frequency. The distance separating the peaks is approximately constant across all the wavelength range: the observed free spectral range (FSR) is 60 pm and is in accordance with the theoretical FSR of the resonance cavity given by $\lambda^2/n_g L \simeq 62\,pm$ where L is the resonator cavity length and $n_g$is group index of the SOI waveguide.

The propagation loss values for the singlemode strained SOI waveguide have

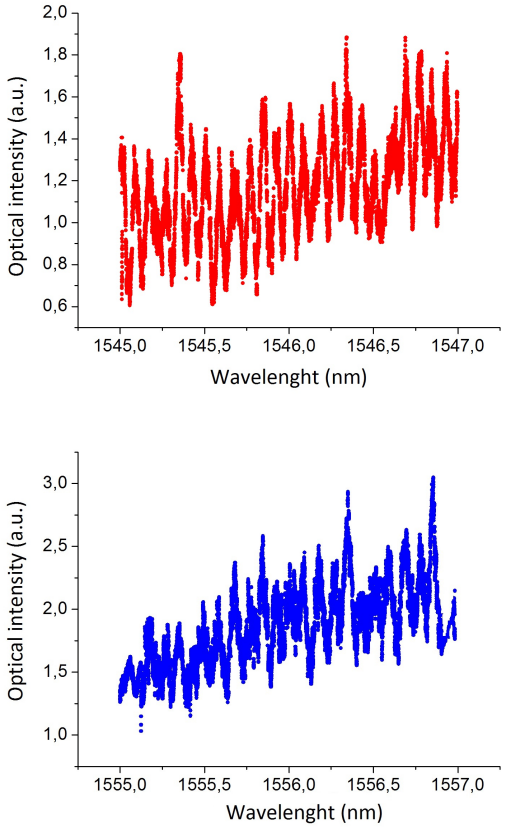

Figure 5.14: Fabry-Perot scan of the manufactured singlemode SOI waveguide for the wavelength interval $1545 - 1547\ nm$ (up) and $1555 - 1557\ nm$ (down).

been evaluated using the data extracted from the intensity spectrum reported in Fig. 5.14. In particular, the maximum and minimum values for different peaks have been recorded and the averaged value of the ζ ratio is fed into Eq. (5.2) and Eq. (5.3). The facet reflectivity R used in Eq. (5.2) is assumed to be 0.31 corresponding to a Fresnel silicon/air interface reflection coefficient. The propagation loss values obtained are $\alpha = 5.8 \pm 0.8\, dB/cm$ for the range $1545 - 1547\ nm$ and $\alpha = 8.8 \pm 0.8\, dB/cm$ for the range $1555 - 1557\ nm$.

The obtained loss values are comparable with those of the state-of-the-art SOI waveguides, around $2 - 3\ dB/cm$, which are commonly fabricated with the $193nm$ optical lithography or electron beam lithography, as described in Chapter 2. Furthermore, the Fabry Perot resonance method can overestimate the loss coefficient values since it assumes perfectly flat waveguide facets. In fact, in our case, the waveguide facets have undergone a lapping process that could reduce the quality of the facets. This procedure consists of a polishing of the sample facets with abrasive materials with sequentially decreasing grit sizes and can induce a certain amount of roughness and a slight curvature on the end facet, not present in the ideally flat surfaces assumed in the FB method. As a result, the reflectivity values of the facets are reduced and the propagation losses are overestimated. The commonly employed procedure for the facet preparation, the cleavin, is carried by mechanically introducing a small crack at the edge of the sample, in the orthogonal plane to the direction of propagation, and applying a pressure so that it craks along a primary crystal plane. This technique allows to allow an high degree of flatness and a very high reclectivity. Unfortunately, this technique could not be employed in the manufactured waveguides due to the presence of the silicon nitride film that would induce serious damages to the sample.

At the light of these considerations, the obtained propagation loss values prove the high quality of the nanofabrication processes employed and in particular the accuracy of the innovative SPM technique. The SPM technique allowed to realize the expected geometries employable in high-performance photonic devices. The etching processes has successfully defined the silicon nanowires with a low RMS surface roughness as shown by the low loss values obtained. Furthermore, the deposition of the high intrinsic stress silicon nitride film has not impaired the guiding properties of the devices showing the compatiblity of the strained silicon technology with the SPM technique. W therefore believe that the SPM nanofabrication technique can be fruitfully employed for the manufacturing of strained high-performance SOI devices employing strained silicon technology and that can represent a low-cost and high yield alternative solution to EBL (Electron Beam Lithography) of DUV (Lased Deep Ultraviolet) lithography.

Chapter 6

Ultra compact OAM beam emitters based on angular gratings

The optical orbital angular momentum (OAM) is a degree of freedom of the photon in addition to the polarization/spin. After the demonstration that physically realizable beams with intensity distributions $u(r, \phi, z) = u_o(r, z)exp(i\phi l)$ carry a well defined OAM about the axis, OAM beams have been employed in different fields for various applications. In particular, light-carrying orbital angular momentum (OAM) has been recently shown to have the potential for efficiently enhancing the information channel capacity in both classical and quantum optical communications. Lately, integrated optical devices for the generation and manipulations of OAM carrying beams have been proposed and employed in experimental communication links. These devices promise to address the demand for switching speed between OAM modes and routing flexibility, essential for an efficient OAM-based communications systems. In this Chapter, we report the results of an experimental study on ultracompact OAM beam emitters based on angular grating with two different geometries: emitters based on microring resonators and omega-shaped emitters. The analyzed devices are based on silicon photonics technology and can be employed in communications the require fast switching of OAM modes, multi-wavelength and multi-OAM state emission.

In the first section of this Chapter a brief review of the story of the orbital angular momentum of light and its applications in communication systems is reported. In section 2 we describe the properties of OAM beams and the demodulation technique used in the experimental analysis. In section 3 we analyze the properties of the OAM devices under study and the physical principles underlying the emission of light carrying well defined OAM by the embedded angular gratings. The results of the experimental analysis on the radiation efficiency of OAM emitters based on microring geometry are discussed in section 4 and the analysis of the OAM beams emitted by the omega-shaped multiplexers is

reported in section 5.

6.1 History of Orbital Angular Momentum of Light and its applications

6.1.1 History of Orbital Angular Momentum of Light

The hypothesis that light should have mechanical properties dates back to the sixteenth century, since Kepler suggested that the comet tails were due to radiation pressure associated with sun light [93]. After the development of Maxwell's unified theory of electricity, magnetism and optics, light radiation pressure could be quantitatively studied but no detailed analysis were carried out on the mechanical properties of light [94]. It was Poynting who quantified the energy flux of an electromagnetic radiation and its linear momentum density [95]: in modern terms the energy flux, called the Poyinting vector, can be expressed as $\mathbf{S} = \mathbf{E} \times \mathbf{H}$ and the linear momentum per unit volume $\mathbf{g}$ is: $\mathbf{g} = (\mathbf{E} \times \mathbf{H})/c^2$ [96]. The angular momentum density $\mathbf{L}$ can be therefore expressed as $\mathbf{L} = \mathbf{r} \times (\mathbf{E} \times \mathbf{H})/c^2$.

Few years later, Poynting [97] suggested that a circularly polarized (CP) light carries an angular momentum (AM) basing his analysis on the analogy with the wave motion associated with a line of dots marked on a rotating cylindrical shaft. In his theoretical work, Poynting demonstrates that the CP light carries an angular momentum per unit of area and time of $E\lambda/2\Pi$ where E is the energy density per unit volume and λ is the wavelength. In order to detect the AM associated with the radiation, he proposed to pass the CP light through a suspending quarter-wave plates and measure the rotational movement induced by the AM transfer. In 1936 Beth [98] carried out Poyinting idea and measured the torque exerted by CP light impinging into single quarter wave plate providing, for the first time, evidences of the AM possessed by the light. The state of polarization (SOP) does not take into account the total orbital momentum carried by a radiation: beside the polarization contribute, known as spin angular momentum (SAM), another contribute is associated with the azimuthal phase distribution of light. This part is said orbital angular momentum (OAM).

The modern study of AM of light, and particularly of the OAM contribute, is considered to have started with the paper of Allen at al [99]. In this work, the authors demonstrated that any beam with the amplitude distribution in the form $u(r, \phi, z) = u_o(r, z)exp(i\phi l)$, where l is integer-valued, carries a well defined angular momentum about the beam axis. Furthermore, the OAM contribute is uniquely determined by the azimuthal phase distribution and assumes quantized values equal to $l\hbar$ per photon with l the azimuthal mode index. The authors highlight that the Laguerre-Gaussian modes, solutions to scalar paraxial Helmoltz equation, represent a physically realizable example of well-defined OAM beams since they are natural modes of cylindrically symmetric resonators. Since the publication of this work, other types of beams have been demonstrated to have well defined orbital angular momentum as, for example, cylindrical vector (CV) beams [100]and (HOB) order Bessel beam [101]. Higher order Bessel

beams are solutions of the exact Helmoltz equation and have a radial dependence on the form of Bessel function of the first kind. HOB are diffraction free solutions: the intensity distribution maintain their shape with no scaling factor during the propagation differently than LG beam. The second type is a solution to vectorial paraxial Helmoltz equations and are characterized by a cylindrically symmetric space distribution of the state of polarization (SOP). A section of this Chapter is devoted to the description of CV beams.

6.1.2 OAM communications

Light-carrying orbital angular momentum (OAM) has found many applications in several areas of science and technology. Some examples are represented by optical manipulation and trapping in optical tweezers, high-precision optical measurements, studies of fundamental quantum physics, high-capacity free-space and fiber-optic communications. In particular, the employment of OAM of light in communication has proved to have the potential for significantly enhancing the information channel capacity of the systems in both classical and quantum domains. In communication systems the optical OAM has been mainly exploited in 2 ways: in the first one the information is encoded as OAM states while in the second one beams with different OAM orders are used as information carriers for multiplexing schemes. In the next section we report a brief review of the experimental realizations of OAM-based free space communication which implement these two schemes.

In the last decade, many experimental demonstrations of free-space OAM-based optical communications have been reported. Initially, the OAM order was exploited as a new degree of freedom for modulation schemes of the signal. Traditional links rely on modulation of intensity, frequency, or polarisation of the radiation. The OAM of light, with a theoretically infinite number of possible values of the OAM states l, can be used to encode an alphabet with an infinite number of "letters". In 2004 Gibson at al. [102] demonstrated the transfer of information encoded as OAM states of infrared light with a good level of eavesdropping resistance. Spatial light modulators were employed for both transmitting and receiving OAM beams in a 15 m long free-space communication based on 8 OAM orders alphabet. Since then, communications encoded as OAM orders up to several Gb/s in free-space under strong atmospheric turbolence, in deep-space and near earth communication[103][104]. Moreover, OAM based comunication has been demonstrated for free-space radio data link[105]. OAM beams have also been employed in quantum key distribution schemes: Malik in [106], reports a free-space 11-dimensional communication system using OAM modes with a maximum measured channel capacity of 2.12 bits/photon.

In addition to OAM modulation, mutliplexing schemes based on different OAM orders have been studied. As will be discussed in the following section, beams with different OAM orders l are orthogonal with each other. This property enables multiple beams of different OAM values to be multiplexed and demultiplexed with no crosstalk between them. OAM order represents therefore a further degree of freedom added to the traditional envisioned switch-

ing domains (space, wavelength, and time) that could be employed in multiplexing schemes for the enhancement of the capacity of the channel. In fact, since each OAM beam can carry an independent data stream, the total capacity of link that transfers multiple spatially overlapped beams, equals the data rate of a single channel multiplied by the number of the beams. Multiplexing schemes for OAM based communications have been recently demonstrated. In 2010 Awaji et al. [107]demonstrates, for the first time, a free-space optical OAM communication employing multiplexed Laguerre-Gaussian beams. In their work, the authors report error-freely propagation of multiplexed LG pulses at 10Gbit/s in telecommunication wavelength (C-band) and their demultiplexing. Subsequently, other groups have demonstrated the compatibility of OAM multiplexing with other conventional multiplexing schemes. Wang [108]at al. demonstrated a communication based on both polarization and OAM multiplexing schemes with a capacity of $2.56\,Tbits^{-1}$ and spectral efficiency of $95.7\,bits^{-1}Hz^{-1}$. The authors also reported data exchange between orbital angular momentum beams encoded with 100 $Gbit/s$ differential quadrature phase-shift keying signals. Huang [109]demonstrates a free-space data link combining OAM-, polarization-, and wavelength-division multiplexing. In particular, the authors report the multiplexing/demultiplexing of 1008 data channels carried on 12 OAM beams, 2 polarizations, and 42 wavelengths with each channel encoding 100 Gbit/s quadrature phase-shift keying data, providing an aggregate capacity of 100.8 Tbit/s.

6.1.3 Generation of beams carrying OAM

In the majority of the summoned experiments, the OAM beams are generated using free-space optical components. In [102] the transmitter unit consisted of a HeNe laser, a telescope and a computer-controlled phase hologram generated through the employment of a reflective spatial light modulator. In [110] helical modes of visible light are generated through q-plates exploiting patterned liquid crystal technology. In [111]Laguerre-Gaussian and vortex orbital-angular-momentum modes are generated using digital micro-mirror devices (DMD), which are amplitude-only spatial modulator consisting of a series of micro-mirrors with electronically controllable deflection angle. The use of such bulk components is not suitable for optical communication due to large size of the devices and the the slow switching speed between the OAM modes which is limited to a few kHz [112].

In the last few years, several groups have demonstrated integrated optical devices, wich have been micofabricated using the mature and reliable CMOS-compatible processes, capable of generating and manipulating OAM beams. These devices can be employed in highly efficient OAM data channels and routing links due to their compactness, robustness and fast tunability. Doerr at al. in [113] demonstrated a silicon PIC employing a circular grating coupler for generating and receiving focused azimuthally and radially polarized beams. Su et al. in [114] exploits tunable-phase arrayed waveguides with vertical grating couplers to achieve space division OAM multiplexing and demultiplexing. Cai

et al. [115]demonstrated ultracompact silicon-integrated optical vortex emitters based on angular gratings capable of extracting light, which is confined in whispering gallery modes of the resonant cavity, into free-space high OAM beams. These devices are ultracompact: the smallest device has radius of 3.9 μm. In this work OAM emitters based on suc geometry are investigated.

6.2 Theory of OAM beams

In this section, we analyze the properties of beams carrying a well defined OAM, in terms of amplitude and phase distribution for the case of Laguerre Gaussian (LG) beams. LG beams represent a well understood example of physically realizable beams carrying OAM and their properties are valid for most of the optical vortex. Then, the working principles of the demodulation technique used in the experimental analysis of the omega-shaped devices are described. The employed technique is based on the phase-only modulation of the OAM beams that is imparted through a spatial light modulator. The effects of phase modulation on the OAM order of the beams together with the issues related to the conversion efficiency will be discussed for the simple case of helical-wavefront beams conversion produced with a spiral phase plate.

6.2.1 OAM of Laguerre Gaussian beams

The LG beams represent a well understood example of beams carrying a defined OAM. Most of their properties are common to all OAM beams and in particular to the cylindrical vectorial (CV) beams which are analyzed in this Chapter. The LG beams are a solution to the linear Helmholtz paraxial equation in cylindrical coordinates. A convenient representation of a linearly polarized LG beams in the Lorentz gauge, is given, using the vector potential $\mathbf{A}$ by:

$$\mathbf{A} = \mathbf{x} u_{pl}(r, \rho, \phi) \tag{6.1}$$

where $\mathbf{x}$ represents the unit vector in the direction of polarization and u_{pl} is the complex scalar function describing the intensity of the field:

$$u_{pl}(r, \rho, \phi) = \frac{C}{(1 + z^2/z_R^2)^{1/2}} \left[\frac{r\sqrt{2}}{w(z)}\right]^l L_p^l \left[\frac{2r^2}{w^2(z)}\right] \exp(-\frac{r^2}{w^2(z)}) \tag{6.2}$$

$$\exp(\frac{-ikr^2 z}{2(z^2 + z_R^2)}) \exp(-il\phi) \exp\left[i(2p + l + 1)\tan^{-1}(z/z_r)\right]$$

where C is a constant, $z_r$is the Rayleigh range, $w(z)$ is the radius of the beam, $L_p^l$is the associated Laguerre polinomial, and the beam waist is at $z = 0$. l and p are two integers and are said azimuthal order and radial order, respectively. As suggested by the name, LG beams can be separated in two

parts: one part describing the radial dependence of the intensity distribution in the form of Laguerre polinomials and a Guassian-like part describing the curvature of phase wavefront. It's worth noting that the the phase spacial dependence on the azimuthal coordinate ϕ is solely expressed by the exponential function $\exp(-il\phi)$.

The angular momentum density, defined by $M = \varepsilon_0 r \times < E \times B >$, is:

$$M = -\frac{l}{\omega}\frac{z}{r}|u|^2 r + \frac{r}{c}[\frac{z^2}{(z^2 + z_R^2)} - 1]|u|^2\phi + \frac{l}{\omega}|u|^2 z \tag{6.3}$$

The contribution of the radial and azimuthal components to the integration of M over the beam profile vanish due to their symmetry about the axis. Solely the z component of angular momentum density contributes to the total angular momentum. M is therefore only dependent on the azimuthal order l and on the wavelength ω and is directed along the propagation of direction z. Considering the ratio of the flux of angular momentum L to that of the energy E, one obtains the angular momentum per photon:

$$\frac{L}{E} = \frac{l}{\omega} \tag{6.4}$$

Since the energy associated to a photon is $E = h\omega$, the LG beams result to have a well defined and quantized orbital angular momentum per photon equal $l\hbar$, labeled by the azimuthal order l.

When the vector potential is generalized to arbitrary state of polarization, a contribute is added to the z component of the angular momentum M:

$$M_z = \frac{l}{\omega}|u|^2 + \frac{\sigma_z r}{2\omega}\frac{\partial|u|^2}{\partial r} \tag{6.5}$$

where $\sigma_z = \pm 1$ for left-handed and right-handed respectively and $\sigma_z = 0$ for linearly polarized radiation. The polarization dependent contribute to the z oriented angular momentum density is dependent upon the gradient of the intensity. The ratio of the angular momentum flux to energy, for arbitrary polarized LG beams, becomes:

$$\frac{L}{E} = \frac{(l + \sigma_z)}{\omega} \tag{6.6}$$

For LG beams, the contributes of OAM and SAM are separated and well defined. LG beams posses other important properties: they form a complete set of solutions to the paraxial Helmholtz equation; it implies that any other solution can be written as a superposition of these beams. Furthermore LG beams with different azimuthal order are orthogonal: no power is exchanged between each other along that propagate in free space.

It can be shown that the results obtained for LG beams and their properties in terms of OAM, are valid for any beam with a intensity distribution $u(r, \phi, z) = u_o(r, z)exp(i\phi l)$ and in particular for the CV beams wich we have analyzed in this experimental analysis.

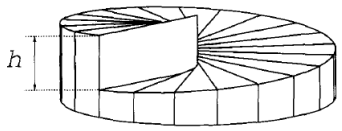

Figure 6.1: Schematic of the spiral phase plate, from [116].

6.2.2 OAM order transformation with spiral phaseplate

In the experimental measurements which we will describe in the following chapter, the demodulation of the OAM beams has been carried out through a phase-only modulation technique. A spatial light modulator (SLM), by imparting a particular phase change pattern to a impinging beam, transforms any OAM order l into $l = 0$ order; the efficiency of such transformation depends on the intensity distribution of the beam. The SLM emulates the behavior of the Spiral Phase Plate (SPP) used for the conversion of laser beam into helical-wavefront laser beams [116]. The working principles of the SPP conversion are also valid for the demodulation technique which we have employed in the reported experimental analysis and are discussed here.

The SPP is a transparent plate with a thickness proportional to the angle ϕ around the middle of the plate, see Fig 6.1. For small divergence beams and for height of the plate sufficiently small, the paraxial regime is maintained and the effect of the phase plate can be considered to affect solely the phase of the beam. The complex amplitude $u(\rho, \phi, z)$ of the beam after crossing the plate results is[116]:

$$u' = u(\rho, \phi, z) exp(-i\Delta l\phi) \tag{6.7}$$

whereΔl is the height of the step normalized to the wavelength λ given by:

$$\Delta l = \Delta n h/\lambda \tag{6.8}$$

Eq. (6.7) shows that the phaseplate imposes a spiral twist to the phase distribution of the beam but it doesn't affect its amplitude. The SPP may therefore transform a non-helical beam into a helical-one or change its helicity. Taking into account the relation, that we have described in the previous section, between the azimuthal phase distribution and orbital angular momentum of a beam, it's clear that the SPP alters the OAM order of a beam passing through. Nevertheless, in most cases, the resulting beam is no longer a pure mode anymore and can be represented as a superposition of pure modes. Again, it is useful to consider LG beams in order to better understand the behavior of a SPP.

The effect of the SPP on a LG beam can be expressed, in ket notation, by:

$$u^*_{nm} LG = \exp(-i\Delta l\phi)|u^{LG}_{nm}> \tag{6.9}$$

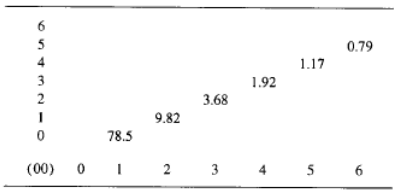

Figure 6.2: Mode contents of a LG_{00} beam that has acquired the phase shift due to $\Delta l = 1$ spiral phaseplate. The index s in on the horizontal axis and the index t is in the vertical axis, from[116].

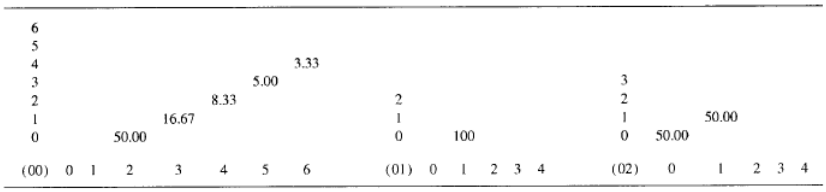

Figure 6.3: Mode contents of a LG_{00},$LG_{01}$and LG_{02} that has acquired the phase shift due to $\Delta l = 2$ spiral phaseplate, from[116].

where the new indices n and m are defined by $p = min(n, m)$ and $l = n - m$, where p and l are the indices used in Eq. (6.2). Employing the LG beams as a complete set of modes, with Rayleigh range and the coordinate of the waist equal to those of the incident beam, it is possible to express the beam of Eq. (6.9) as a superposition of modes with expansion coefficients $a_{mn,st}$ given by:

$$a_{nm,st} =< u_{st}^{LG} | \exp(-i\Delta l\phi) | u_{st}^{LG} > \tag{6.10}$$

where $< | >$ denotes the integration in the transverse plane. The integral is non null for s and t satisfying the following equation:

$$s - t = n - m + \Delta l \tag{6.11}$$

In the tables of Fig. 6.2 and Fig. 6.3, we report the numerical estimations of the coefficients $a_{nm,st}$ for a LG_{00}beam passed through a $\Delta l = 1$ phase plate and for LG_{00}, $LG_{01}$and LG_{02}beams passed through$\Delta l = 2$ phase plates, from [116].

The values reported, demonstrate that most of the power of the incoming beam LG_{00} , about 78, is carried by $LG_{0,1}$mode but more than 20 ends up in other orders. The values of table in Fig 6.3 show that, generally, the transfer of power from one mode to another is not complete, except the case:

$$\Delta l = -2(n - m) \tag{6.12}$$

In these transformations, the conversion is complete since the incoming beam and the considered one have the same intensity but inverted phase. In the other

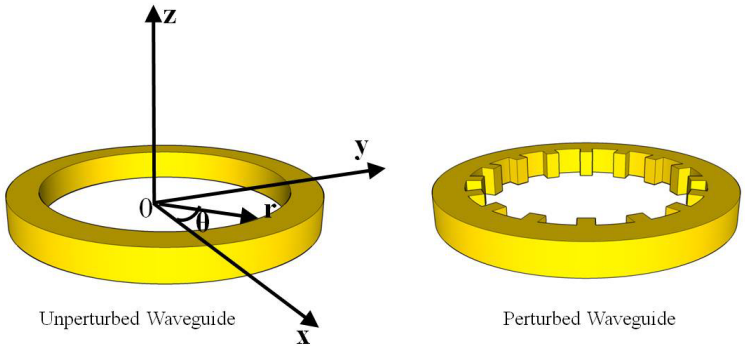

Figure 6.4: Layout of a microring (left) and of OAM beam emitters based on angular gratings (right), from [115].

cases, the mismatch between the intensity pattern forbids a complete transfer of power from one mode to another: the spiral phase plate is not in general a pure mode converter. Furthermore, the purity of the converted mode reduces for high OAM order l since the phase and amplitude distribution of the transformed mode give rise to low values of overlap integral with the pure beam.

These consideration for the SPP plate transformation on LG beam can be applied to the demodulation technique employed in the experimental analysis where the phase modulation is imparted through a SLM. The phase pattern used for the demodulation has, indeed, the same azimuthal dependence of the one imparted by the spiral phase plate. The details on the demodulation procedure employed are provided in the section 5.

6.3 Ultra compact OAM beam emitters based on angular gratings

6.3.1 Coupled mode theory (CMT) analysis of angular sidewall gratings

In the experimental analysis reported in this work, two types of integrated OAM beam emitters have been studied. The first type are micrometer-sized SOI ring resonators embedding second order angular gratings. In such devices, the grating is patterned in the inner vertical sidewalls of the ring and allow to extract the resonant confined light imparting well defined phase distribution and polarization state to the radiated beam. The OAM order of the emitted beam is determined solely by the periodicity of the grating and the wavelength of the radiation. The working principles of the OAM emitters as well as the properties of the radiated beam can be described through a Coupled Mode Theory (CMT) based analysis.

It's well known that the presence of a perturbation, in the cross-section of a waveguide, induces coupling between the eigenmodes of the unperturbed waveguide. In the OAM emitters, the embedded gratings can be considered as a periodic perturbation that coherently couples the guided mode of the microring resonators with the radiative modes generating a radiated beam with well defined optical properties. In the cylindrical coordinate system (r, z, θ), defined in Fig. 6.4, the electric field of the perturbed waveguide, can be expressed as a linear combination of the unperturbed eigen-modes of the structure[115]:

$$\mathbf{E} = \sum A_m(\theta)\mathbf{E}_m(r,z)\,\exp(i\omega t - \nu_m(\theta)) \tag{6.13}$$

where $A_m(\theta)$ are the coefficients of the guided and radiative modes propagating in θ direction, $E_m(r,z)$ is the transverse mode profile, and $\nu_m = \beta_m R$ is the angular propagation constant for a ring with radius R.

The dielectric constant, as a function of space, can be written as:

$$\varepsilon(r,z,\theta) = \varepsilon_u(r,z) + \triangle\varepsilon(r,z,\theta) \tag{6.14}$$

where ε_u is the unperturbed part of the dielectric constant, and $\triangle\varepsilon(r,z,\theta)$ is the perturbed dielectric constant which is periodic in θ direction.

Assuming the slowly varying amplitude (SVA) approximation, the evolution of coefficients $A_s(\theta)$ can be shown to determined by the following relation:

$$\langle s|s\rangle \frac{dA_s}{d\theta} = \frac{\omega^2\mu}{2i\nu_s} \sum_n \left\langle s|\Delta\varepsilon(r,z,\theta)\, r^2|n\right\rangle A_n \exp(\pm(i(\nu_s - \nu_n)) \tag{6.15}$$

where

$$\langle s|s\rangle = \int \mathbf{E}_s^*(r,z)\mathbf{E}_s(r,z)drdz \tag{6.16}$$

$$\left\langle s|\Delta\varepsilon(r,z,\theta)\, r^2|n\right\rangle = \int \mathbf{E}_s^*(r,z)\Delta\varepsilon(r,z,\theta)r^2\mathbf{E}_n(r,z)drdz \tag{6.17}$$

The RHS of Eq (6.17), said overlap integral of the modes, represents the coupling strength between the 2 eigen-modes mediated by the perturbation.

A general consideration can be made on the expected state of polarization of the scattered radiation. In SOI waveguides, strong electric fields polarized in the propagation (azimuthal) direction, E_{az}, are present due to tight confinement. Their maxima are located at the vertical sidewalls of the waveguide in correspondence of the scattering elements (see Fig. 6.5). It's clear that in order for the overlap integral not to be negligible and consequently the transfer of power to be efficient, it is necessary that the polarization of the radiation mode must be parallel to that of the guided mode in correspondence of the dielectric perturbation. At the light of these considerations, the radiation excited by a quasi transverse-electric mode TE is expected to be mainly longitudinally polarized. The effects on the state of polarization of the radiated beam steaming from the constructive interference of the radiation of the singular diffractive element will be discussed later.

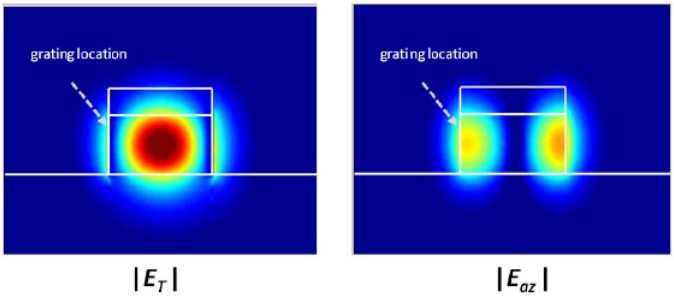

Figure 6.5: Simulated field distribution of azimuthal electric field E_{az} and transverse electric field E_T for quasi-TE WGM mode in silicon bend waveguide at 1550 nm, from [115].

The perturbation of the dielectric constant $\Delta\varepsilon$, i.e. the grating, is periodic in the angular direction θ and can be expressed as a Fourier series:

$$\Delta\varepsilon(r,z,\theta) = \sum_g \varepsilon_g(r,z)\exp(igq\theta) \tag{6.18}$$

where g is an integer and $q = 2\Pi R/\Lambda$ represents the number of scattering elements. Substituting Eq. (6.18) in Eq. (6.17), we obtain:

$$\langle s|s\rangle \frac{dA_s}{d\theta} = \frac{\omega^2\mu}{2i\nu_s}\sum_n \left\langle s|\varepsilon_g(r,z)\, r^2|n\right\rangle A_n \exp(i(\nu_s - \nu_n + gq)\theta) \tag{6.19}$$

Integrating Eq. (6.19) over an arc longer than the grating period and shorter than the variation scale of the amplitude, one obtains the increment of the sth field amplitude A_s , due to the mode coupling and mediated by the g component of the dielectric perturbation:

$$\Delta A_s(\theta) = \frac{\omega^2\mu}{2i\nu_s}\sum_n \left\langle s|\varepsilon_g(r,z)\, r^2|n\right\rangle A_n \int^{\theta} \exp(i(\nu_s - \nu_n + gq)\theta')d\theta' \tag{6.20}$$

The integral does not equal zero, and consequently the radiation is coherently scattered by the diffraction elements so that a significant amount of power is transferred to the radiated beam, only if the exponent is zero:

$$\nu_s - \nu_n + gq = 0 \quad g = \pm 1, \pm 2, \pm 3 \ldots \tag{6.21}$$

The Eq. (6.21) is said angular phase matching condition for the diffraction order g.

When the phase matching condition is satisfied, power from of the mode s can be transferred to a mode n with an efficiency determined by the overlap

integral: $\langle s|\varepsilon_g(r,z)\, r^2|n\rangle\, A_n$. Theoretically, a large number of modes can be coupled as long as their propagation constants match with a Fourier component of the grating. Nevertheless, the possible values of g are limited by the materials used in the system. Firstly of all the frequencies ν are tied to the propagation constant β through the relation: $\beta = \nu/R$ and $\beta_n = \beta_{wg} = \nu_{wg}/R = 2\Pi/\lambda n_{eff}$. Than $|\beta_s| = |\beta_{rad}| = |\nu_s/R| \leq 2\Pi/\lambda$ since the radiation mode propagates in vacuum.

These requirements impose a condition on the pitch given by:

$$(n_{eff} - 1)\frac{\Lambda}{\lambda} < g < (n_{eff} + 1)\frac{\Lambda}{\lambda} \tag{6.22}$$

For TE mode in SOI waveguide n_{eff} is around 2.5, λ is around 1550 nm and Λ is around 650 nm since this period corresponds to a second order grating. The only possible value for g is 1. Therefore, Eq. (6.21) can be rewritten as:

$$\nu_{rad} = p - q \tag{6.23}$$

where $p = \nu_{wg}$. Since the guided mode is a resonant mode of the ring, ν_{wg} has is integer valued and represents the number of times the wavelength of the light fits the optical length of the ring. ν_{rad} represents the angular velocity of the vortex emerging from the emitters and, in accordance with the considerations of the previous section, the OAM order l of the generated beam. Since both p and q are integer values, the OAM order l is integer as well and Eq. (6.23) can be rewritten as:

$$l = p - q \tag{6.24}$$

Eq. (6.24) shows that the OAM order of the emitted beam depends only on the resonant order p of the wavelength circulating in the microring and the number of scattering elements q of the embedded second order grating.

6.3.2 State of polarization of the radiated beam

As described above, since the polarization for quasi-TE mode in a SOI waveguide is mainly longitudinal in correspondence of the scattering elements, the radiated field is supposed to be mainly longitudinally polarized. Furthermore the angular grating structure is cylindrically simmetric, hence we expect that the radiated beam maintain this symmetry. The polarization of the emitted beam is therefore supposed to change its direction about the optical axis in a cylindrically symmetric pattern. Optical vortex with SOP that possess these properties are said cylindrical vector (CV) beams. Zhu et al. in [117] theoretically demonstrated these properties for optical vortex generated by angular grating-based emitters and provided analytical expression for the far field-components of the radiated beam. We report some of such results which are useful to the understanding of the properties of the OAM beams analyzed in this work.

In theoretical work reported in [117], azimuthally polarized dipole oscillators $\mathbf{P}_m = \hat{\varphi}_m P_0 \exp(jl\varphi_m)$ are used to describe the emission of the scattering

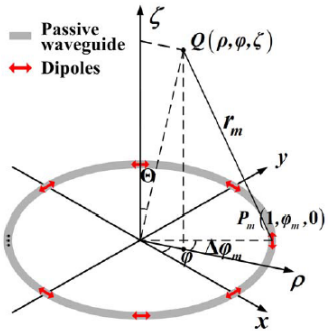

Figure 6.6: Schematic diagram of the dipole model used in [117].

elements. The radiated electric field in each point $Q(\rho, \varphi, \chi)$ of the upper hemisphere, see Fig. 6.6, is given by the interference among the radiation of all the dipoles:

$$E_l(\rho,\varphi,\chi) = \frac{A}{R^3}\sum_{m=1}^{q}\exp(j\nu r_m)\exp(jl\phi_m)\left[(\frac{\nu^2}{r_m} - j\frac{\nu}{r_m^2} - \frac{1}{r_m^3})(r_m \times \phi_m)\times\right] \tag{6.25}$$

$$\times\, r_m - (j\frac{2\nu}{r_m^2} + \frac{2}{r_m^3})(r_m \cdot \phi_m)\cdot r_m]$$

where $A = P_0/4\Pi\varepsilon_0$, r_m is the distance between Q and the m_{th} dipole $P_m(1, \phi_m, 0)$ and $r_m$is the unit vector in the direction of P_mQ pointing from P_m.

Neglecting the near-zone terms ($\sim \frac{1}{r^2}$ and $\sim \frac{1}{r^3}$) and using the Fresnel diffraction paraxial approximation, one obtains the far-field analytical expression of the radiative field components:

$$E_{\rho,l}(\rho,\varphi,\varsigma) = j^l\frac{Alq}{R^3}\frac{\nu}{\rho}\Phi(\rho,\varsigma)\exp(jl\phi_m)J_l(-\nu tan(\Theta)) \tag{6.26}$$

$$E_{\varphi,l}(\rho,\varphi,\varsigma) = j^{l-1}\frac{Aq}{R^3}\frac{\nu^2}{\varsigma}\Phi(\rho,\varsigma)\exp(jl\phi_m)J_l'(-\nu tan(\Theta)) \tag{6.27}$$

$$E_{\varsigma,l}(\rho,\varphi,\varsigma) = -j^l\frac{Alq}{R^3}\frac{\nu}{\varsigma}\Phi(\rho,\varsigma)\exp(jl\phi_m)J_l(-\nu tan(\Theta)) \tag{6.28}$$

where $\Phi(\rho,\varsigma) = \exp\{j\nu[\varsigma + (\rho^2+1)/2\varsigma]$,$J_l$ are Bessel functions of the first kind and $\Theta = \tan^{-1}(\rho/\varsigma)$.

The expressions represent a set of orthogonal cylindrical vector Bessel beam (CVB) for each component. Each component has well defined OAM order determined by the azimuthal order l in the phase factor $\exp(jl\varphi)$. The spiral-like

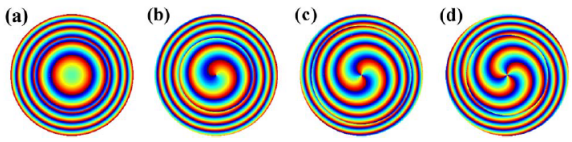

Figure 6.7: Far-field transversal phase distribution of $E_\phi(l=0)$ (a), $E_\rho(l=1)$ (b), $E_\rho(l=2)$ (c) and $E_\phi(l=3)$ (d), from[117].

pattern of the complex phase distributions of radial and azimuthal components is shown in Fig. 6.7 for different OAM orders.

Each component's amplitude is proportional to the l_{th}order Bessel function of the first kind or to its derivative and propagate in constant angle $(-\nu tan(\Theta))$ to the ς axis . Nevertheless, each component has a different scaling factor and the amplitude of the radial and longitudinal components are proportional to OAM order l. This implies that that for $l=0$ the far field emitted beam is purely azimuthal-polarized.

Considering the azimuthally polarized radiated beam, the electric field is given by:

$$E_{\varphi,l}(\rho,\varphi,\varsigma) = \begin{bmatrix} E_x(\rho,\varphi,\varsigma) \\ E_y(\rho,\varphi,\varsigma) \end{bmatrix} = E_l(\rho,\varsigma) \begin{cases} -\sin(\varphi) \\ \cos(\varphi) \end{cases} \quad \exp(il\varphi) \tag{6.29}$$

Using Euler relations and Jones vectors, Eq. (6.29) can be rewritten as:

$$E_{\varphi,l}(\rho,\varphi,\varsigma) = E_l(\rho,\varsigma)\frac{i}{2}\begin{bmatrix} 1 \\ -i \end{bmatrix}\exp(i(l+1)\varphi) + E_l(\rho,\varsigma)\frac{i}{2}\begin{bmatrix} 1 \\ i \end{bmatrix}\exp(i(l-1)\varphi) \tag{6.30}$$

The field can be therefore described as the sum of a right hand circularly polarized (RHCP) beam, described by the Jones vector $\begin{pmatrix} 1 \\ i \end{pmatrix}$, with topological charge of $l-1$ and a a left hand circuarly polarized (LHCP), Jones vector $\begin{pmatrix} 1 \\ -i \end{pmatrix}$ bean with topological charge of $l+1$. This is a fundamental property of azimuthally polarized CV beam and will be exploited in the demodulation scheme employed in the experimental analysis.

6.3.3 Omega-shaped OAM multiplexer

The second type of the analyzed OAM emitters consist of non-resonant cavity made by a quasi-circular waveguides wich are connected to bus waveguides through a gap in correspondence of an opening-angle α (see Fig. 6.8). In order to extract the light traveling in the omega-shaped waveguide, second order angular grating are embedded in the inner vertical sidewalls as for the case of microring OAM emitters which we have described in the previous section. The

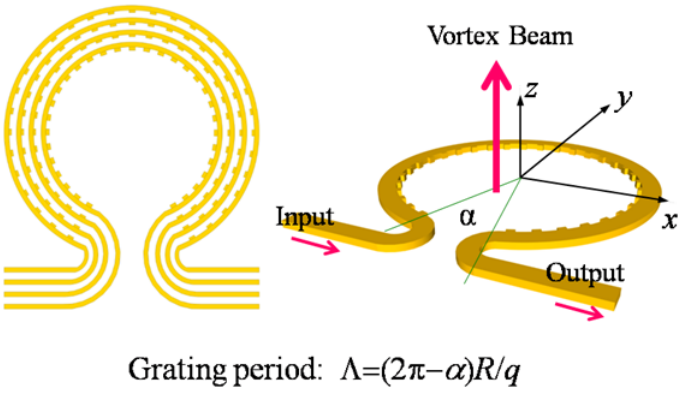

Figure 6.8: Layout of Omega-Shaped OAM multipliplexer.

innovative omega-shaped geometry allows to pack, in the same planar substrate, several emitters with the same optical axis allowing the multiplexing of beams with different OAM orders. The theoretical analysis of the OAM beam emission carried out for microring-based emitters can be still applied to these devices. Nevertheless there are important differences related to the selectivity in the emitted frequency which must be considered in terms of purity of the beams.

When all the waveguides of the omega-shaped device are excited, due to the orthogonality between the OAM orders, the radiated beam is simply the sum of the different beams emitted by the single waevguides. The relationship between the OAM order of the emitted beam and the input optical wavelengths is:

$$l_{emit} = \sum_i l_i = \sum_i sign(p)(p - q_i) \tag{6.31}$$

where $sign(p) = +$ or - represents the CW or CCW traveling optical modes inside each arc waveguide, $p_i$is the azimuthal order of the equivalent microring and q_i is the number of grating periods.

In single-pass open microrings, no conditions on the round trip phase shift need to be satisfied in order for the wavelength to circulate in the device. The requirement of integer azimuthal order, that imposed an integer valued OAM order in microring emitters, is relaxed and all the circulating frequencies are emitted as long as the phase matching condition, given by Eq. (6.29), is fulfilled. The OAM order, of the emitted beam is not necessarily integer. For the resonance wavelengths of the equivalent microrings, a better purity of the emitted beam is expected since the radiated beam has an integer valued topological charge matching with the phase distribution of the proper OAM beams. This implies that OAM beams corresponding to these wavelength have a OAM order dominant on the others resulting in higher side mode suppression ratios (SMSR). On the other hand the transmittance and the overall radiative power is not expected to change with the frequency.

The value of the opening angle α plays a fundamental role in the performance of the omega-shaped devices. Wide angles are preferable since more microrings can be inserted concentrically and/or more space is available for the bend waveguides connecting the omega-devices to the bus waveguide. Sharp bends and abrupt variation of the effective refractive index along the optical path introduce excess losses and consistent back-reflection and must be avoided. On the other hand, small angles ensure a better purity on the OAM vortex emitters due to a smaller perturbation in the azimutally distribution of the radiation.

In Fig. 6.9, we report simulative estimations of side mode suppression ration (SMSR) for OAM orders $l = 0, \pm 1, \pm 2, \pm 3, \pm 4$ emitted by the studied devices for the resonance wavelength of the equivalent microring as a function of opening angle. The SMSR values considered are calculated as the ratio between the power of the dominant mode over that of second highest mode. The values show, as expected, that SMSR degrades as the opening angles increases but that for opening angle values smaller than 10°, SMSR is high: SMSR values grater than 100 or 20 dB are obtained for all the OAM orders considered. Furthermore, for wider angles only the OAM orders $l = 0, \pm 1$ achieve SMSR values grater than 100 while the purity of the other OAM orders reduces to SMSR values contained in the range $10 - 100$ for angle equal 15°. This simulative estimation show that the opening angle affects dramatically the purity of emitted OAM beam and demonstrate that coupling angle values smaller than 10 are required for acceptable SMRS values (> 20 dB) with OAM orders $l \leq 5$. At the same time low OAM orders beam seem not to be considerably affected by the aperture and can be used with wide opening angles. The properties of the OAM beams emitted by wide angle omega-shaped emitters , $\alpha > 10°$, have been analyzed in the experimental analysis and will be discussed later.

6.4 Results of radiation efficiency measurements of microring-shaped emitters

In the first part of the study, the research activity focused on the optimization of the grating and layout design of microring OAM emitters. In particular, devices with different geometrical layouts and embedding scattering elements of several shape and dimensions have been characterized in terms of emitted and transmitted power. The experimental analysis on the radiation efficiency is aimed at providing information on the combined effect of the geometrical parameters on the performance of devices and to give a guideline for the optimization of the design of such type of emitters.

The layout of the OAM microrings emitters is reported in Fig. 6.10:

As for the layout, different values for the Euler Bend $EuPi$ and the coupling angle θ have been considered. The Euler band $EuPi$ is defined as $EuPi = \Pi/\phi$ where ϕ is the half-angle of the arc connecting the bus waveguide and the coupling section. The coupling angle θ is the angle corresponding to coupling section, i.e. the section where the ring and the bus waveguide are parallel. These

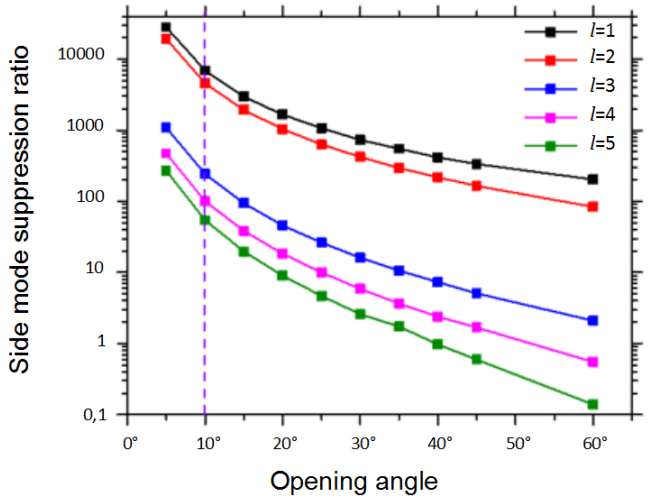

Figure 6.9: Simulative estimation of SMSR for different OAM orders as a function of the omega-shaped device opening angle. Such simulations have been carried out by Dr. Ning Zhang of the University of Glasgow.

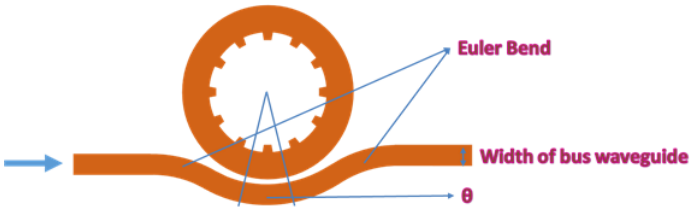

Figure 6.10: Schematic representation of the microring resonator OAM emitter.

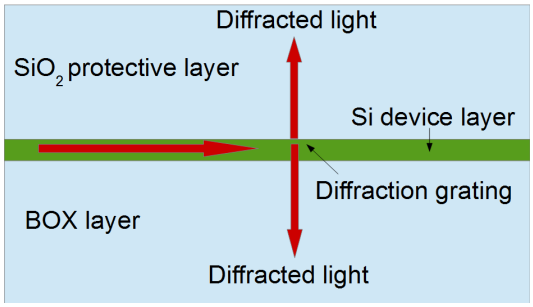

Figure 6.11: Schematic representation of the symmetry of the OAM emitters.

two geometrical parameters play a fundamental role in the coupling efficiency between the bus waveguide and microring and are therefore expect to affect the performance, and in particular the radiation efficiency, of the device, as will be described later.

A preliminary remark on the maximum radiation efficiency has to be done. Since the SOI device is covered by a silica protective film; the stack made up of the BOX layer, silicon device layer and silica protective layer is therefore symmetrical with regard the waveguide plane. This symmetry limits the maximum power that can be emitted: considering the ideal case of a complete emission of radiation by the waveguide, half of the power is radiated upward and half downward. The emission efficiency in these devices cannot therefore exceed 50%. Higher values can be obtained either breaking the symmetry of the structure or reflecting upward part of the radiation directed toward the substrate. In this work, we focus our attention on the analysis of the grating and microring design in order to approach the maximum theoretical radiation efficiency for symmetrical SOI devices.

In order to maximize the radiated power two issues must be addressed: the loss of the resonant structure and the critical coupling. As for the first, it is quite intuitive that the scattering induced by the gratings should be the most effective source of loss of the radiation circulating in resonator: the lifetime of a photon should be long enough to allow the photon be scattered. The state-of-art technology for SOI waveguide shows a propagation loss, as described in Chapter 2, of few dB/cm. For small rings as the ones analyzed here, with radius values < 30 μm, the propagation loss is negligible and the biggest contribute is due to the mismatch between the mode of the coupling region and that of the single waveguide. This perturbation in the waveguide cross-section causes a certain amount of the circulating radiation to be reflected back in the waveguide or scattered to the radiating modes. The typical value of loss induced by the modal mismatch are are about 0.03 dB per round trip. On the other hand, due to the high index contrast contrast of silicon waveguide, even shallow grating brings to significant coupling. The typical "loss" induced by the grating is of the order of 0.12 dB per round trip. This means that if the microring is well

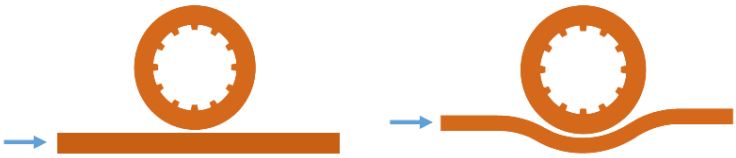

Figure 6.12: Standard point coupler geometry (left) and optimized geometry (right) of the microring OAM emitter.

designed, the first requirement is easily met in a sidewall grating technology.

Concerning the second issue, as explained in Chapter 2, the minimum transmittance of a ring resonator and consequently the maximum power stored, is observed when the device operates at the critical coupling condition. Under critical coupling condition, the internal losses equal the coupling power; slight deviations from this value induces drastic variation of the performance of the device. Since the embedded second order gratings are designed to efficiently extract light from the waveguide, coupling strength greater than 10 are required to achieve critical coupling. In standard point coupler geometry, similar coupling strength require a reduction of the gap down to distances less than 100 nm which add modal mismatch loss and cause technological complications in the lithographic and etching processes. The extension of the coupling region from a point to a section where bus waveguide and ring are straight and parallel, similarly to racetrack geometry would impair the cylindrical symmetry and reduce the purity of the emitted mode.

In order to address this issue, the geometry employed in the microring devices analyzed makes use of a curved bus waveguide running parallel to a section of microring, as depicted in Fig. 6.12.

This layout allows not to impair the cylindrical symmetry of the structure, essential for the emission of the OAM optical vortex and to the other hand enlarges the coupling region. The power transferred from the bus waveguide to the ring and viceversa is determined by the the angular extent of the coupling section. This geometry solution arises challenging issues in the layout design: firstly the radiation traveling in the curve bus waveguide may suffer bend loss and the effective power in the coupling section may be significantly lower than the injected one. Furthermore, a modal mismatch appears at the beginning at the end of the coupling region, in correspondence of the bend connecting the straight waveguide to the curved section. In addition, the radiation circulating in the microring and the one passing through the bus waveguide may run out of phase the path due to the different radius of curvature. One solution can be the reduction of the effective refractive index of the bus waveguide by narrowing its width. This solution reduces the optical path of the outer radiation and restores the phase-matching condition.

As for the scattering elements, two geometries have been employed: one with sinusoidal shape and one with rectangular shape (see Fig 6.13). Furthermore

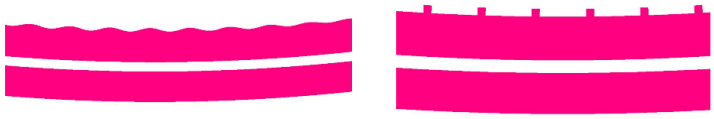

Figure 6.13: Sine geometry and rectangular geometry of the second-order gratings which are embedded in the OAM emitter.

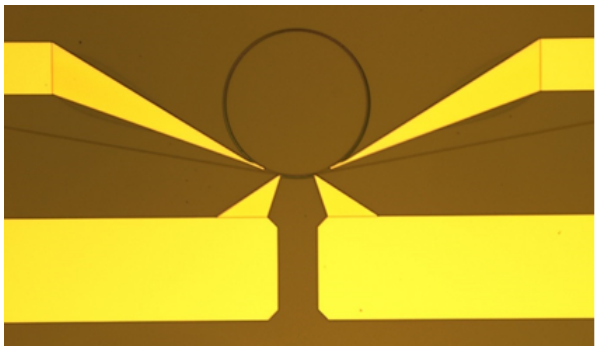

Figure 6.14: Optical image of a manufactured ring-shaped emitter with metallic tracks and pads for thermal tuning of the coupling section.

rectangular gratings with different values of height and width (i.e. duty cycle) have been considered. The details of the grating layout will be given in the next section. Each of these parameters can alter significantly the power of the circulating radiation that is extracted by the second order grating as demonstrated in different works, see for example [118, 119]. In fact, the height of the teeth determines the extent of the dielectric function perturbation and consequently the coupling strength of the grating. On the other hand, the shape and width of the gratin teeth set the spatial Fourier components of the gratings and consequently the orders of diffraction of the gratings that can be exploited for the phase-matched scattering.

Keeping in mind these considerations, it's clear that the variation of just one the considered layout parameter can dramatically alters the propriety of the devices. Furthermore it's hard to predict how the variations of the parameters are correlated and to know a priori the combination that optimizes the layout. For this reason, the measurements of radiation efficiency for various combinations of these parameters could provide important infrormation for the understanding the impact of these parameters on the properties of the emitted OAM beam and on the performance of the devices.

The microring OV emitters have been manufactured starting with a SOI wafer containing a 220 nm silicon device layer and 2 μm-thick buried oxide (BOX) layer. The device geometry was patterned through electron lithogra-

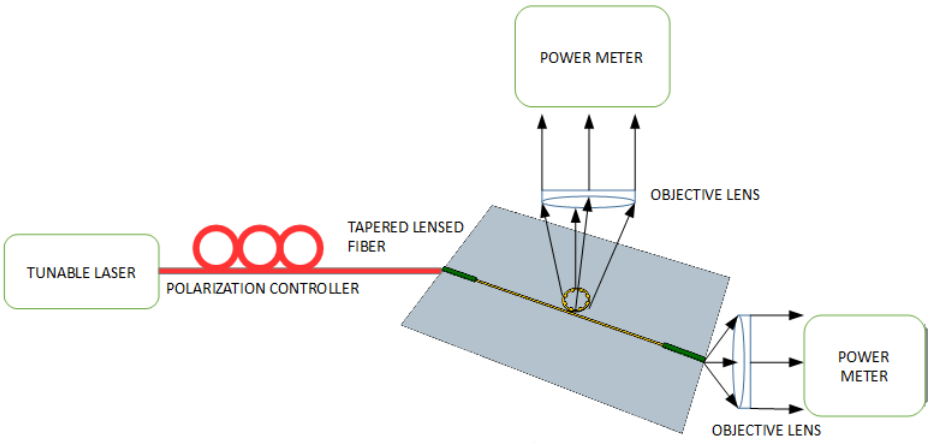

Figure 6.15: Experimental set-up for the measurement of the radiation efficiency.

phy on a negative photoresist, hydrogen silsesquioxane (HSQ), and dry-etched anisotropically on silicon layer down to the BOX layer. Finally, the manufactured devices have been covered by a protective layer of silica. The expected geometry of the bus waveguide and of the ring waveguide is $(500 \times 220)\ nm$. The coupling distance is $150\ nm$, the radius of the microring is $29\ \mu m$ and the period of the embedded second order grating is $650\ nm$. The radiation efficiency of the nanofabricated angular grating-based microring emitters has been estimated analyzing the spectrum of transmittance and radiance.

The setup employed for these measurements is reported in Fig 6.15. A tunable laser source is uused for generating a stable polarization radiation injected into the bus waveguide through a singlemode tapered lensed fiber with a spot diameter matching the dimension of the polymer waveguide hosting the nanotaper.

The polarization of the field is adjusted through a polarization controller in order to excite the quasi TE mode of the silicon waveguide. The power of the transmitted field P_{tra} at the endface of the sample and the power of the optical vortex beam P_{rad} are collected through a high sensitivity Germanium power meter. Due to the high divergence of the transmitted field exiting the waveguide and of the emitted radiation, we used objective lenses to collimate the beams and direct them toward the camera and the other optical instruments.

The emission efficiency η of the device is defined by the ratio of the emitted power P_{rad} to the optical power in the midpoint of the access waveguide P_{in}:

$$\eta = P_{rad}(dBm) - P_{in}(dBm) \tag{6.32}$$

Assuming the same coupling loss at the two facets,P_{in} can be calculated as:

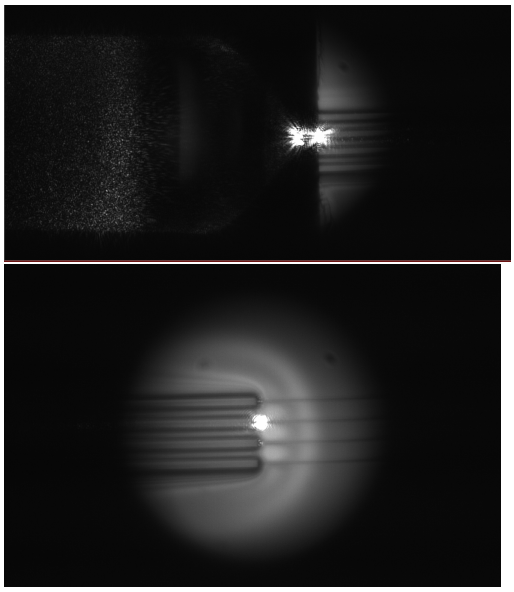

Figure 6.16: IR image captured of the lensed fiber used to inject light in the polymer waveguide (up) and of the scattered light at the end of the polymer taper (down).

$$P_{in}(dBm) = \frac{P_{inj} + P_{tra}}{2}(dBm) \tag{6.33}$$

where P_{inj} is the power emitted from the input fiber lens.

The transmission spectrum of one of the microring OAM emitter for the wavelength range of $1540 - 1565\,nm$ is reported in Fig. 6.17 . The spectrum shows dips arranged in a periodic pattern similar to the ones observed for microring resonators without gratings in the sidewalls, see for example Fig. 2.18. The wavelengths of the dips correspond to the resonance wavelengths of the microring at which the radiation is stored in the ring. The distance between the dips is about 3.1 nm gap and is in accordance with the expected free spectral range of the microring, which is calculated using the group index of SOI waveguide 4.1 and the microring perimeter of 182 um. The observed extinction ratio is high for all the dips (more than 10 dB); this results show that the coupling strength is high enough to efficiently feed the resonance mechanism.

Fig 6.17 reports the transmission spectrum and radiation spectrum of one of the manufactured microring emitters. In this case, the range and the wavelength step of the tunable laser sweep have been reduced to enhance the accuracy and the precision of the measurements. The obtained peaks and the dips are observed at the same wavelengths; this demonstrates that when the microring operates in resonant condition, the light is stored in the resonator and is partly extracted by the embedded grating as expected. The observed spectra show

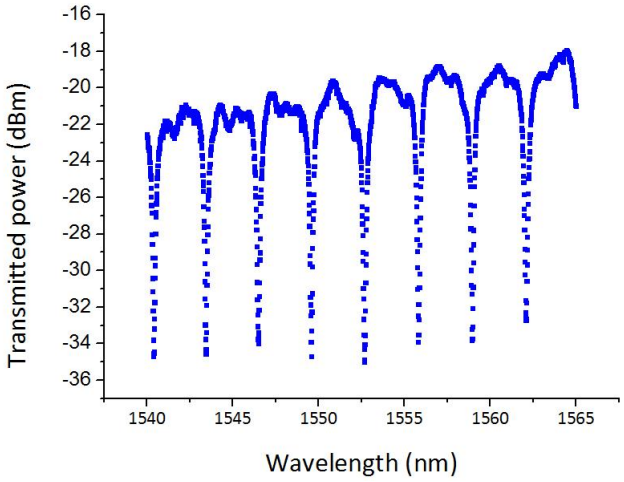

Figure 6.17: Measured transmission spectrum for a microring OAM emitter.

transmittance dips vales of about 7 dB while the radiation peak values grater than 4 dB; the values obtained in the measurements of other microrings are comparable with such values. It's possible to observe that the shape and the full width half maximum (FWHM) of the obtained peaks are more similar to the ones of a lossy microring resonators. In fact, the phenomenon of scattering of the circulating light by the diffracting elements represents, as described, a significant source of loss for the resonator. Differently with an ideal resonator which is not affected by any kind of loss and shows delta-like peaks, a lossy resonator, due to the limited photon life time, presents reduced the extinction ratio and a broadening of the peaks as observed in the spectra of the analyzed emitters.

The transmission and radiation spectra recorded have been used for the estimation of the radiation efficiency of the ultracompact OAM beam emitters with different geometrical parameters. Some results of the emission efficiency estimations are reported in Figg. 6.19, 6.20 and 6.21.

First of all, high values of radiation efficiency have been obtained, greater than 20%, for different geometries analyzed proving the efficiency of these devices in trapping ed emitting light. The gratings with 90 nm high and 90 nm wide scattering elements show the highest value of radiation efficiency: for Euler bend angle of 5° the efficiency obtained is around 26%. Furthermore, valuer greater than 13% have been obtained for Euler bend sweeping from 4° to 12°. Nevertheless, grating with geometries of (120×60) nm and(90×60) nm have achieved high value of emission efficiency with maximum efficiency about 20% and values greater than 13 for almost all the geometry considered. These grating layouts resulted to have the greatest coupling strength and will be employed in future analysis for the optimization of the devices. As for the other grating ge-

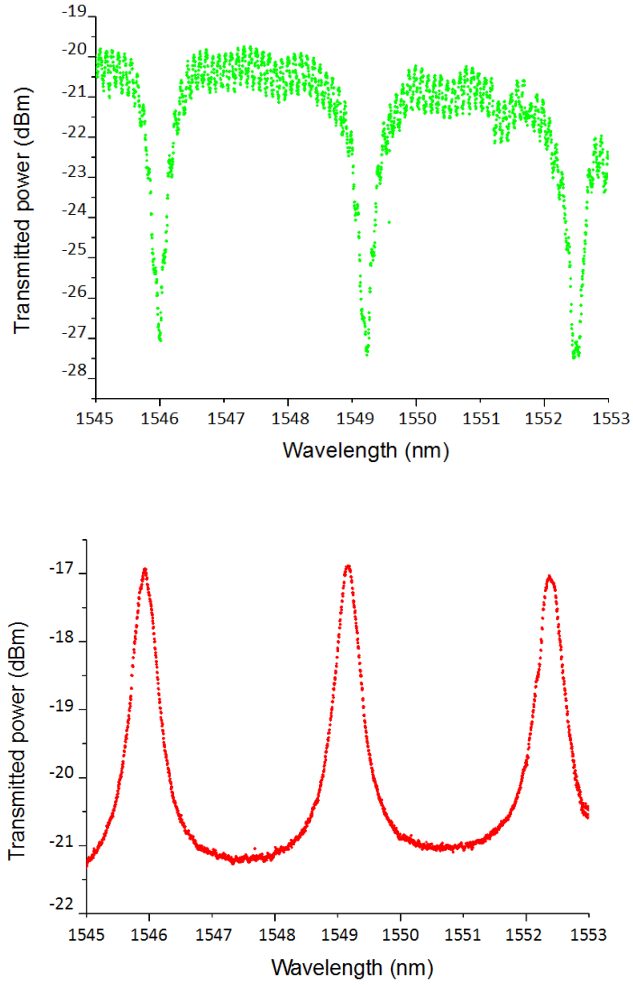

Figure 6.18: Measured transmission and radiation spectra for a microring OAM emitter.

	Sine 20 nm	(60x100) nm	(60x150) nm	(90x60) nm	(90x90) nm
EuPi = 0°, θ = 12°	10-11%	8%	13,5-14,5%	10%	11-12%
EuPi = 0°, θ = 15°	11-12%	6-6,5%	-	-	19-19,5%
EuPi = 3°, θ = 12°	10-11%	8,5%	14%	17%	17-18%
EuPi = 3°, θ = 15°	-	5-6%	11-12%	12,5-13%	15%
EuPi = 5°, θ = 12°	10-11%	10-11%	-	13,5-14%	23-24%
EuPi = 5°, θ = 15°	-	-	-	-	22-23%
EuPi = 7°, θ = 12°	-	6-6,5%	-	16,5-17%	12,5-13%
EuPi = 7°, θ = 15°	-	6%	-	9-10%	12-13%

Figure 6.19: Measured radiation efficiency as a function of Euler bend angle $EuPi$ and coupling angle θ, for different sine and rectangular grating geometries.

	Sine 20 nm	(60x60) nm
EuPi = 0°, θ = 3°	-	6%
EuPi = 0°, θ = 4°	11%	5-6%
EuPi = 0°, θ = 5°	11%	5%
EuPi = 0°, θ = 6°	-	-
EuPi = 0°, θ = 8°	12%	-
EuPi = 0°, θ = 10°	13%	-
EuPi = 0°, θ = 12°	11%	-
EuPi = 0°, θ = 15°	-	-

Figure 6.20: Measured radiation efficiency as a function of Euler bend angle $EuPi$ and coupling angle θ, for different sine and rectangular grating geometries.

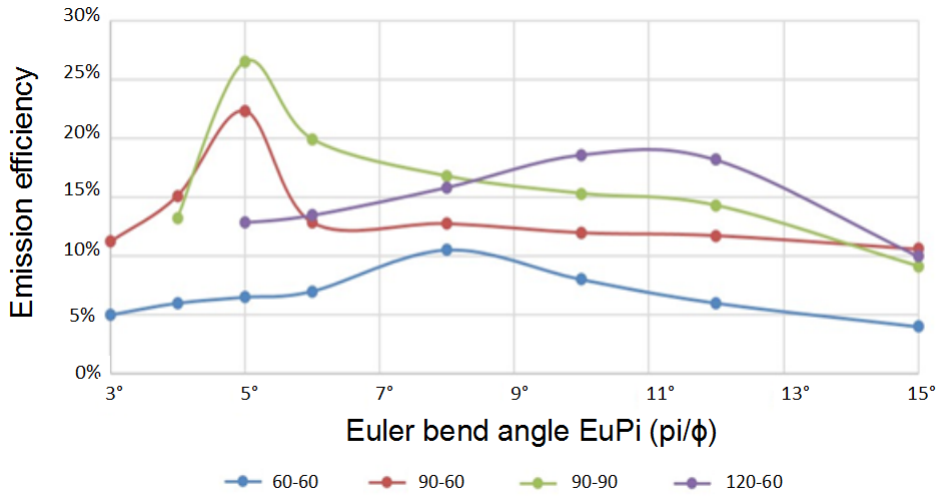

Figure 6.21: Radiation efficiency as a function of Euler bend angle for different grating geometries.

ometry, the sinusoidal shaped gratings show promising efficiency values as well, taking into consideration the small eight of the protrusion analyzed: in fact values around 11% have been obtained for 20 nm of extension. Nevertheless, sine grating with bigger heights have brought to lower radiation efficiency: this is likely to stem from technological issues arisen by the requirement of continuously varying patterning of the structures on bigger scale. Further analysis are again required for exploring the potential of this grating geometry.

Beside the grating layout, the results highlight the influence of the microring layout on the emission efficiency. In particular, the Euler bend angle has proved to affect dramatically the emission for (90×90) nm gratings: sweeping the Euler bend angle values in the range 4°-15°, the emission efficiency values vary from 9° to 26°. The same behavior can be observed for other squared gratings geometries, in particular(120×60) nm and(90×60) nm but within a reduced range of radiation efficiency values. On the other hand, the performance of sinusoidal shaped gratings emitters proved to be less affected by variation in Euler band and coupling angle values: radiation efficiency values about 11 have been obtained for all the Euler band and coupling angle combination considered. The same happens for squared gratings with low emission efficiency as $(60x100)$ nm. Furthermore, gratings with different radial protrusions are differently affected by the variation of geometrical parameters: maximum values of radiation efficiency for (90×60) nm, (60×60) nm and (120×60) nm correspond to different values of Euler bend, in particular 5°, 9°and 10° respectively. On the other hand, highest efficiency values for grating with the same height, (90×60) nm and (60×60) nm have been obtained for the same Euler bend angle. These results can be explained considering that the grating strength determines the loss of the resonator and consequently the coupling strength at which the critical coupling condition occurs. Therefore, different grating height can shift geometrical parameters values, as Euler band angle, that make the emitters operate at critical coupling condition.

In conclusion, the experimental values obtained show that the greatest emission efficiency is obtained for squared grating with height values of 90 nm and width values of 60 nm and 90 nm, corresponding to duty ratio of 10% and15%, respectively, and with Euler band angle of 5°. Such outcome highlights this layout as a promising starting point for the optimization of the OAM beam emitters radiation efficiency. Nevertheless, due to the extreme sensitivity of the device to the variation of geometrical parameters and to geometrical nonidealities induced by the nanofabrication processes, it is not possible to understand whether the ring is or not in critical coupling condition and attribute the obtained efficiency solely to the grating and ring design. Further analyses will be carried out in order to remove this ambiguity and evaluate the maximum potential radiation efficiency of the various layout. In particular, the experimental measurements of radiation efficiency will be performed employing metallic microheater for thermally tuning the coupling strength of the ring and reaching critical coupling condition.

6.5 Results of the characterization of the omega-shaped multiplexers

In the second part of this study on integrated OAM beam emitters, the research activity has been focused on omega-shaped emitters for OAM radiation multiplexing. The working principles of this innovative type of OAM emitter have been assessed through the analysis of the optical properties of the radiated beams in terms of phase distribution, state of polarization and order purity. The characterization of the OAM beams required a demodulation scheme that transforms any OAM order l of into zero order. The demodulation technique employed in these measurements consists, basically, of imparting a phase modulation pattern wich match the one of the beam itself but with opposite topological charge. The principle is analogous to the modulation scheme, described in section 6.2, where a spiral phase plate (SPP) is employed to convert TEM laser beam into OAM beam of any order. Nevertheless, in the measurements reported, the phase modulation is not imparted through a SPP, but through a spatial light modulator (SLM) that allows to electronically configure the phase pattern to impose. The mode purity of the OAM beam, i.e. the fraction of power carried by a single OAM order with regard the overall power of the beam, can be estimated comparing the pattern of the demodulated beam with a Gaussian like beam. In fact, as described before, a zero order CV beam has an intensity distribution comparable to a Gaussian beam and by estimating the amount of normalized power contained in the central spot of each demodulated beam, it's possible to quantify the purity of the order.

The setup employed for the analysis of the optical vortex beam emitted by the omega-shaped devices is reported in Fig. 6.22. The complexity of the demodulation procedure required the addition of several tools to the setup used for the analysis of radiation efficiency for ring-shape OAM emitters. The optical vortex beam radiated by the devices is collected by the objective lens and passed through a quarter waveplate. This plate, built combining multi-order crystalline quartz waveplate, induce an optical phase shift of $\lambda/4$ between the polarization aligned with its fast and slow axis. This phase shift transforms circularly polarized light into linear polarized light with the direction of the electric field oriented at 45° to the fast axis. According to the decomposition of a CV beam described above, an OAM order l beam can be decomposed in 2 linearly polarized beam with different orientation of order $l-1$ and$l+1$. An high extinction ratio ($> 50\ dB$) nanoparticle film linear polarizer selects the beam with the polarization aligned with its axis which impinges on the (SLM). The (SLM) which we have employed is basically a reflective liquid crystal (LC), mounted on silicon layer, containing anisotropic rod-like molecules. The orientation of these molecules, in each pixel, is controlled by an electric field which rotates the fast and slow axis of this birefringence crystal. This mechanism allows to impose a electronically controlled phase pattern modulation to incident light which is reflected by the silicon substrate, after passing the LC layer. The SLM works with linear polarized radiation which is vertically aligned to the screen; the axis

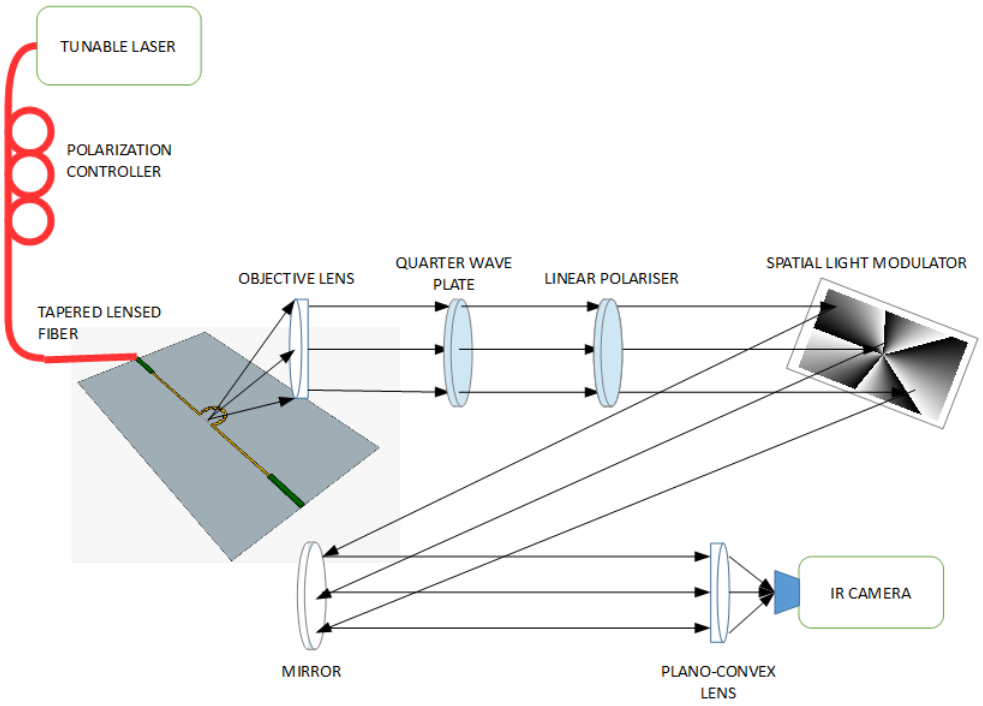

Figure 6.22: Experimental set-up for the measurement for the Omega-shaped OAM emitters.

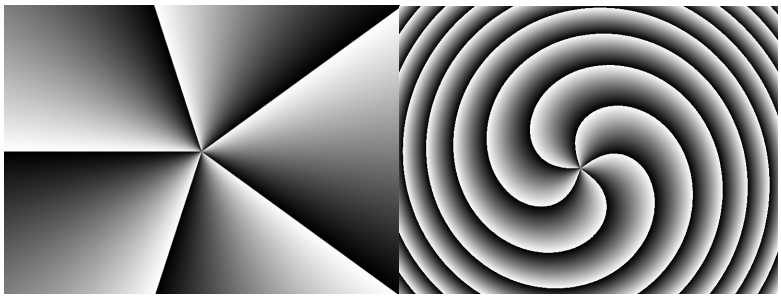

Figure 6.23: Phase pattern employed in the SLM for the OAM beam demodulation with$l = 5$ (left). The same pattern with the lens phase factor (right).

of the polarizer and the axis of the SLM are therefore aligned. Finally, the collimated optical vortex beam is focused on the screen of a high sensitivity and high resolution InGaAs camera. For the observation and recording of far-field image of the radiation pattern, a plano convex lens is posed along the optical path focusing on the back focal plane of the objective lens.

An example of the phase pattern used in the SLM is reported in Fig 6.23: this pattern is used for the demodulation of beam with OAM order$l = 5$. On the right, we report the same pattern with the addition of a lens phase factor $\propto exp(j\rho^2/2f)$, where ρ is the radial coordinate and f the focal length. Comparing this pattern with the phase distribution reported in Fig. 6.7, it's clear that the lens phase factor improves the matching between the modulation pattern and the impinging CV beam: a very good emulation of the Bessel-like radial dependence in the spiral pattern of the OAM beam, expressed by Eq. (6.25), can be obtained. In order to improve the matching between the impinging beam and the SLM pattern, it is possible to modify the "focal length" of the lens phase until a good demodulated pattern is obtained. The demodulated optical vortex beam, which theoretically has OAM order $l = 0$, shows a Gaussian-like intensity distribution which can be observed and recorded through the InGaAs camera.

The omega-shaped devices have been nanofabricated employing the same manufacturing technological processes used for the nanofabrication of the microring emitters which have been described in the previous section.

Fig. 6.24 shows two images of the omega-shaped devices analyzed which have been captured through a visible camera. In the image on the left, it's possible to observe the complete layout of the device: the single pass emitters, the straight and curved section of the bus waveguides, and the metallization which can be used for tuning the resonance wavelength of the equivalent microrings. On the right we report is a particular of the omega-shaped emitters showing solely the waveguides embedding the second order angular grating; the device is realized packing concentrically four microrings with an opening angle of about 15°. The layout allows to obtain a compact device with reduced footprint: such device is contained in a $(250\ \mu m \times 250)\ \mu m$ area. At the same time, the device does not contain sharp bends or abrupt discontinuities in the waveguide section that

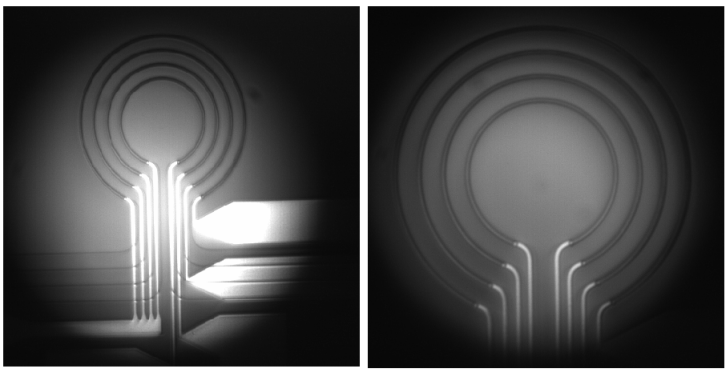

Figure 6.24: Layout of the OMEGA-shaped devices.

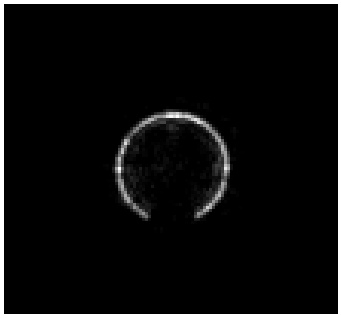

Figure 6.25: Near-field intensity distribution of the beam radiated by the Omega-shaped emitter exciting one waveguide.

could induce bend losses, back scattering or unwanted reflections.

In the first part of such experimental analysis which we have carried out on omega-shaped devices, we evaluated the optical properties of the emitted beams with different OAM orders exciting the waveguides singularly. At this stage we have analyzed the intensity distributions of the emitted OAM beams without the employment of the described-above modulation technique and we have estimated the resonance wavelengths of the equiavalent microrings of the devices. Such values have been employed for the analysis of the demodulated beams which is discussed later.

Fig. 6.25 shows the obtained near-field intensity distribution when the inner omega-shaped emitter is excited.

The pattern is clearly visible and neat, and match, as expected, with the geometry of the device. The numerical aperture of the objective lens allows to collect a sufficient amount of the spatial frequencies contained in the radiation.

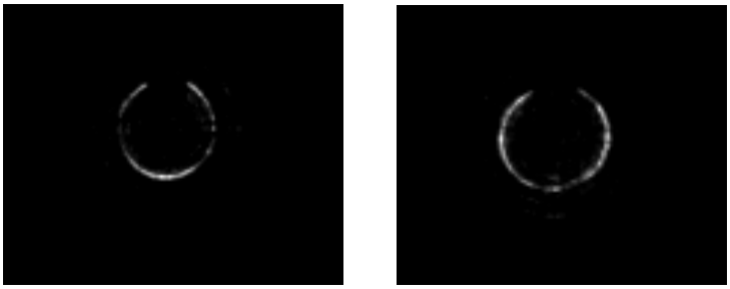

Figure 6.26: Near-field intensity distribution of the beam of Fig. 6.24 after a polarizer horizontally (left) and vertically (right) oriented. Rotating the polarizer the two.lobe pattern rotates in the same manner.

The intensity distribution is quite uniform along the azimutal direction; this implies that the device efficiently extracts and directs the circulating light toward the lens with almost the same intensity all along the optical path.

Then, we have analyzed the state of polarization of the emitted beams through the employment of a polarizer after the objective lens. When the polarizer is aligned along the horizontal direction solely horizontally polirized radiation is transmitted and low intensity area are visible on the equatorial points, see Fig. 6.26 (left). In these points the radiation is therefore vertically polarized. Rotating the polarizer of 90°, the lower intensity is observed at the poles. The same results are obtained for arbitrary orientation of the polarizer. Such outcomes show that the emitted beams have no radial components: as expected, the SOP of the beam emitted by omega-shaped device is predominantly azimuthally polarized analogously to case of CV radiation of microring-based devices.

As discussed in section 6.3.3, due to the open geometry of the device and the absence of resonance mechanism, the response in frequency of the omega-shaped emitters is expected to be quite flat. In fact, the radiation and transmittance spectrum obtained for the omega-shaped devices don't show sharp peaks or dips differently with the case of microring-based devices. Nevertheless, it is possible to identify the wavelength corresponding to OAM order $l = 0$ taking advantage of the decomposition of the mode in circularly polarized radiations of different OAM orders, which we have described in the section 6.3.2.

The $l = 0$ beam can be decomposed as the sum of two beams with $l = -1, +1$ that possess donuts-like intensity distribution. On the other hand, the emitted beam with OAM order $l = \pm 1$, can be decomposed respectively in the OAM orders $l = 0, +2$ and $l = -2, 0$. This implies that the intensity pattern of beam with $l = 0$ is expected to be less intense in the center and that the order $l = \pm 1$ have a maximum of intensity in the center. Fig. 6.27 reports the radiation spectrum recorded in correspondence of the center of the pattern. The radiated power corresponding to the parts of the pattern which are far from the center

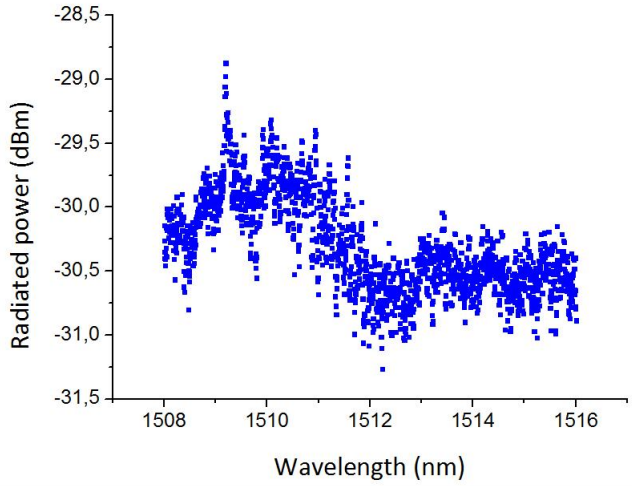

Figure 6.27: Radiation spectrum for the Omega-shaped device exciting one waveguide utilizing an iris to collect light in the center of the beam solely.

has been blocked through the employment of an iris. In the obtained image, as expected, a dip is clearly visible for wavelength values about $\lambda = 1512\,nm$ while a peak is observed for wavelength values about $\lambda = 1509\,nm$. Such wavelengths, $\lambda = 1512\,nm$ and $\lambda = 1509\,nm$, are used as starting point for the pursuit of the OAM order $l = +1$ and $l = 0$.

The wavelength corresponding to the OAM order$l = +1$ is therefore selected through the observation of the far field pattern for wavelengths values which are accurately tuned around $\lambda = 1509\,nm$ until a Gaussian-like spot is clearly visible, (Fig. 6.28(a)). The same procedure is applied for the wavelength corresponding to $l = 0$; in this case we seek a far-field image with a well defined donuts-like pattern, as shown in Fig. 6.28(c). Once inferred the FSR for the omega-devices under analysis, the OAM order $l = -1$ can be obtained in the same way (Fig. 6.28(b)). This procedure yielded the wavelengths 1508.75 nm, 1513.825 nm and 1511.25 nm for the OAM order $l = +1, 0, -1$ respectively and FSR values of about 2.54 nm, as expected from theory.

The obtained patterns, reported in Fig. 6.28 are well defined with a sharp point in the center and intensity minima and maxima which alternate along the radial direction, for OAM order $l = \pm 1$. In correspondence to halfway wavelength, ($l = 0$), the pattern shows a hole in the center and brighter points collected in ordered rings around the optical axis; this is an expected result since a zero order beam has component of the order $l = \pm 1$ whit a donuts like pattern, as described in previous sections. The outer maxima and minima, which are arranged concentrically, correspond to higher OAM order beams that are excited due to the discontinuity of the radiative pattern in correspondence of the opening angle.

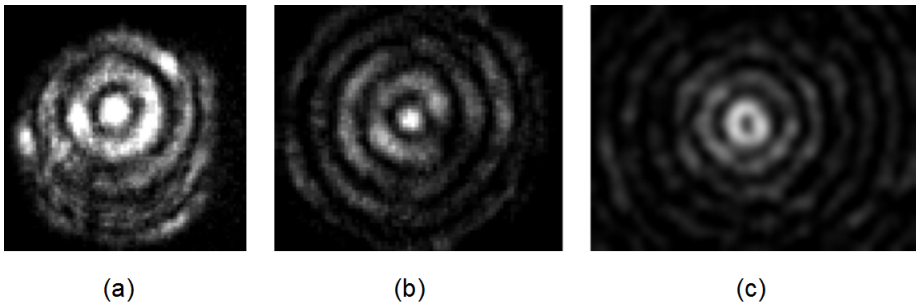

Figure 6.28: Far-field intensity distribution of the emitted beam for wavelengths $\lambda = 1508.75\,nm$ (a), $\lambda = 1513.85\,nm$ (b) and $\lambda = 1511.25\,nm$ (c) corresponding to OAM order $l = +1$, $l = -1$ and $l = 0$ respectively.

The wavelengths values corresponding to the OAM orders $l = +1, 0, -1$ and the obtained FSR are subsequently employed for the analyses of the OAM order purity and modal contents of the emitted beams. Such analysis has required the demodulation of the radiated beams which we have carried out following the procedure described above . The pattern of the demodulated beams and the phase patterns imposed by the SLM are reported for OAM order $l = +1, 0, -1, -2, -3$. In order to set the wavelengths corresponding the OAM orders, we started from the wavelengths with OAM order $l = +1$, shifted of the FSR inferred from the previous analysis and finely tuned the injected wavelength in order to obtain a well defined gaussian pattern, analogously to technique used for not-demodulated beams.

For all the OAM orders under analysis, the intensity pattern of the demodulated beams shows a bright disk in the center, where most of the energy is concentrated, and surrounding areas with lower intensity. Comparing the$l = 0$ beam in Fig. 6.28 (c) with the corresponding demodulated beam, it's possible to appreciate how the demodulation effectively redistributes the intensity of the radiated beam. The hole has disappeared, and most of the power is concentrated around the center. The energy around the disk has been "spatially" scattered destroying the Bessel-like radial dependence visible in the original pattern. Furthermore, the OAM order obtained is in accordance with the theoretical one determined by the relation given by Eq. (6.24).

As described in section 6.2, a pure mode conversion obtained through demodulated technique which we have employed, is theoretically impossible. Beams with different OAM order have different intensity distribution patterns and SLM imparts a phase-only modulation: the decomposition is therefore expected to contain different modes. Nevertheless, the demodulated patterns are good for all the OAM order beams analyzed: since the intensity distribution of the pattern is concentrated in the center of the pattern, most of the emitted radiation power is expected to be carried solely by one OAM order.

We therefore carried out an extensive set of measurements to quantify the

fraction of power of the demodulated beams which is carried by each OAM order, i.e. their purity. The purity has been analyzed through the analysis of the obtained intensity distribution patterns of the demodulated beams. In particular, for each of the wavelengths under analysis, the far field pattern has been demodulated using phase modulation patterns, through the employment of the SLM , with different OAM orders. The intensity of the obtained Gaussian spot contained in the demodulated patterns, has been calculated through image software processing of the recorded images and normalized to the power of the radiated beams. Fig 6.29 shows the obtained values for the purity of the beams with OAM order $l = 5$. The results shows that most of the power of the radiated beam is carried solely by one mode. The grating wavelength selectivity combined with the constructive phase interference of the scattered radiation in a single round trip proved to efficiently select a preferential OAM order in the radiated beam. The results show that the performance of the omega-shaped devices in terms of sideband suppression are good despite the wide opening angle (around 15°): the principal mode carries approximately 80% of the total power less than 10% is contained in the other modes. These values correspond to SMRS values of 10 dB for the device under analysis; comparable SMRS values, about 10 dB, have been obtained in the experimental analysis which we have carried out on the other OAM orders and omega-shaped emitters with different dimensions. It's worth noting that the design of the grating and layout has not been optimized; the performance of such devices, in terms of OAM order purity, can be significantly improved through systematic analysis like those which we have carried out on the ring-shaped emitters. At the light of these consideration, these results show that the omega-shaped devices, despite the open geometry and significant discontinuity ($\alpha = 15^{\circ}$) in the emission pattern, have proved to emit OAM orders beams with high modal purity and SMRS values around 10 dB.

Fig. 6.31 shows the near field intensity distributions and relative demodulated patterns of the beam, radiated by one omega device with four waveguides separately (a,b,c,d) excited. The device is designed so that for the same wavelength $\lambda \simeq 1513.4$, all the omega-shaped waveguide radiate beams with the OAM order $l = +1$. The demodulated patterns are similar to those reported in the previous analysis, as expected, see for example Fig. 6.25 and Fig. 6.26. Fig. 6.31 report the-near field and far-field intensity pattern of the radiated beam when all the waveguides are excited at the wavelength $\lambda \simeq 1513.4$. In the far field, the zero OAM order contained in each of the emitted beams, give rise to a perfectly centered gaussian-like pattern. Despite the observed pattern is the sum of the beams emitted by the four omega shaped waveguide, no distortion to the symmetry can be observed; the pattern is similar to the one observed for the single omega device. This implies that all the radiated beams are coaxially emitted and that theirs patterns sum maintaining the cylindrical symmetry of the single beam. Similar results have been obtained for the other fabricated omega-shaped emitters. Considering the high divergence angle of the radiated beams and the long between the emitters and the IR camera (about $> 1\ m$) used for the observation of the emitted patterns, misalignments between the optical

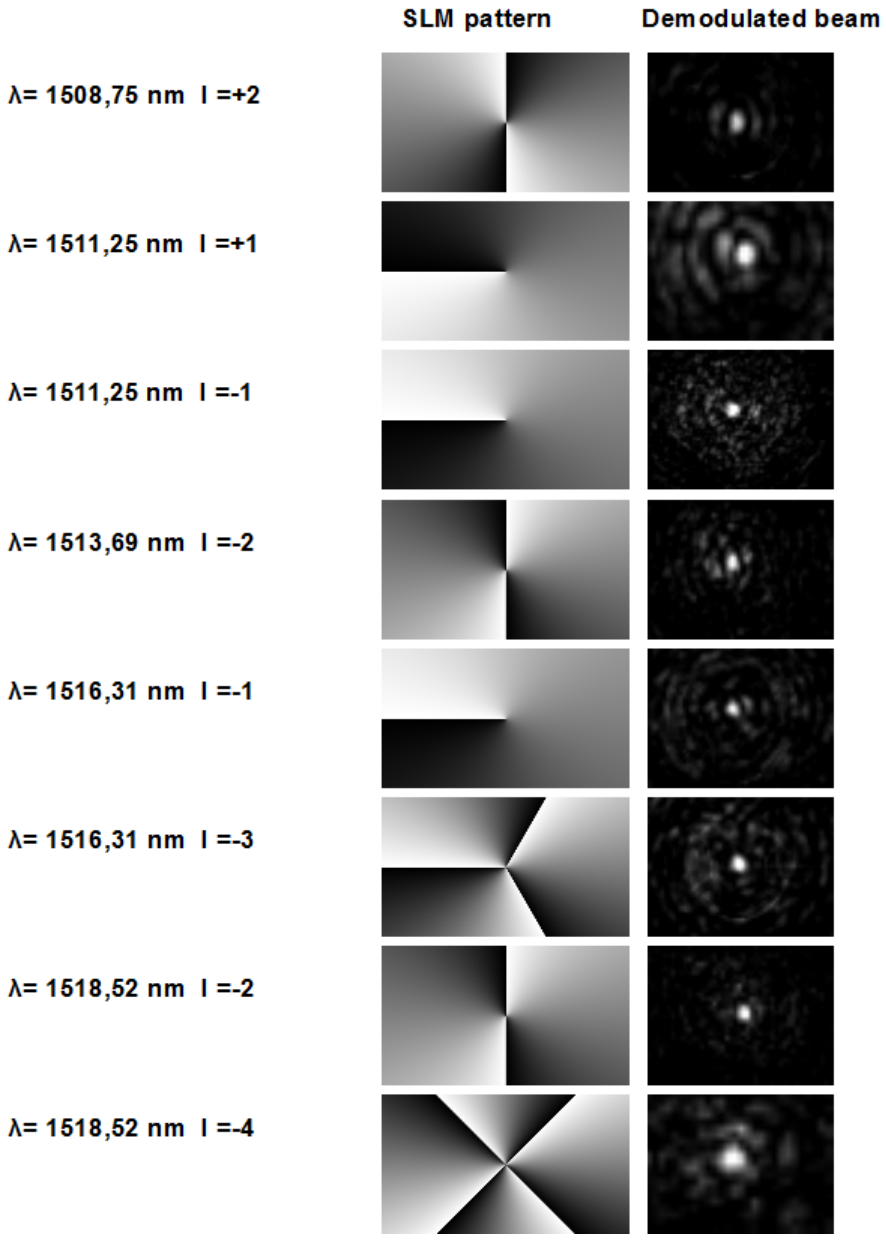

Figure 6.29: Intensity distribution of the demodulated beams for different wavelengths and OAM orders (right) and phase patterns used in SLM (left).

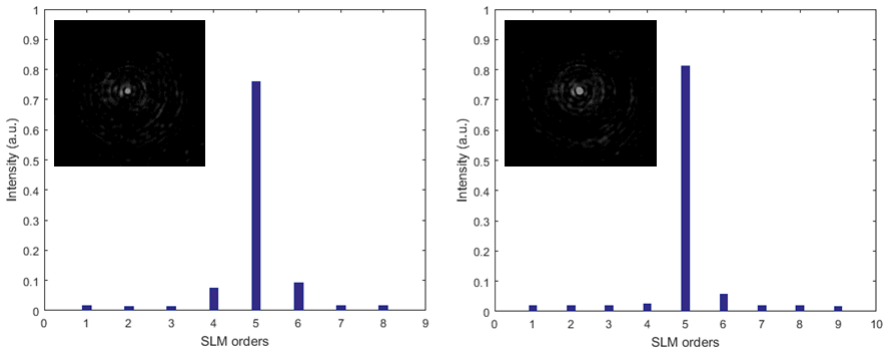

Figure 6.30: Modal purity of a OAM beam, at $\lambda = 1520,81\ nm$, emitted by two distinct waveguides of the OAM emitter. The principal OAM order is $l = -5$.

axis of the OAM beams would give rise to evident asymmetries in the recorded images. Nevertheless, the obtained pattern do not show any evidences of such imperfections; these results prove that the proposed layouts allows to efficiently mix beams with different OAM orders without significant impairments on the symmetry of the emitted radiation with regard to the single emission case. Further analyses, employing experimental setup with longer distances between the emitter and the recording instruments, are necessary but these results suggest that the devices represent a possible solution for Mode-Division-Multiplexing schemes employing OAM-carrying beams.

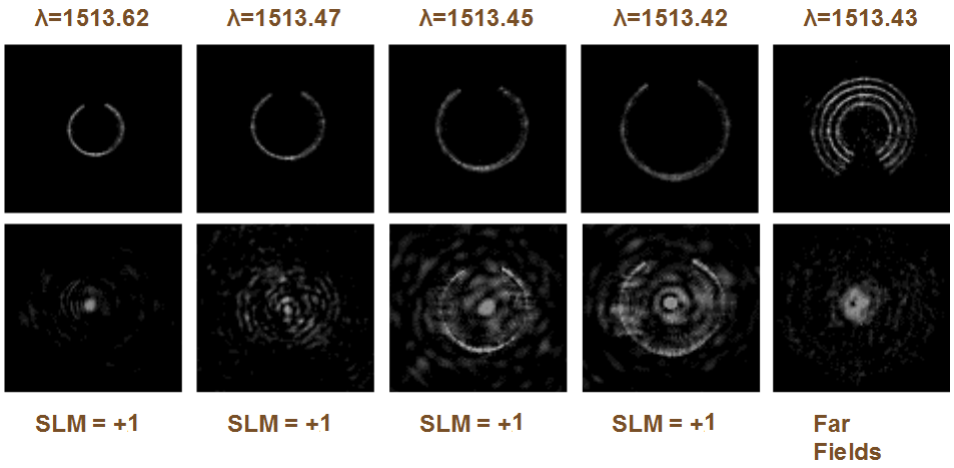

Figure 6.31: Near field intensity profiles (up) and relative demodulated patterns (down) of the beams radiated by a Omega-shaped emitter with four waveguides separately excited (a,b,c,d). In the last column near field intensity distribution and far field intensity distribution of the beam radiated with the four waveguides excited.

Conclusions

This Thesis dissertation has been focused on the analysis of the physical properties of strained silicon structures, and in particular of the structural, mechanical and electromagnetic properties of the photonic devices based on strained silicon technology. Strained silicon has been recently shown to induce nonlinear effects, (not observed in pure silicon due to its crystal symmetry properties) which can be fruitfully exploited for the realization of novel optical functionalities. The aim is to study the effects induced by lattice deformations, which are generated through the deposition of high intrinsic stress films, in the structures under analysis and the impact on the optical properties of such semiconductor devices to obtain a deeper understanding of the physical principles underlying the insurgence of nonlinear effects in deformed silicon structures and to investigate their dependency on the experimental technological nanofabrication parameters. In order to accomplish this task, we carried out a set of simulative and experimental studies on strained silicon structures and SOI devices that allowed us to estimate, through the employment of the developed FEM-based simulative model, the lattice deformations induced on micrometric and nanometric stilicon rib structures by the deposition of a silicon nitride layer and to measure the strain field distribution through the employment of the Convergent Beam Electron Diffraction (CBED) technique. We have also assessed the effectiveness of lattice deformation, observed in the analyzed photonic devices, in altering the optical properties of strained SOI waveguides through the employment of a multhyphysical simulative model and of experimental techniques for the measurements of the performance of the manufactured SOI devices. We manufactured the silicon structures and SOI devices that we have used for the the experimental measurements employing the novel Space Pattering Method manufacturing technique that allowed us to realize nanometric features starting from conventional photolithography and we carried out experimental analysis on the quality of the processes that provided useful information on the possible use of this nanofabrication technique for the manufacturing of strained silicon photonic devices.

An overview of the proposed silicon photonic devices employing the strained silicon technology was provided in Chapter 1 focusing on the advantages that could stem from their use in interconnects and switching fabrics of IT-infrastructures in terms of bandwidth, power consumption and wiring density. In particular, we described the effects that are commonly exploited in silicon based optical

devices to achieve modulation functionalities, i.e thermo-optic and free carrier dispersion effect, and highlighted the limits of performance of these devices concerning the tunability range, the induced loss and power consumption. Then we described the strained silicon photonic devices that have been proposed for the realization of optical functionalities exploiting nonlinear effects, such as Pockels effect and Second Harmonic Generation, induced by lattice deformation showing the potential of strained silicon photonics technology.

In Chapter 2 we provided the theoretical framework for the analysis of structural and optical properties of strained SiPh devices. In particular, I introduced the mathematical equations that describe mechanical and electromagnetic problems and the implementation of this theoretical model in the FEM-based simulative tools that we have developed for the analysis of the lattice deformation and their effects on the optical properties of the manufactured devices. Then we described the sources of loss suffered by radiation traveling in SOI waveguides for straight and bent rib and ridge structures highlighting the influence of geometrical imperfections, stemming from nonidalities in the manufacturing processes, on the performance of the devices and provided state-of-the-art values of optical losses that have been used as reference to assess the quality of the manufacturing processes employed for the realization of SOI waveguide.

Strained silicon rib structures and devices have been successfully manufactured starting from Si and SOI wafer through the employment of the Spacer Pattering Method (SPM) technique, discussed in Chapter 3, and an experimental analysis based on electron microscopy techniques has been carried on the micro- and nano-fabricated devices. The results, reported in Chapter 3, proved the reliability and accuracy of the CMOS processes employed and in particular of the SPM nanofabtication technique. The SPM, that had never been employed for the realization of photonic devices, allowed to successfully define nanometric structures and gaps starting from conventional photolitography obtaining the expected dimensions. In particular, the layout contained ribs and ridges with(450×220) nm geometry separated by gaps with minimal dimension of 200 nm. The etching processes have not been impaired by the closeness of the other structure and the delicate gap definition has been accomplished correctly also for coupling ribs sections. The LPCVD Si_3N_4 layer was conformally deposited on the structures and, despite the high intrinsic stress that produced significant strain values in the devices, it has not induced crack or delaminations in the ridge or in the structures. These results confirm the employability of these technological processes and techniques for the manufacturing of photonic devices.

A simulative and experimental analysis of the lattice deformation of the manufactured devices as well as of the optical properties of the nanofabricated strained SOI devices has been carried out and its results are reported in Chapters 4 and 5. In particular the distributions of strain tensor components ε_{xx}, ε_{xz} and ε_{zz} across the silicon rib structures have been estimated through the employment of a finite element method (FEM) based simulative model. The simulative estimations, reported in Chapter 4, that have been obtained assuming the geometries observed on the manufactured structures, show strain values

of the order of the millistrain for all the considered components, with maximum values obtained at theSi/Si_3N_4 interface, for both micrometric and nanometric ridges. In particular, maximum values of 2.2 $m\varepsilon$ for ε_{xx}, -2.3 $m\varepsilon$ for ε_{zz} and ± 1.8 $m\varepsilon$ have been obtained in the micrometric structures. Instead, For the nanometric case, we attained maximum strain values of 2.8 $m\varepsilon$ for ε_{xx}, -3.1 $m\varepsilon$ for ε_{zz} and ± 3.5 $m\varepsilon$ for ε_{xz}. Both ε_{xx} and ε_{zz} show a symmetric behavior with respect to the rib vertical axis, while an anti-symmetric one is found for ε_{xz}, as expected from theory. Around the rib center, the amplitude of ε_{xx} and ε_{zz} components is found to be still significant for the nanometric structures differently from the micrometric case while the ε_{xz} component approaches to negligible values for both the structures. These results confirm the possibility to attain significant values for all the strain tensor components analyzed in photonic structures through the deposition of a high intrinsic stress silicon nitride layer.

A comparative analysis between the strain values estimated through the FEM based simulative model and those obtained through the Convergent Beam Electron Diffraction (CBED) technique, has been carried out obtaining a good agreement between the expected and the experimental values. The measured strain components behaviors of the manufactured structures, reported in Chapter 5 follow the theoretical expectations confirming, in particular, a symmetric behavior for ε_{xx} and ε_{zz}, and an anti-symmetric behavior for ε_{xz}. Furthermore, the estimated values of ε_{xx} and ε_{xz} show a quantitative agreement with those measured through the CBED technique. For vertical deformation, i.e. for the case of ε_{zz}component, the amount of strain is underestimated by simulative predictions for both the micrometric and nanometric structures. This discrepancy can be linked to the reduction of sample thickness down to 200 nm required for the TEM analysis. This procedure makes the sample subject to deformation assessment and phenomena of strain relaxation that the simulative model, assuming a bulk condition for the sample, does not take into consideration. These results show that the developed simulative model and CBED strain measurement technique represent reliable and accurate tools for the analysis of structural properties of strained silicon structures and that can be employed in the design of photonic structures exploiting strained silicon technology.

The optical properties of single and coupling strained SOI waveguides have been evaluated through a multiphysical simulative model and the results are reported in Chapter 5. A good modal confinement and values of birefringence of $1.3{\cdot}10^{-2}$ have been obtained together with a variation of $5{\cdot}10^{-3}$ and $9{\cdot}10^{-3}$ for the effective refractive index and effective group index, respectively, with regard to the stress-free case when a 350 nm Si_3N_4 thick layer is deposited. Note that the attained values of the analyzed electromagnetic properties are of the same order of magnitude of those possessed by lithium niobate commonly employed in modulating devices; this paves the way for an effective use of strained silicon technology. The presence of the high intrinsic film is therefore expected to affect significantly the optical properties of the silicon nanowire, in particular inducing a significant optical anisotropy and enabling the presence of second order nonlinear effects without deteriorating the guiding properties of the SOI

waveguides.

The propagation losses of the manufactured strained SOI waveguides have been evaluated through the experimental Fabry-Perot (FP) resonance technique, discussed in Chapter 5. Propagation losses of $(5.8 \pm 0.8)\ dB/cm$ for the range $1545 - 1547\ nm$ and $(8.8 \pm 0.8)\ dB/cm$ for the range $1555 - 1557\ nm$ have been obtained. Despite the FP technique can overestimate the loss coefficients, (since it assumes perfect waveguide facets while the reflectivity is usually lower than the ideal Si/air interface), the obtained values are of the same order of magnitude of those reported in literature for the state-of-the art waveguides fabricated with the 193 nm optical lithography or electron beam lithography. These results confirm, therefore, the quality of the manufacturing processes employed and in particular the reliability of the SMP technique for the realization of low loss SOI waveguide-based devices.

In addition to the described research activity, we carried out an experimental study on the electromagnetic properties of novel integrated emitters of optical beams carrying a well-defined orbital angular momentum (OAM) order. These devices are based on silicon photonics technology and represent an innovative type of structures that has gained growing interest due to its potential use as multiplexer in free-air optical communication. We carried out this research activity during an internship as visiting postgraduate researcher at the Electronics and Nanoscale Engineering Division of the School of engineering of the University of Glasgow. The outcomes of this activity, reported in Chapter 6, provided important information for the understanding of the optical properties of the OAM carrying radiated beams and the impact of the experimental technology nanafabrication parameters on performance of the devices, in particular on the phase distribution and OAM purity of the emitted beams. Furthermore this analysis allowed to explore the potential use of SiPh OAM emitters in telecom and datacom applications as well as to estimate the advantages, in terms of crosstalk and switching speed, brought by the replacement of the actually employed bulk OAM emitters with the proposed devices. The results show that radiation efficiency values of 27% can be obtained for ring-shaped emitters and that the adjustment of geometrical parameters could bring to a significant enhancement of the emitted power. We showed that omega-shaped emitters can efficiently accomplish multiplexing operations in OAM-based free-space communication showing high values of OAM purity in the emitted beams; in particular side mode suppression ratio (SMSR) values around 10 dB have been obtained for 4-OAM orders multiplexing schemes for all the geometries that have been considered. In view of these results, we believe that SiPh integrated OAM emitters can be fruitfully employed in multiplexing techniques for free-space and fiber-optic communications and that the replacement of bulk OAM emitters with the proposed devices could bring to significant advantages.

In conclusion, the outcomes of the simulative and experimental analysis reported in this Thesis dissertation provided important information on the material properties of strained silicon structures as well as on experimental and simulative tools that could be employed to implement this technology in SiPh devices and provide accurate and reliable analysis on strained silicon structures.

In particular, the results show that the deposition of a high intrinsic stress silicon nitride film on silicon structures is exerting a strong straining effect that, in accordance with the multiphysical analysis, induces significant nonlinear effects in silicon devices for datacom and telecom applications. At the same time, we assessed the quality and reliability of the Spacer Patterning Technique method employed for the manufacturing of strained silicon photonic devices: due to its low-cost and high yield processing the SPM represents a promising alternative to actually employed technology and can provide benefices to the development of SiPh, and in particular to the strained SiPh. Within this work we also proved the accuracy of the developed FEM-based models and of the CBED experimental technique for the estimation and measurements of lattice deformation in silicon photonic structures and the strain-induced optical properties, showing that these two techniques can be effectively employed for the analysis of photonics devices based on strained silicon technology. Finally, we believe that the SPM nanofabrication technique can be fruitfully employed for the manufacturing of strained silicon devices and that the developed FEM-based simulative models together with the CBED strain measurement technique represent accurate and reliable tools for the analysis of strained SiPh devices. The results of the simulative and experimental analysis that we have reported in this Thesis, in particular the significant values of birefringence as well as the low propagation losses of strained SOI devices that we have obtained, show that strained silicon technology can be fruitfully employed as a technological platform for the manufacturing of novel and high-performance optoelectronic silicon photonic devices.

Bibliography

[1] Benner, Alan F., et al. "Exploitation of optical interconnects in future server architectures." IBM Journal of Research and Development 49.4.5 (2005): 755-775.

[2] Sakr, Sherif, et al. "A survey of large scale data management approaches in cloud environments." IEEE Communications Surveys & Tutorials 13.3 (2011): 311-336.

[3] Feng, Wu-chun, and Kirk Cameron. "The green500 list: Encouraging sustainable supercomputing." Computer 40.12 (2007): 50-55.

[4] http://www.thefoa.org/tech/ref/appln/datacenters.html

[5] Gripp, Jürgen, et al. "Optical switch fabrics for ultra-high-capacity IP routers." Journal of Lightwave Technology 21.11 (2003): 2839.

[6] Poon, Andrew W., et al. "Cascaded microresonator-based matrix switch for silicon on-chip optical interconnection." Proc. IEEE 97.7 (2009): 1216-1238.

[7] Feng, Shaoqi, et al. "Silicon photonics: from a microresonator perspective." Laser & photonics reviews 6.2 (2012): 145-177.

[8] Haurylau, Mikhail, et al. "On-chip optical interconnect roadmap: challenges and critical directions." IEEE Journal of Selected Topics in Quantum Electronics 12.6 (2006): 1699.

[9] http://www.networkworld.com/article/2164240/lan-wan/cisco-funded-startup-unveils-breakthrough-router--targets-sdns.html

[10] http://www.intel.it/content/www/it/it/architecture-and-technology/silicon-photonics/silicon-photonics-overview.html

[11] Bianco, Andrea, et al. "Optical interconnection networks based on microring resonators." Journal of Optical Communications and Networking 4.7 (2012): 546-556.

[12] Pintus, P., Ming-Chun Tien, and John E. Bowers. "Design of magneto-optical ring isolator on SOI based on the finite-element method." IEEE Photonics Technology Letters 23.22 (2011): 1670-1672.

[13] Li, Chao, Linjie Zhou, and Andrew W. Poon. "Silicon microring carrier-injection-based modulators/switches with tunable extinction ratios and OR-logic switching by using waveguide cross-coupling." Optics express 15.8 (2007): 5069-5076.

[14] Ding, Jianfeng, et al. "Ultra-low-power carrier-depletion Mach-Zehnder silicon optical modulator." Optics express 20.7 (2012): 7081-7087.

[15] Xiao, Xi, et al. "High-speed, low-loss silicon Mach–Zehnder modulators with doping optimization." Optics express 21.4 (2013): 4116-4125.

[16] Vlasov, Yurii A. "Silicon CMOS-integrated nano-photonics for computer and data communications beyond 100G." IEEE Communications Magazine 50.2 (2012): s67-s72.

[17] Dong, Po, et al. "Wavelength-tunable silicon microring modulator." Optics express 18.11 (2010): 10941-10946.

[18] Xu, Qianfan, et al. "12.5 Gbit/s carrier-injection-based silicon micro-ring silicon modulators." Optics express 15.2 (2007): 430-436.

[19] Reed, Graham T., et al. "Silicon optical modulators." Nature photonics 4.8 (2010): 518-526.

[20] Marsh, John. "Electro-absorption modulator with broad optical bandwidth." U.S. Patent Application No. 10/507,670.

[21] Izutsu, Masayuki. "LITHIUM NIOBATE MODULATOR." Encyclopedic Handbook of Integrated Optics (2005): 122.

[22] Cocorullo, G., and I. Rendina. "Thermo-optical modulatin at 1.5 μm in silicon etalon." Electronics Letters 28.1 (1992): 83-85.

[23] Cocorullo, G., F. G. Della Corte, and I. Rendina. "Temperature dependence of the thermo-optic coefficient in crystalline silicon between room temperature and 550 K at the wavelength of 1523 nm." Applied physics letters 74.22 (1999): 3338-3340.

[24] Pavesi, Lorenzo, and Gérard Guillot. "Optical interconnects." Springer series in optical sciences 119 (2006).

[25] Atabaki, A. H., et al. "Optimization of metallic microheaters for high-speed reconfigurable silicon photonics." Optics express 18.17 (2010): 18312-18323.

[26] Soref, R., et al. "Electrooptical effects in silicon." IEEE journal of quantum electronics 23.1 (1987): 123-129.

[27] Reed, Graham T. Silicon Photonics: the state of the art. John Wiley & Sons, 2008.

[28] Pavesi, Lorenzo, and David J. Lockwood. Silicon photonics. Vol. 1. Springer Science & Business Media, 2004.

[29] Xu, D-X., et al. "Eliminating the birefringence in silicon-on-insulator ridge waveguides by use of cladding stress." Optics letters 29.20 (2004): 2384-2386.

[30] Jacobsen, Rune S., et al. "Strained silicon as a new electro-optic material." Nature 441.7090 (2006): 199-202.

[31] Cazzanelli, M., et al. "Second-harmonic generation in silicon waveguides strained by silicon nitride." Nature materials 11.2 (2012): 148-154.

[32] Chmielak, Bartos, et al. "Pockels effect based fully integrated, strained silicon electro-optic modulator." Optics express 19.18 (2011): 17212-17219.

[33] Chmielak, Bartos, et al. "Investigation of local strain distribution and linear electro-optic effect in strained silicon waveguides." Optics express 21.21 (2013): 25324-25332.

[34] Lenahan, P. M., D. T. Krick, and J. Kanicki. "The nature of the dominant deep trap in amorphous silicon nitride films: Evidence for a negative correlation energy." Applied Surface Science 39.1-4 (1989): 392-405.

[35] Weber, K. J., and H. Jin. "Improved silicon surface passivation achieved by negatively charged silicon nitride films." Applied Physics Letters 94.6 (2009): 063509.

[36] Sharma, Rajat, et al. "Characterizing the effects of free carriers in fully etched, dielectric-clad silicon waveguides." Applied Physics Letters 106.24 (2015): 241104.

[37] Azadeh, S. Sharif, et al. "On the measurement of the Pockels effect in strained silicon." Optics letters 40.8 (2015): 1877-1880.

[38] Landau, Lev D., and E. M. Lifshitz. "Theory of Elasticity, vol. 7." Course of Theoretical Physics 3 (1986): 109.

[39] Grundmann, Marius. The Physics of Semiconductors: An Introduction Including Nanophysics and Applications. Springer, 2016.

[40] Belen'kiĭ, G. L., E. Yu Salaev, and R. A. Suleĭmanov. "Deformation effects in layer crystals." Soviet Physics Uspekhi 31.5 (1988): 434.

[41] Hopcroft, Matthew A., William D. Nix, and Thomas W. Kenny. "What is the Young's Modulus of Silicon?." Journal of microelectromechanical systems 19.2 (2010): 229-238.

[42] Riley, Frank L. "Silicon nitride and related materials." Journal of the American Ceramic Society 83.2 (2000): 245-265.

[43] Kazinczi, Robert, Jeff R. Mollinger, and Andre Bossche. "Reliability of silicon nitride as structural material in MEMS." Symposium on Micromachining and Microfabrication. International Society for Optics and Photonics, 1999.

[44] Irene, E. A. "Residual stress in silicon nitride films." Journal of Electronic Materials 5.3 (1976): 287-298.

[45] Temple-Boyer, P., et al. "Residual stress in low pressure chemical vapor deposition SiNx films deposited from silane and ammonia." Journal of Vacuum Science & Technology A 16.4 (1998): 2003-2007.

[46] Olson, James M. "Analysis of LPCVD process conditions for the deposition of low stress silicon nitride. Part I: preliminary LPCVD experiments." Materials Science in Semiconductor Processing 5.1 (2002): 51-60.

[47] Vanzetti, L., et al. "Correlation between silicon-nitride film stress and composition: XPS and SIMS analyses." Surface and interface analysis 38.4 (2006): 723-726.

[48] Claassen, W. A. P., et al. "On the relation between deposition conditions and (mechanical) stress in plasma silicon nitride layers." Thin Solid Films 129.3-4 (1985): 239-247.

[49] Morin, Pierre, et al. "A comparison of the mechanical stability of silicon nitride films deposited with various techniques." Applied surface science 260 (2012): 69-72.

[50] Sze, Simon Min. Semiconductor devices: physics and technology. John Wiley & Sons, 2008.

[51] Saleh, Bahaa EA, Malvin Carl Teich, and Bahaa E. Saleh. Fundamentals of photonics. Vol. 22. New York: Wiley, 1991.

[52] Giacovazzo, Carmelo. Fundamentals of crystallography. Vol. 7. Oxford University Press, USA, 2002.

[53] Boyd, Robert W. Nonlinear optics. Academic press, 2003.

[54] Winnie, N. Ye, et al. "Birefringence control using stress engineering in silicon-on-insulator (SOI) waveguides." Journal of lightwave technology 23.3 (2005): 1308.

[55] Lifante, Ginés. Integrated photonics: fundamentals. John Wiley & Sons, 2003.

[56] Agrawal, Govind P. "Fiber-Optic Communication Systems."

[57] Marcuse, Dietrich. Theory of dielectric optical waveguides. Elsevier, 2013.

[58] Powell, Olly. "Single-mode condition for silicon rib waveguides." Journal of Lightwave Technology 20.10 (2002): 1851.

[59] Pavesi, Lorenzo, and David J. Lockwood. Silicon photonics. Vol. 1. Springer Science & Business Media, 2004.

[60] Selvaraja, Shankar Kumar. Wafer-scale fabrication technology for silicon photonic integrated circuits. Diss. PhD thesis, Ghent University, 2011.

[61] Tien, P. K. "Light waves in thin films and integrated optics." Applied Optics 10.11 (1971): 2395-2413.

[62] Vlasov, Yurii, and Sharee McNab. "Losses in single-mode silicon-on-insulator strip waveguides and bends." Optics express 12.8 (2004): 1622-1631.

[63] Hiremath, Kirankumar Rajshekhar. Coupled mode theory based modeling and analysis of circular optical microresonators. Kirankumar R. Hiremath, 2005.

[64] Senior, John M., and M. Yousif Jamro. Optical fiber communications: principles and practice. Pearson Education, 2009.

[65] Quarteroni, Alfio, and Alberto Valli. Numerical approximation of partial differential equations. Vol. 23. Springer Science & Business Media, 2008.

[66] https://www.comsol.com/multiphysics/finite-element-method

[67] Drever, R. W. P., et al. "Laser phase and frequency stabilization using an optical resonator." Applied Physics B 31.2 (1983): 97-105.

[68] Bortnik, Bartosz, et al. "Electrooptic polymer ring resonator modulation up to 165 GHz." IEEE Journal of Selected Topics in Quantum Electronics 13.1 (2007): 104-110.

[69] Yariv, A. "Universal relations for coupling of optical power between microresonators and dielectric waveguides." Electronics Letters 36.4 (2000): 321-322.

[70] Bogaerts, Wim, et al. "Silicon microring resonators." Laser & Photonics Reviews 6.1 (2012): 47-73.

[71] Han, Xiuyou, et al. "Quasi-single-sideband radio over fiber transmission with a polymer-based waveguide microring resonator." Optical Engineering 50.12 (2011): 124601-124601.

[72] Carroll, John E., James Whiteaway, and Dick Plumb. Distributed feedback semiconductor lasers. Vol. 10. IET, 1998.

[73] Wolf, Stanley. "Silicon processing for the VLSI era." LATTICE. 1995.

[74] Karen A. Reinhardt and Richard F. Reidy;"Handbook of Cleaning in Semiconductor Manufacturing: Fundamental and Applications", ISBN: 9780470625958

[75] Hwang, Joowon, et al. "A middle-1X nm NAND flash memory cell (M1X-NAND) with highly manufacturable integration technologies." Electron Devices Meeting (IEDM), 2011 IEEE International. IEEE, 2011.

[76] Matteo Ferri, Fulvio Mancarella, Alberto Roncaglia, James Ransley, Jize Yan, Ashwin Seshia, "Fabrication of DETF sensors in SOI technology with submicron air gaps using a maskless line narrowing technique", IEEE SENSORS 2008

[77] Gnan, M., et al. "Fabrication of low-loss photonic wires in silicon-on-insulator using hydrogen silsesquioxane electron-beam resist." Electronics Letters 44.2 (2008): 115-116.

[78] Kittel, Charles. Introduction to solid state. John Wiley & Sons, 1966.

[79] Tanaka, Michiyoshi, and Kenji Tsuda. "Convergent-beam electron diffraction." Journal of electron microscopy 60.suppl 1 (2011): S245-S267.

[80] Williams, David B., and C. Barry Carter. "The transmission electron microscope." Transmission electron microscopy. Springer Us, 1996. 3-17.

[81] Armigliato, A., et al. "Analysis of localised strains in crystals by convergent beam electron diffraction." High-Pressure Crystallography. Springer Netherlands, 2004. 277-294.

[82] Mayer, Joachim, et al. "TEM sample preparation and FIB-induced damage." Mrs Bulletin 32.05 (2007): 400-407.

[83] Oatley, C. W., W. C. Nixon, and R. F. W. Pease. "Scanning electron microscopy." Advances in Electronics and Electron Physics 21 (1966): 181-247.

[84] Joel,"Invitation to the SEM World: For People who are Using the SEM for the First Time"

[85] Reed, Graham T., and Andrew P. Knights. "Silicon photonics: an introduction." John Wiley & Sons, 2004.

[86] Andriolli, Nicola, et al. "Challenges and progress toward a silicon-based multi-microring optical network-on-chip." Networks and Communications (EuCNC), 2014 European Conference on. IEEE, 2014.

[87] Marini, D., et al. "Lattice deformations in strained-silicon rib structures for photonic devices." Photonics Technologies, 2014 Fotonica AEIT Italian Conference on. IEEE, 2014.

[88] Marini, D., et al. "Study of induced strain in silicon rib structures." Group IV Photonics (GFP), 2014 IEEE 11th International Conference on. IEEE, 2014.

[89] R. Balboni, et al. "Strain determination by CBED in Si-rib structures for photonic devices", 18th International Microscopy Congress, Prague, Czech Republic, Sep 2014, P. MS-8-P-2815.

[90] Montanari, G. B., et al. "Induced strain in silicon waveguides and couplers." SPIE OPTO. International Society for Optics and Photonics, 2015.

[91] Marini, D., et al. "Study of birefringence and strain distribution in silicon waveguides and coupling structures." Fotonica AEIT Italian Conference on Photonics Technologies, 2015. IET, 2015.

[92] D. Marini, et al. "Strain assessment in strained-silicon photonic structures", European Optical Society Topical Meeting on Optical Microsystems, Sep 2015, paper OμS 15-07.

[93] Allen, Leslie, Stephen M. Barnett, and Miles J. Padgett. Optical angular momentum. CRC Press, 2003.

[94] Maxwell, James Clerk. A treatise on electricity and magnetism. Vol. 1. Clarendon press, 1881.

[95] Poynting, John Henry. "On the transfer of energy in the electromagnetic field." Philosophical Transactions of the Royal Society of London 175 (1884): 343-361.

[96] Jackson, John David. Classical electrodynamics. Wiley, 1999.

[97] Poynting, J. H. "The wave motion of a revolving shaft, and a suggestion as to the angular momentum in a beam of circularly polarised light." Proceedings of the Royal Society of London. Series A, Containing Papers of a Mathematical and Physical Character 82.557 (1909): 560-567.

[98] Beth, Richard A. "Mechanical detection and measurement of the angular momentum of light." Physical Review 50.2 (1936): 115.

[99] Allen, Les, et al. "Orbital angular momentum of light and the transformation of Laguerre-Gaussian laser modes." Physical Review A 45.11 (1992): 8185.

[100] Verma, Manish, et al. "separation of spin and orbital angular momentum states from cylindrical vector beams." Optik-International Journal for Light and Electron Optics (2016).

[101] Volke-Sepulveda, K., et al. "Orbital angular momentum of a high-order Bessel light beam." Journal of Optics B: Quantum and Semiclassical Optics 4.2 (2002): S82.

[102] Gibson, Graham, et al. "Free-space information transfer using light beams carrying orbital angular momentum." Optics Express 12.22 (2004): 5448-5456.

[103] Djordjevic, Ivan B., and Murat Arabaci. "LDPC-coded orbital angular momentum (OAM) modulation for free-space optical communication." Optics express 18.24 (2010): 24722-24728.

[104] Djordjevic, Ivan B. "Deep-space and near-Earth optical communications by coded orbital angular momentum (OAM) modulation." Optics express 19.15 (2011): 14277-14289.

[105] Willner, Alan E., Jian Wang, and Hao Huang. "A different angle on light communications." Science 337.6095 (2012): 655-656.

[106] Malik, Mehul, et al. "Influence of atmospheric turbulence on optical communications using orbital angular momentum for encoding." Optics Express 20.12 (2012): 13195-13200.

[107] Awaji, Yoshinari, Naoya Wada, and Yasunori Toda. "Demonstration of spatial mode division multiplexing using Laguerre-Gaussian mode beam in telecom-wavelength." 2010 IEEE Photonic Society's 23rd Annual Meeting. 2010.

[108] Wang, Jian, et al. "Terabit free-space data transmission employing orbital angular momentum multiplexing." Nature Photonics 6.7 (2012): 488-496.

[109] Huang, Hao, et al. "100 Tbit/s free-space data link using orbital angular momentum mode division multiplexing combined with wavelength division multiplexing." Optical Fiber Communication Conference. Optical Society of America, 2013.

[110] Marrucci, Lorenzo, C. Manzo, and D. Paparo. "Pancharatnam-Berry phase optical elements for wave front shaping in the visible domain: Switchable helical mode generation." Applied Physics Letters 88.22 (2006): 221102

[111] Mirhosseini, Mohammad, et al. "Rapid generation of light beams carrying orbital angular momentum." Optics express 21.25 (2013): 30196-30203.

[112] Sorel, Marc, et al. "Photonic integrated devices for exploiting the orbital angular momentum (OAM) of light in optical communications." Optical Communication (ECOC), 2015 European Conference on. IEEE, 2015.

[113] Doerr, Christopher R., and Lawrence L. Buhl. "Circular grating coupler for creating focused azimuthally and radially polarized beams." Optics letters 36.7 (2011): 1209-1211.

[114] Su, Tiehui, et al. "Demonstration of free space coherent optical communication using integrated silicon photonic orbital angular momentum devices." Optics express 20.9 (2012): 9396-9402.

[115] Cai, Xinlun, et al. "Integrated compact optical vortex beam emitters." Science 338.6105 (2012): 363-366.

[116] Beijersbergen, M. W., et al. "Helical-wavefront laser beams produced with a spiral phaseplate." Optics Communications 112.5 (1994): 321-327.

[117] Zhu, Jiangbo, et al. "Theoretical model for angular grating-based integrated optical vortex beam emitters." Optics letters 38.8 (2013): 1343-1345.

[118] Hardy, A. M. O. S., David F. Welch, and William Streifer. "Analysis of second-order gratings." IEEE Journal of Quantum Electronics 25.10 (1989): 2096-2105.

[119] Streifer, William, D. Scifres, and Robert Burnham. "Coupled wave analysis of DFB and DBR lasers." IEEE Journal of Quantum Electronics 13.4 (1977): 134-141.